

The coherence collapse regime of high-coherence
Si/III-V lasers and the use of swept frequency
semiconductor lasers for full field 3D imaging

Thesis by
Mark Harfouche

In Partial Fulfillment of the Requirements for the
degree of
Doctor of Philosophy

The logo for the California Institute of Technology (Caltech), featuring the word "Caltech" in a bold, orange, sans-serif font.

CALIFORNIA INSTITUTE OF TECHNOLOGY
Pasadena, California

2018
Defended October 5, 2017

© 2018

Mark Harfouche

ORCID: 0000-0002-4657-4603

All rights reserved except where otherwise noted

ACKNOWLEDGEMENTS

First and foremost, I would like to thank my parents for the opportunity they have given me to grow up and study in North America. I do not ignore that their personal sacrifice has allowed me to invest nearly three decades of my life in pursuit of scientific knowledge. My brothers, Pierre and Henry, have also continuously supported me during my studies at Caltech.

My time as one of Prof. Amnon Yariv's students has truly been remarkable. He has fostered an atmosphere that encourages learning and finding one's passion. By bringing together motivated students and researchers from around the world, he created a group where ideas can be shared and explored to their fullest extent. Much of the work presented here is built on the foundations laid down by previous students and collaborators and would have been impossible without their expertise.

I would also like to thank my committee, Prof. Oskar Painter, Prof. Azita Emami, Prof. Andrei Faraon and Prof. Axel Scherer for their time, guidance, and expertise throughout my graduate studies.

None of the work presented in my thesis would have been possible without the generous support of various government funding agencies. The US Army Research Office (ARO), Defense Advanced Research Projects Agency (DARPA), and the Natural Sciences and Engineering Research Council of Canada (NSERC) have all funded me at various stages during my time as a graduate student.

I was lucky enough to have met five key individuals that have defined my experience at Caltech. First and foremost, I would like to thank Dr. Dongwan Kim with whom I have spent countless hours in and outside the lab, often when I didn't deserve it. Dr. Roarke Horstmeyer shared with me his love for mathematics and optics and made California a welcoming state. Dr. Manan Arya always made home a welcoming place and shared his passion for space and art with me. Dr. Christos Santis taught me everything I know about semiconductor lasers and joined me on many adventures around Pasadena and Toronto. Finally, Naresh Satyan taught me about the rigors of the lab and not to ignore the natural beauty of California.

Graduate school would not have been the same without many other mentors, collaborators, and friends: Dr. Scott Steger, Dr. Yasha Vilenchik, Dr. Huolei Wang, Dr. Arseny Vasilyev, Dr. Jacob Sendowski, Dr. George Rakuljic, Dr. Jeff White, Dr. Paula Popescu, Marilena Dimotsantou, Dr. Sinan Zhao, Hetuo Chen, Zhewei

Zhang, Prof. Bruno Crosignani, Alireza Ghaffari, Dr. Reginald Lee, Connie Rodriguez, and Christy Jenstad. Their welcoming attitude and insight made the Yariv group a great place to spend my last 6 years. A special thanks to Prof. Joyce Poon who guided me as an undergraduate student at the University of Toronto in my early years in optics.

Many other friends shaped California into a great place to call home: SJ, KF, ES, BH, JB, EV, EM, FS, MJ, KT, MA, LK, DY. Finally I would like to thank Janaki Sheth for her unyielding support over the last two years.

ABSTRACT

The semiconductor laser is the linchpin of optical communication and is now also penetrating a wide spectrum of new applications such as biomedical sensing, coherent communication, metrology, and time keeping. These require a higher degree of temporal coherence than is available from the present generation. Recently, it has been proposed and shown that heterogeneously integrated lasers on silicon and InGaAsP can be used to design high coherence single mode lasers with a much narrower linewidth than their all InGaAsP counterparts. Unfortunately, these lasers suffer from large thermal impedances and their optical feedback characteristics have not yet been explored. In the first part of this thesis, we will explore how flip chip bonding can help decrease the thermal impedance of these lasers to improve their overall performance and show that these lasers can provide up to 20 dB of optical isolation compared to their all III-V counterparts.

In the second part of this thesis, we will report on the use of commercially available semiconductor lasers, in conjunction with an optical modulator to obtain high-resolution tomographic images in one shot without any moving parts. The electronic control over the imaged depth of this novel tomographic imaging camera enables it to monitor arbitrary depth slices in rapid succession over a depth range limited only by the coherence length of the laser. Not only does this imaging modality acquire the transverse image intensity (x, y) distribution of the light reflected from a particular depth, but also the phase of the reflected light enabling imaging beyond the conventional depth of field of the lens. This has important implications in applications requiring high lateral resolution images where the shallow depth of field would often require mechanical scanning of the lens elements to change the imaged depth.

PUBLISHED CONTENT AND CONTRIBUTIONS

- [1] M. Harfouche, N. Satyan, A. Vasilyev, and A. Yariv, “Compressive sensing optical coherence tomography using randomly accessible lasers,” vol. 9109, 2014, pp. 91090L–8. doi: 10.1117/12.2048754. [Online]. Available: <http://dx.doi.org/10.1117/12.2048754>,
M.H. participated in the conception of the project, realizing the experimental setup, analysing the data, and writing the manuscript.
- [2] M. Harfouche, N. Satyan, G. Rakuljic, and A. Yariv, “A full-field tomographic imaging camera based on a linearly swept frequency dfb at 1064 nm,” in *CLEO: 2015*, Optical Society of America, 2015, AM2J.1. doi: 10.1364/CLEO_AT.2015.AM2J.1. [Online]. Available: http://www.osapublishing.org/abstract.cfm?URI=CLEO_AT-2015-AM2J.1,
M.H. participated in the conception of the project, realizing the experimental setup, analysing the data, and writing the manuscript.
- [3] D. Kim, P. Popescu, M. Harfouche, J. Sendowski, M.-E. Dimotsantou, R. Flagan, and A. Yariv, “On-chip integrated differential optical microring biosensing platform based on a dual laminar flow scheme,” in *CLEO: 2015*, Optical Society of America, 2015, STu4K.7. doi: 10.1364/CLEO_SI.2015.STu4K.7. [Online]. Available: http://www.osapublishing.org/abstract.cfm?URI=CLEO_SI-2015-STu4K.7,
M.H. aided in the data analysis, troubleshooting the experimental setup, linearizing the laser and writing the manuscript.
- [4] D. Kim, P. Popescu, M. Harfouche, J. Sendowski, M.-E. Dimotsantou, R. C. Flagan, and A. Yariv, “On-chip integrated differential optical microring refractive index sensing platform based on a laminar flow scheme,” *Opt. Lett.*, vol. 40, no. 17, pp. 4106–4109, Sep. 2015. doi: 10.1364/OL.40.004106. [Online]. Available: <http://ol.osa.org/abstract.cfm?URI=ol-40-17-4106>,
M.H. aided in the data analysis, troubleshooting the experimental setup, linearizing the laser and writing the manuscript.
- [5] J. O. White, M. Harfouche, J. Edgecumbe, N. Satyan, G. Rakuljic, V. Jayaraman, C. Burgner, and A. Yariv, “1.6 kW Yb fiber amplifier using chirped seed amplification for stimulated Brillouin scattering suppression,” *Appl. Opt.*, vol. 56, no. 3, B116–B122, Jan. 2017. doi: 10.1364/AO.56.00B116. [Online]. Available: <http://ao.osa.org/abstract.cfm?URI=ao-56-3-B116>,
M.H. participated in realizing the experimental setup, analysing the data, and writing the manuscript.
- [6] M. Harfouche, D. Kim, H. Wang, N. Satyan, G. Rakuljic, and A. Yariv, “Optical feedback sensitivity of heterogeneously integrated silicon/iii-v lasers,”

in *Conference on Lasers and Electro-Optics*, Optical Society of America, 2017, SW4C.7. DOI: 10.1364/CLEO_SI.2017.SW4C.7. [Online]. Available: http://www.osapublishing.org/abstract.cfm?URI=CLEO_SI-2017-SW4C.7,

M.H. aided in conducting the experiments, the data analysis, and writing the manuscript.

- [7] D. Kim, M. Harfouche, H. Wang, N. Satyan, G. Rakuljic, and A. Yariv, “Suppression of linewidth enhancement factor in high-coherence heterogeneously integrated silicon/iii-v lasers,” in *Conference on Lasers and Electro-Optics*, Optical Society of America, 2017, SW4C.8. DOI: 10.1364/CLEO_SI.2017.SW4C.8. [Online]. Available: http://www.osapublishing.org/abstract.cfm?URI=CLEO_SI-2017-SW4C.8,

M.H. aided in conducting the experiments, the data analysis, and writing the manuscript.

- [8] W. Huolei, D. Kim, M. Harfouche, N. Satyan, G. Rakuljic, and A. Yariv, “Narrow-linewidth oxide-confined heterogeneously integrated si/iii-v semiconductor laser,” in *Conference on Lasers and Electro-Optics*, Optical Society of America, 2017, AM2B.2. DOI: 10.1364/CLEO_AT.2017.AM2B.2. [Online]. Available: http://www.osapublishing.org/abstract.cfm?URI=CLEO_AT-2017-AM2B.2,

M.H. aided in conducting the experiments, the data analysis, and writing the manuscript.

TABLE OF CONTENTS

Acknowledgements	iii
Abstract	v
Published Content and Contributions	vi
Table of Contents	viii
Chapter I: Thesis overview	1
1.1 Introduction	1
1.2 Applications of semiconductor lasers	2
1.3 Semiconductor laser structures	4
I Quantum noise controlled Si/III-V lasers	8
Chapter II: The quantum noise controlled semiconductor laser	9
2.1 Platform parameters	9
2.2 Quantum noise control review	12
2.3 Output power optimization of quantum noise controlled lasers	16
2.4 Final platform design parameters	19
2.5 Conclusions	21
Chapter III: Thermal properties of high-Q silicon/III-V lasers	22
3.1 Thermal characteristic of semiconductor lasers	22
3.2 Thermal challenges for heterogeneously integrated lasers	23
3.3 Thermal impedance of high-coherence silicon III-V lasers	24
3.4 Flip-chip bonding for decreased thermal impedance	35
3.5 Flip-chip bonding results	39
3.6 Flip-chip bonding limitations	43
3.7 Conclusions	43
Chapter IV: Feedback sensitivity of high-coherence Si-III/V lasers	44
4.1 Optical feedback sensitivity review	44
4.2 Feedback sensitivity of high coherence Si/III-V lasers	49
4.3 Measurement of the feedback sensitivity of QNCL lasers	50
4.4 Conclusions	61
II 3D imaging with swept frequency semiconductor lasers	62
Chapter V: Swept source semiconductor lasers for 3D imaging	63
5.1 Swept frequency reflectometry	63
5.2 Optical sources for swept frequency reflectometry	68
5.3 Reference mirror location	70
5.4 The linearly swept frequency laser	70

5.5	Linearly swept frequency lasers at 850 nm and 1064 nm	71
5.6	Conclusions	73
Chapter VI: 3D imaging with the tomographic imaging camera		75
6.1	High resolution 3D imaging	75
6.2	TomlCam principle of operation	76
6.3	Comparison between different 3D imaging modalities	81
6.4	Imaging optics	82
6.5	Signal to noise ratio for shot noise limited measurements	84
6.6	Compatible modulation formats	85
6.7	Experimental results at 850 nm	88
6.8	Experimental results at 1064 nm	90
6.9	Conclusions	94
Chapter VII: Imaging beyond the depth of field		97
7.1	Depth of field of a $4f$ imaging system	97
7.2	Computationally refocusing images acquired with TomlCam	101
7.3	Experimental results with a resolution target	102
7.4	Experimental results for retro-reflective polystyrene beads	104
7.5	3D imaging in bulk dielectric volumes	105
7.6	Conclusions	109
Bibliography		110
Appendix A: Silicon and III-V wafers		124

Chapter 1

THESIS OVERVIEW

1.1 Introduction

Since its inception in 1975 [1], the distributed feedback laser (DFB laser) has become instrumental in nearly all applications requiring a precisely controlled light source. By combining recent advances in the understanding of periodic structures with advances in materials science, the DFB enabled the precise control of the lasing wavelength in a monolithic semiconductor laser. This drastically reduced the power and size requirements for a spectrally pure source at the time. Today, DFB lasers have found their way in diverse applications ranging from coherent communication systems to biomedical sensing, metrology, and time keeping.

More recently, a new type of semiconductor laser [2], based on a waveguide composed of both silicon and InGaAsP has emerged as the next contender for high-coherence lasers [3]. This novel structure uses modal engineering [4] to increase the coherence of semiconductor lasers by orders of magnitude.

This thesis is organized in two distinct sections. The first considers the design of high coherence semiconductor lasers on a heterogeneously integrated silicon-InGaAsP platform. There we consider the thermal properties of these lasers and how the design of the laser can be improved to mitigate the thermal effects. We also consider the feedback sensitivity of these high coherence laser to external optical reflections, showing experimental evidence that these lasers are much less sensitive to reflections in communication systems.

The second part describes the development of a novel 3D imaging technique that makes use of swept frequency semiconductor lasers and single optical modulator to obtain high resolution 3D imaging using a conventional CCD or CMOS camera. Like other techniques based on swept frequency lasers, the axial resolution of the images obtained is limited by the total change in frequency of the laser during the exposure known as the chirp bandwidth. Because the system makes use of a CCD camera to acquire the lateral information at a chosen depth in a few exposures, images much beyond the conventional depth of field can be obtained without sacrificing lateral resolution through computational refocusing.

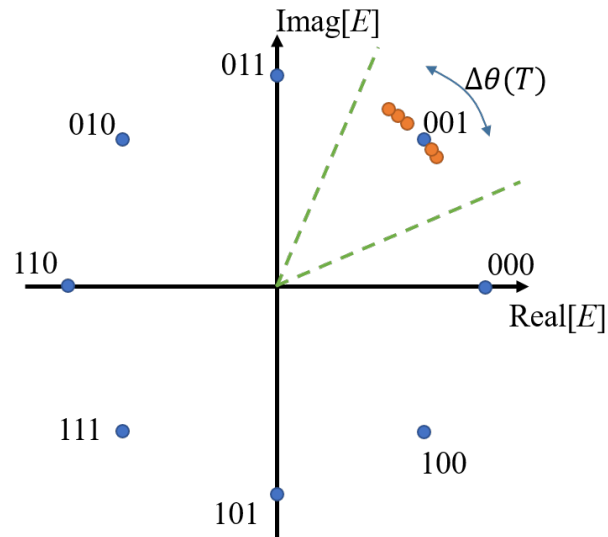


Figure 1.1: Constellation diagram of a phase shift keying modulation format sending three bits per symbol ($k = 3$). The blue dots indicate the ideal location of the symbol. The green dashed lines show the decision boundary of the detection system used to differentiate between the symbol for 001 and the adjacent symbols. The orange dots are visual representations of the measurement of a symbol when corrupted with phase noise.

1.2 Applications of semiconductor lasers

The semiconductor laser has become the linchpin of optical communication [5], [6]. It is now also penetrating a wide spectrum of new applications such as biomedical sensing [7], metrology [8], [9], time keeping [10], coherent communication [11], random number generation [12], and 3D imaging [13]. In this section, we will give a quick overview of how semiconductor lasers are used in coherence communication systems and in 3D imaging.

Digital communication

The most prolific deployment of semiconductor lasers is likely in the sector of digital communications. The low loss optical fiber ($\approx 0.25 \text{ dB km}^{-1}$ at 1550 nm [5]) has made it possible to create long reaching fiber optical networks. Today, the challenge for communication engineers has shifted from finding a low loss channel for communication to finding efficient modulation and detection formats that make the most of the existing fiber deployed around the globe. This has led to a shift toward coherent modulation formats that have a higher spectral efficiency (up to 6 bit/s/Hz using quadrature amplitude modulation [14]) than conventional on-off keying formats. These new modulation formats necessitate the ability to detect the

phase of light in addition to its intensity. This is typically done by beating the received signal with another laser at the receiver, known as the local oscillator (LO). For phase shift keying modulation formats, the probability of error for the detection of a symbol is determined by the variance of the measurement of the phase ($\Delta\theta^2$) and the separation between two symbols ($2\pi/2^k$), assuming k bits are sent per symbol, as illustrated in Figure 1.1 and given approximately by [15]:

$$P_e = \operatorname{erfc}\left(\frac{\pi}{2^k} \cdot \sqrt{\frac{1}{2\Delta\theta^2(T)}}\right), \quad (1.1)$$

where we the measurement time is T seconds, and erfc is the complimentary error function. The phase variance in a coherent detection system is given by

$$\Delta\theta^2(T) = \Delta\nu_{\text{ST}}T, \quad (1.2)$$

where $\Delta\nu_{\text{ST}}$ is the quantum limited linewidth (known as the Schawlow-Townes linewidth [16]) of the laser [17]. For a given bit error rate, narrow linewidth lasers enable sending an extra bit per symbol every time the variance phase noise is reduced by 3 dB enabling more information to be sent in the phase quadrature.

Transmission of information within a data center continues to play an important role in the design of communication networks the for a major portion of data center traffic [18]. While the length of fiber within a data centers is much smaller than the distance between cities, the length between computers in different racks can still reach 100's of meters [19] limiting the use of multi-mode fiber for high speed links. As such, it is predicted that in the coming years, there will be a larger move toward the deployment of single mode fiber for increased performance. Point to point links between the different computers are expected to enable a massive increase in the capacity of the communication links within data centers but require at least as many lasers as active links [20]. One ever-present challenge in these networks is the integration of an isolator. Optical isolation is necessary to keep the lasing frequency stable and the output of the laser stable [21]. Unfortunately, today's isolators are based on magnetic materials and are not amenable to the semiconductor methodology. Obviating the need for an isolator has the potential to massively reduce the cost of communication networks and improve the prospects of using CMOS electronic fabrication techniques for optical circuits.

High resolution 3D imaging

Another important application of semiconductor lasers is in the field of 3D imaging. Two important regimes have emerged: long range depth imaging, which goes

under the name of frequency modulated continuous wave LIDAR [22], and high-resolution 3D imaging, typically for biomedical applications taking the name of optical coherence tomography (OCT) [23]. Swept source ranging makes use of the large bandwidth available in the optical domain to measure the unambiguous depth of objects at high resolutions and in certain cases, can be shown to improve the signal to noise ratio compared to white light interferometry [24]. The basic principle of operation is illustrated in Figure 1.2. A typical system includes a swept-frequency laser, a reference mirror, beam forming elements, and a photodetector that measures the interference signal between the reference mirror and the imaged object. The lasing frequency of the laser can be changed in a continuous fashion either by changing the injection current [13], or by changing the length of the lasing cavity as is done in MEMS VCSELs [25]–[27]. In the case of a linear chirp, the optical path length between the sampled point object on the object and the reference mirror is directly proportional to the output photocurrent frequency at the photodetector. The details of this measurement will be described in detail Part II. 3D imaging continues to play an important role in many applications including high-accuracy optical profilometry [28], fingerprint detection [29], and many *in vivo* biomedical diagnostic applications [30]–[33]. As such, it is increasingly important to develop new 3D imaging modalities that are able to quickly acquire the desired information.

1.3 Semiconductor laser structures

We begin by describing key structures that are used in the design of semiconductor lasers. Figure 1.3 shows a schematic and cartoon for a Fabry-Perot (FP) cavity used in the most basic type of semiconductor laser. It contains three important sections:

1. The end mirrors: these mirror ensure that light recirculates within the cavity

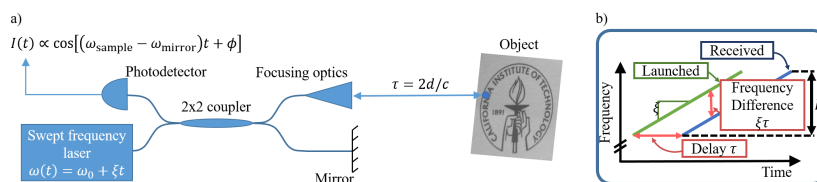


Figure 1.2: a) Depiction of a swept-source OCT/FMCW LIDAR system utilizing a linearized swept frequency laser. The frequency of the laser is swept linearly and the beat signal between a reference reflector and the collected light is recorded on a photodetector. b) The frequency of the beat signal is directly proportional to the time of flight difference between the mirror and imaged object.

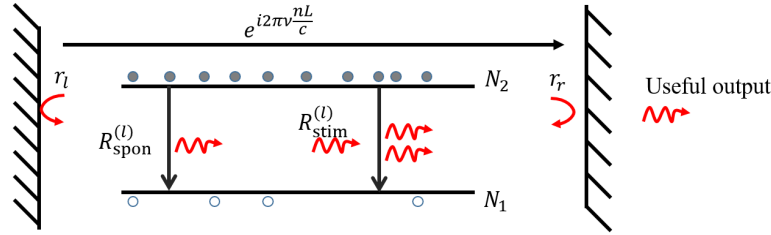


Figure 1.3: Cartoon of a typical Fabry-Perot semiconductor laser, illustrating the left and right mirrors, the phase section, as well as the gain medium. In the illustrated case, the gain medium is an excited 2 level system.

and control the output coupling of the cavity.

2. The phase section: in a Fabry-Perot laser, this corresponds to the entire length of the waveguide. Along with the phase of the reflection of the mirrors, it defines the phase matching condition.
3. A gain providing material: this material is usually distributed throughout the cavity, providing gain to the lasing mode (stimulated emission $W_{stim}^{(l)}$), as well as providing the seed and continuous source of noise, spontaneous emission ($W_{spon}^{(l)}$).

We assume a single oscillating transverse mode within the waveguide.

A resonator is qualified by two important numbers: the resonance frequency (ν in Hz) and the quality factor (Q). The resonance condition can be determined mathematically by considering the round trip phase accumulation in a cavity and ensure that the accumulated phase is an integer multiple of 2π . In the case of a FP cavity, this can be written as:

$$1 = e^{i\phi_l} e^{i2\pi\nu \frac{nL}{c}} e^{i\phi_r} e^{i2\pi\nu \frac{nL}{c}}, \quad (1.3)$$

where $\phi_{l,r}$ is the phase acquired upon reflection from the left and right facet respectively, L is the length of the waveguide, n is the effective index in the cavity, and c is the speed of light in vacuum. One shortfall of an FP laser is that for moderate length lasers, the cavity can contain a multitude of modes with similar quality factors which makes it challenging to control the exact lasing mode during fabrication.

DFB-like structures

Resonators can also be defined by creating “defects” in an otherwise uniform periodic grating within a waveguide, known as a distributed feedback grating (DFB), as shown

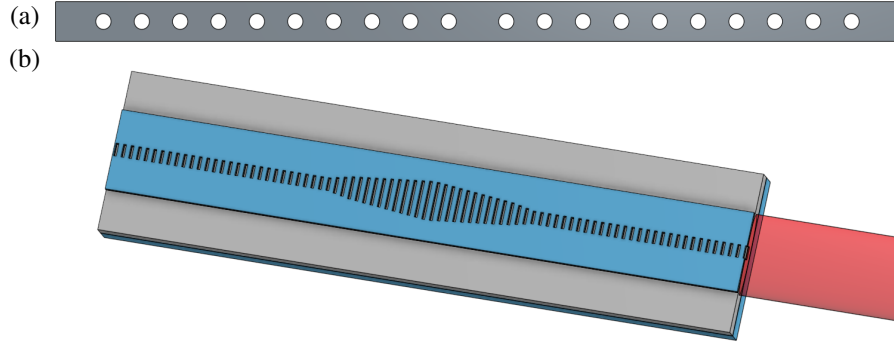


Figure 1.4: a) A cartoon of a quarter wave shift DFB resonator. The grating period is Λ and the small gap between the unit cells at the center of the grating is $\Lambda/4$. b) A cartoon (not to scale) of a mode gap resonator where the useful output of the laser is taken from the right side (shown in red). The defect in this case is a grating where one parameter, the grating strength in this case, is changed along the direction of propagation.

in Figure 1.4a [6]. A defect can be defined by varying a single parameter along the center of the grating enabling a mode to be localized within the stop band of the un-perturbed structure. By distributing the defect over a length of multiple microns, the optical mode is less localized and leading to decreased spacial hole burning [34], [35]. We call this laser a mode gap resonator, as shown in Figure 1.4b and discussed in more detail in Chapter 2.

Losses in semiconductor lasers

The quality factor (Q) is strongly related to the losses in the cavity through the following relation:

$$Q = 2\pi\nu \frac{\text{Energy stored}}{\text{Power lost}}. \quad (1.4)$$

It follows that

$$Q = 2\pi\nu\tau_p, \quad (1.5)$$

where τ_p is the experimental decay time constant for the modal energy often known as the photon cavity lifetime. We consider four main sources of loss in a resonator: absorption loss, scattering losses, radiation losses, and coupling losses. The photon cavity lifetime is given by the harmonic mean of the photon lifetimes obtained by considering the different sources of loss listed above:

$$\tau_p^{-1} = \tau_{\text{abs.}}^{-1} + \tau_{\text{scat.}}^{-1} + \tau_{\text{rad.}}^{-1} + \tau_{\text{ext.}}^{-1}. \quad (1.6)$$

Finite $\tau_{\text{abs.}}$ is due to the residual material absorption. Scattering losses, represented by $\tau_{\text{scat.}}^{-1}$, are typically present due to fabrication imperfections. This type of loss can be mitigated by decreasing the sidewall roughness of the waveguide by modifying the fabrication process [36]. Radiation losses, represented by $\tau_{\text{rad.}}^{-1}$, are present as a consequence of the design of the waveguide, cavity, and possibly the grating if one is present. Smooth transitions between waveguides of different shapes as well as k -space engineering [37] can help mitigate these losses.

We have demonstrated single mode resonators in silicon with quality factors of 1×10^6 operating near 1550 nm, indicating that the photon cavity lifetime in the laser mode due to material absorption and scattering is upwards of 0.8 ns [2] in our resonators. In InGaAsP, losses are typically dominated by free carriers absorption in the p and n doped claddings [38]. In Section 2.2 we will explore how modal engineering can be used to control the losses by changing the confinement factor in the low loss silicon and high loss InP to increase the effective photon cavity lifetime of the lasing mode without sacrificing the threshold current or output power of the laser.

Useful output coupling losses to external waveguides are necessary for the operation of a laser and define $\tau_{\text{ext.}}$. From the point of view of the optical cavity, the useful output is also considered a loss. As we will show in Section 2.3, this loss has to be designed to be the main source of loss in a laser to ensure high wall-plug efficiency.

Part I

Quantum noise controlled Si/III-V lasers

Chapter 2

THE QUANTUM NOISE CONTROLLED SEMICONDUCTOR LASER

In this chapter, we describe the general structure and design of the quantum noise controlled lasers on the heterogeneously integrated silicon-InGaAsP platform. We note that the details of this platform are discussed in [4], [39], [40] and published in [2], [41], [42]. We will therefore restrict the discussion to the salient features of the platform and justify the choice of parameters for the lasers that will be analyzed in the remainder of this thesis. The lasers are built on a heterogeneously integrated silicon-InGaAsP platform similar to those used in [43], [44]. The integration of silicon and III-V semiconductors on the same platform is attractive since it enables the generation of light at 1550 nm and 1310 nm [45], [46] as well as the fabrication of complex photonic circuits [47], [48] in the high index silicon that can be used to transmit information. We will begin by describing the general platform, highlighting how quantum noise control is achieved, and finish with a summary of the laser parameters for the measured lasers.

2.1 Platform parameters

The quantum noise controlled lasers are designed as a single waveguide where the light is primarily guided in a silicon core. The final structure contains a InGaAsP epitaxially grown stack that is directly bonded to a thin layer of SiO₂ over the length of the entire grating without the use of any transition regions. A cross-section of the final structure is shown in Figure 2.1.

Prior to bonding the InGaAsP epi layer, a ridge silicon waveguide is defined on a 500 nm thick silicon layer by etching a rib approximately 60 nm deep and 2.5 μm wide. In the same fabrication step, a grating is etched in the center of the waveguide to define the optical cavity by etching holes 60 nm wide in the direction of propagation, and of varying width, between 200 and 500 nm in the x direction. A scanning electron microscope image of the waveguide and grating prior to bonding are shown in Figure 2.2. The final waveguide supports two TE-like polarized modes, shown in Figure 2.3. Since the second mode does not overlap significantly with the grating (etched in the center of the waveguide), only the fundamental transverse mode possesses a high quality factor (Q) mode. The silicon is patterned using the

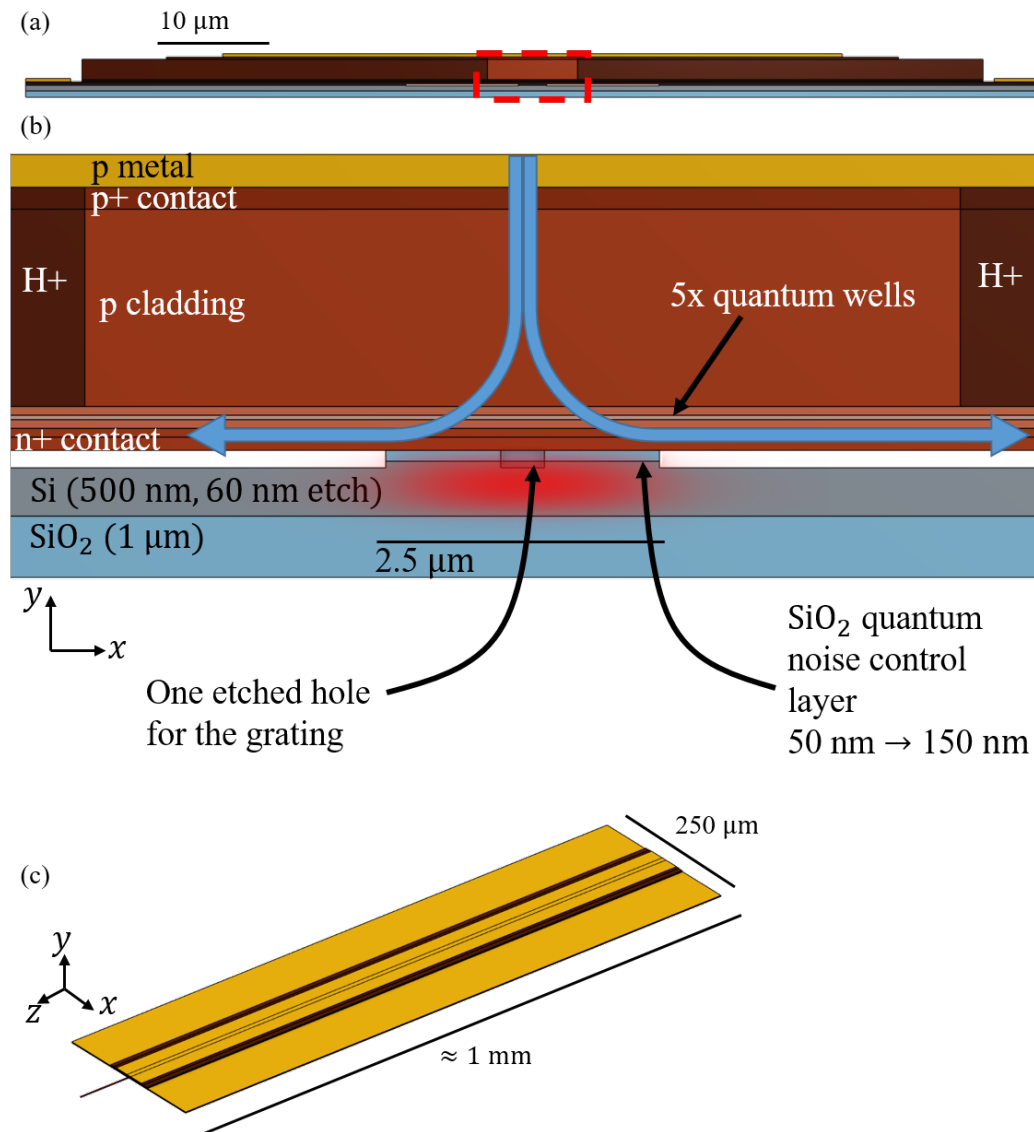


Figure 2.1: (a) The cross section of the laser showing the silicon core, InGaAsP mesa structure, and buried oxide layer. The silicon handle below the SiO₂ (150 μm thick after thinning) is omitted. (b) View of the dashed region of the laser structure. The epitaxially grown InGaAsP mesa structure, directly bonded to the silicon, is detailed in [4]. The electrical current path is defined through ion implantation and is shown in blue. Current flows from the top p-contact to the two n-contacts on either side of the laser. The optical mode is shown in red. (c) Isometric view of the top of a typical laser (1 mm long in this case). The output is depicted as a small beam on the bottom left side. Since the laser cavity is symmetric, light also exists from the back side.

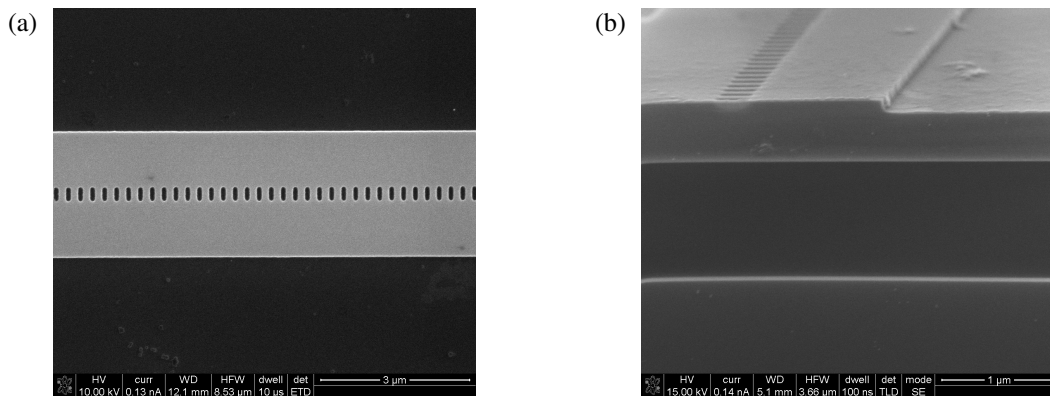


Figure 2.2: a) Top view of a short portion of the silicon grating defining the resonator, approximately 10 μm of the 1 mm resonator. b) Side view of a different resonator showing the cross-section of the waveguide.

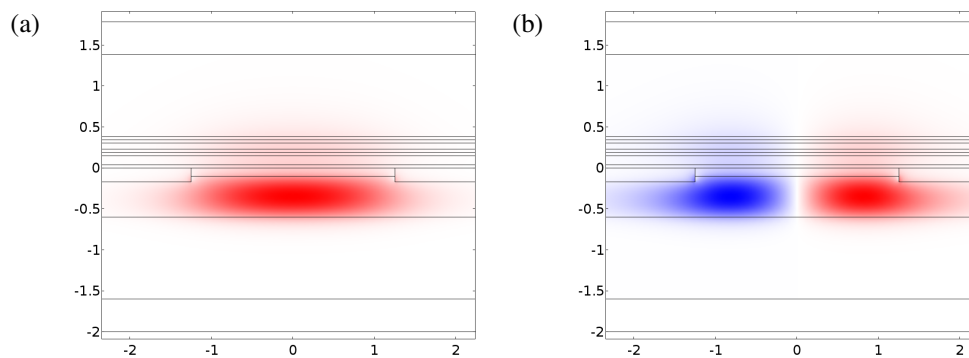


Figure 2.3: Color legend: red denotes a positive electric field while blue denote a negative electric field. The wire-frame outlines the geometry of the waveguide with the core being made of the silicon, bottom cladding SiO_2 and the upper cladding being the InGaAsP epitaxially grown structure. The thin layer between the silicon core and the InGaAsP is the quantum noise control layer, whose thickness here is 100 nm. a) Electric field distribution of the TE0-like mode. b) Electric field distribution of the TE1-like mode. Note that the TE1 mode has a null in the center of the waveguide, making it not interact with the grating.

Leica Microsystems EBPG-5000+ electron beam writer at the Kavli Nanoscience Institute at Caltech while the InGaAsP is patterned using standard contact optical lithography. The thickness of the SiO_2 layer between the silicon core and the InGaAsP controls the fraction of light that is confined in the low loss silicon core and in the lossy but light generating InGaAsP active layer. Figure 2.5 shows the E_x field along the center of the waveguide as the thickness of the “quantum noise control layer” is varied. In Section 2.2, we will show how changing the thickness of this layer decreases the intrinsic losses in the resonator and suppresses spontaneous emission in the resonator, giving the low noise characteristics of the lasers.

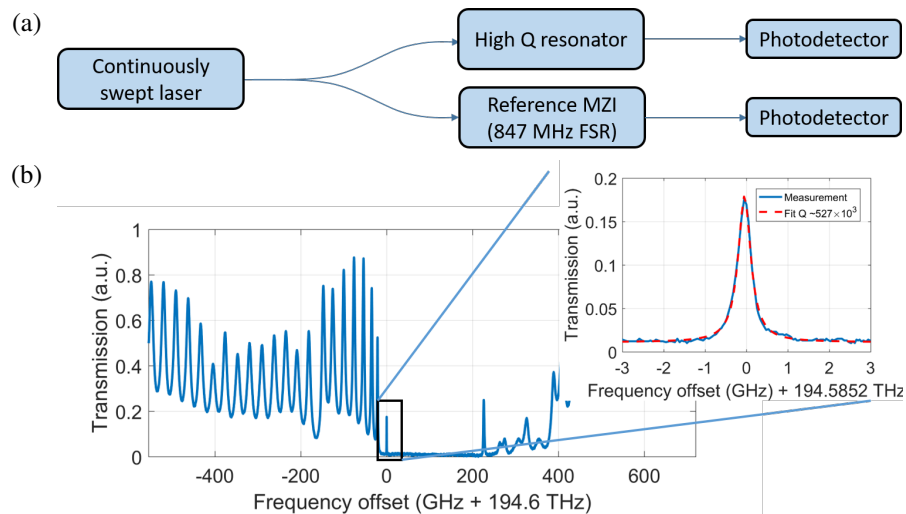


Figure 2.4: a) Cartoon of the transmission measurement setup. A reference Mach-Zehnder interferometer is used to characterize the linearity of the sweep to ensure an accurate estimate of the quality factor. b) Representative measurement of the transmission spectrum of a high-Q modegap resonator. The loaded quality factor of this particular resonator was determined to be just above 500×10^3 . Loaded quality factors of under coupled resonators have been measured as high as 1.2×10^6 .

The mode gap resonator is designed by “engineering” the band edges of the grating as described in [39]. The design of the resonator ensures that the mode envelope in the direction of propagation is a Gaussian, minimizing spatial hole burning and radiation loss [37]. The measured transmission spectra of a sample high-Q modegap resonator is shown in Figure 2.4. This measurement is taken using a tunable laser and a Mach-Zehnder interferometer (MZI) as a frequency reference to accurately characterize the sweep of the laser in the vicinity of the resonance. For our most under coupled resonators, a quality factor of 1.2×10^6 was measured, indicating that the maximum photon cavity lifetime in the resonator due to sidewall scattering and absorption is approximately 1 ns.

2.2 Quantum noise control review

The presence of the QNCL, the SiO_2 layer between the III-V and the Si, affords us a degree of control over the basic properties of the semiconductor laser to a degree not previously possible in the conventional all III-V lasers. In the case of the lasers studied in this part of thesis, a single transverse mode is used to guide light throughout the entire laser as opposed to using transition regions to shuffle the mode between the silicon layer and the InGaAsP layer [49], [50]. The key advantage of this strategy is the ability to engineer a compact single mode high-

quality factor resonator without worrying about step discontinuities through the cavity or coupling to external resonators. Furthermore, as shown in [3], [4], the thin SiO_2 layer introduced between the silicon and the InGaAsP can control by orders of magnitude the confinement factor of the mode in the low loss silicon and the lossy InGaAsP. This allows the design to take advantage of the two orders of magnitude difference between the losses in the III-V and the silicon to engineer the optimal cavity. Since the confinement factor in the quantum wells is proportional to the confinement factor in the InGaAsP, decreasing the confinement in the InGaAsP has the added effect of decreasing the spontaneous emission of the excited electrons hole pairs in the quantum wells into the lasing mode. Hereafter, we will refer to this SiO_2 layer, which plays a key role in the laser design, as the quantum noise control layer (QNCL). Figure 2.5 shows the E_x field for the optical mode at the center of the waveguide changes with the increased thickness of the quantum noise control layer and Figure 2.6 shows the energy density of the mode along the center for the same thicknesses of the quantum noise control layer. The confinement factors (Γ) in the different sections of the waveguide, defined as the fraction of total optical energy in the respective layers, are summarized in Figure 2.5b obtained using finite element simulations to compute the 2D modal profile in the silicon/III-V waveguide with COMSOL 5.1.

The thickness of the quantum noise control layer (t_{QNCL}) is used to change the confinement factor between in different materials. As indicated by the simulations above, larger values of QNCL thicknesses increase the confinement factor in the silicon, and decrease the interaction between the mode and the gain (and noise) providing quantum wells. The quality factor of the silicon/III-V waveguide can be estimated by considering the intrinsic quality factor of each material in isolation (Q_{Si} and Q_{InGaAsP} respectively) and their respective confinement factors (Γ) through:

$$\frac{1}{Q_{\text{tot}}} = \frac{\Gamma_{\text{Si}}}{Q_{\text{Si}}} + \frac{\Gamma_{\text{InGaAsP}}}{Q_{\text{InGaAsP}}}, \quad (2.1)$$

where Γ_{Si} and Γ_{InGaAsP} are the confinement factors of the optical mode in the low-loss portion of the resonator (Silicon, air, and silicon dioxide) and is InGaAsP epi-structure, respectively. Because InGaAsP is orders of magnitude lossier than our high-Q silicon resonator, the total quality factor is well approximated by

$$Q_{\text{tot}} = \frac{Q_{\text{InGaAsP}}}{\Gamma_{\text{InGaAsP}}(t_{\text{QNCL}})}, \quad (2.2)$$

until the resonator Q becomes limited by the losses in the silicon waveguide. This in our case is approximately valid for $t_{\text{QNCL}} < 150$ nm for a silicon resonator with

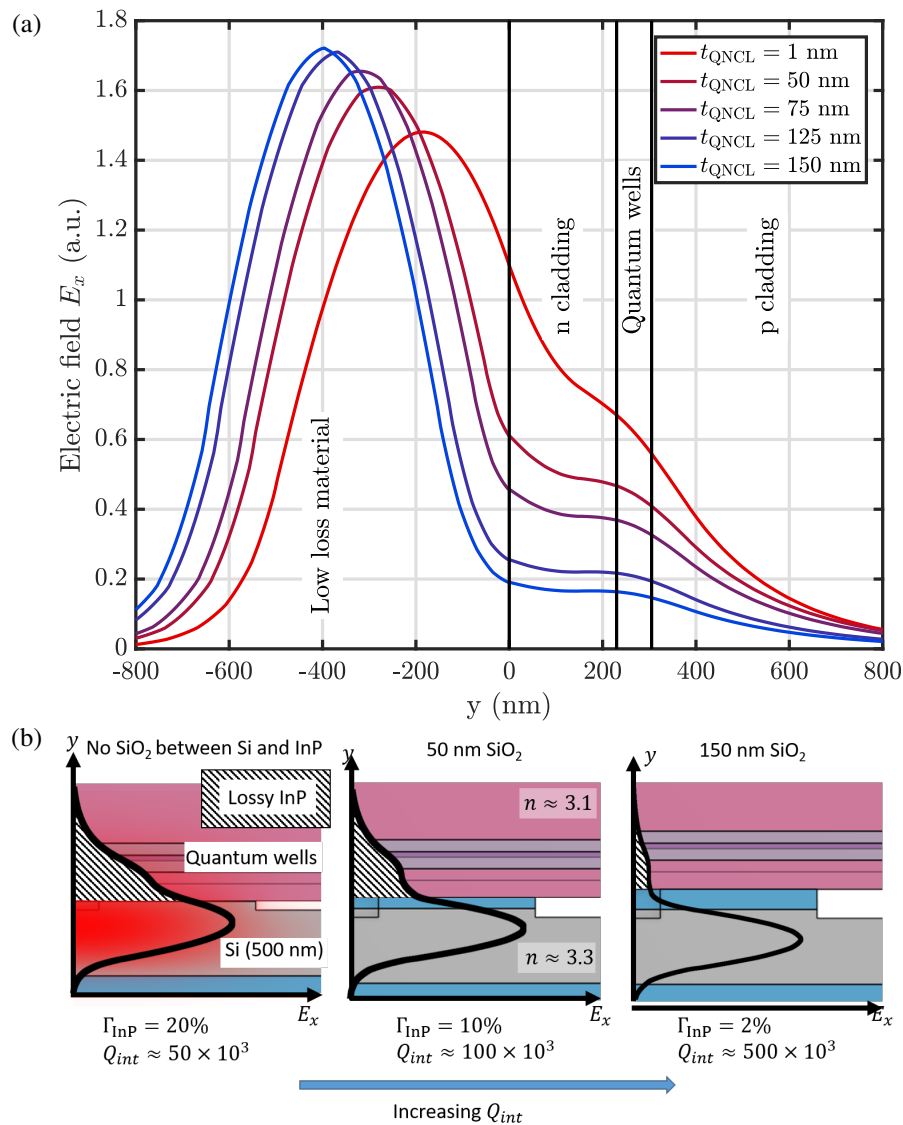


Figure 2.5: a) Electrical field profile at the center of the waveguide for different thicknesses of quantum noise control layers (QNCL). The low-loss (silicon, and silicon dioxide) as well as the pertinent sections of the InGaAsP epi-structure are labeled. b) Cartoon of how the optical mode changes when the SiO_2 layer is added. The intrinsic quality factor of the different different QNCL structures is indicated below each structure, assuming that the intrinsic quality factor of the III-V is 1×4 .

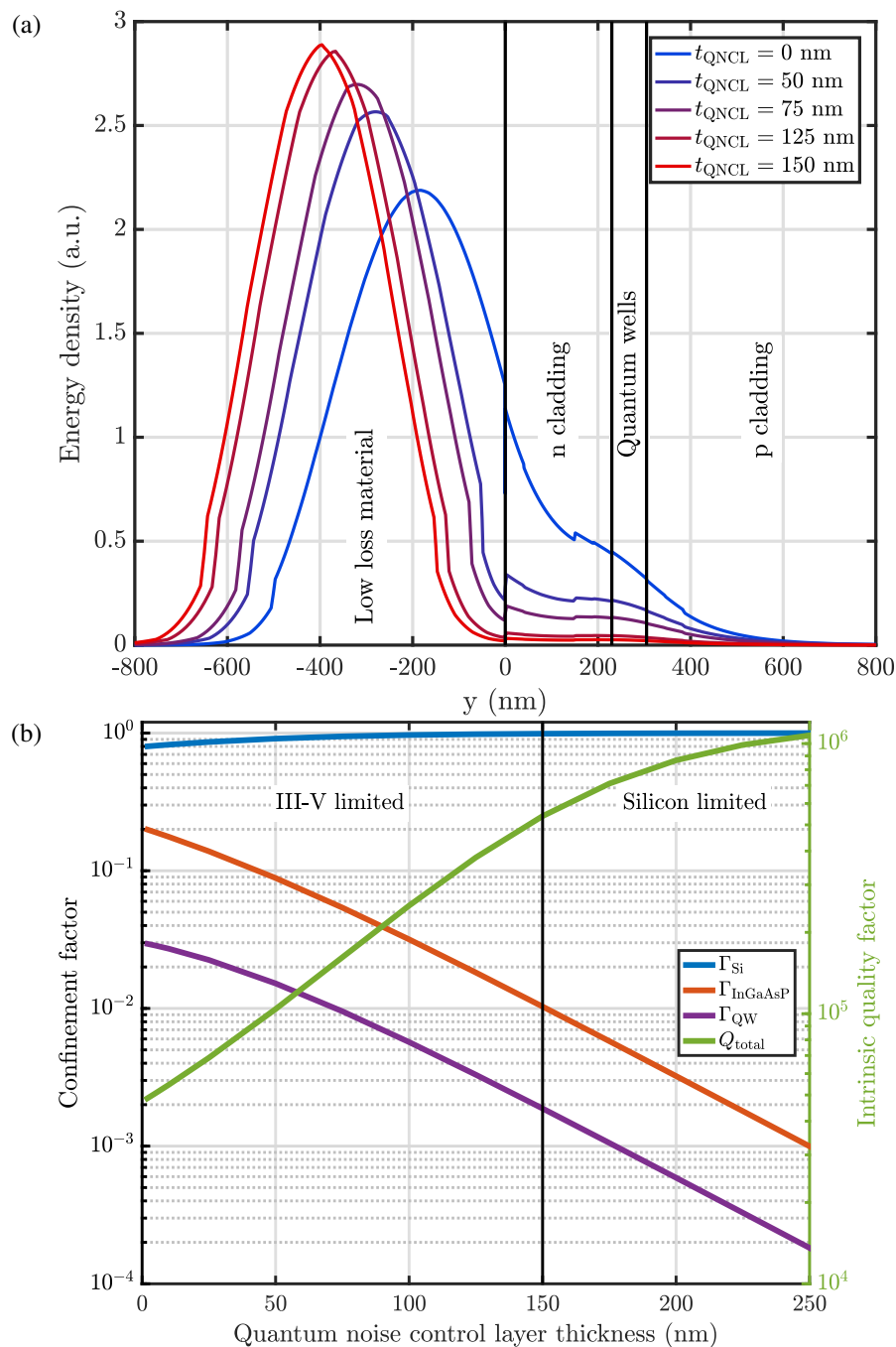


Figure 2.6: a) Optical energy density at the center of the waveguide for different thicknesses of quantum noise control layers (QNCL). The low-loss (silicon, and silicon dioxide) as well as the pertinent sections of the InGaAsP epi-structure are labeled. The discontinuity in the energy density profile is due to the varying refractive index in the structure. b) Summary of the confinement factor in the waveguide as the thickness of the quantum noise control layer is varied. Below a thickness of approximately 150 nm, the quality factor of the resonator increases in a manner inversely proportional to the confinement in the gain providing quantum wells.

a quality factor of 1.2×10^6 . Since $\Gamma_{\text{InGaAsP}}(t_{\text{QNCL}})$ can be made much smaller than 1, Equation 2.2 highlights the power of the quantum noise control layer to change the total quality factor of the resonator by orders of magnitude.

It has been shown in [2]–[4] that the location of the optical emitters, in our case the electron hole pairs within the quantum wells, has dramatic implications on the frequency noise power spectral density of the laser. The Schawlow-Townes linewidth is related to the spontaneous emission rate of a single pair into the lasing mode ($W_{\text{spont.}}^{(l)}$), the number of electron-hole pairs at threshold (N_{th}), the number of photons in the cavity (P), and the linewidth enhancement factor (α) by [51], [52]

$$\delta\nu_{\text{ST}} = \frac{N_{\text{th}} W_{\text{spont.}}^{(l)}}{2P}. \quad (2.3)$$

From the equation above, it can be seen that the spontaneous emission rate into the lasing mode, and the number of photons in the cavity have direct implications on the quantum limited linewidth of the laser. The quantum noise control layer introduced between the silicon and III-V changes both these parameters to ultimately increase the coherence of the silicon/III-V lasers. By decreasing the confinement factor of the optical mode in the quantum wells, the spontaneous emission into the lasing mode is decreased ($W_{\text{spont.}}^{(l)} \propto Q_{\text{tot}}^{-1}$). Similarly, by decreasing the confinement factor in the InGaAsP, the cold cavity (no gain) quality factor approaches that of the low loss silicon, increasing the photon storage ($P \propto Q_{\text{tot}}$) at a fixed output power. Combined, these two effects lead to a decrease in the quantum limited frequency noise by a factor of Q^{-2} .

The last few years have witnessed a strong and growing interest in using silicon-III/V lasers to leverage integration with silicon electronics to create integrated transceivers [53] for communication or sensor for various applications [54]. In the remainder of this thesis, we will explore how the use of the quantum noise control layer (QNCL) can yield lasers that are insensitive to optical feedback. In certain application, these lasers could operate without the use of costly magnetic based optical isolators. This is especially important in the case of integrated photonics and inexpensive communication links where each material is introduced at the cost of increased complexity fabrication.

2.3 Output power optimization of quantum noise controlled lasers

A natural question to ask is whether or not the introduction of the quantum noise control layer has a direct impact on the wall-plug efficiency of the laser. While the

linewidth and optical feedback sensitivity of the lasers can be decreased by increasing the quality factor of the laser, we will show that without careful consideration, this can come at the expense of output power for poorly designed lasers.

We begin by considering the case of a laser cavity interacting with a two level system. While this model is far from ideal, it models enough of the physics to understand how the thickness of the quantum noise control layer can affect the threshold and output power of the laser. The equations that describe the number of electron-hole pairs N , the number of photons in the cavity P , and output power P_{out} , can be written as:

$$\frac{dN}{dt} = \frac{I}{q} - \frac{(N - \bar{N})}{\tau_e} - gNP \quad (2.4)$$

$$\frac{dP}{dt} = -P \left(\frac{1}{\tau_{\text{ext}}} + \frac{1}{\tau_{\text{int}}} \right) + gNP \quad (2.5)$$

$$P_{\text{out}} = \frac{P}{\tau_{\text{ext}}} \cdot h\nu, \quad (2.6)$$

where g is the differential modal gain (from quantized field theory it can be shown to be equal to $W_{\text{spn.}}^{(l)}$), I is the injected current q is the charge of an electron, \bar{N} is the number of electron-hole pairs at transparency, τ_{int} is the total photon cavity lifetime due to the intrinsic losses in the resonator, τ_{ext} is the photon cavity lifetime due to the finite coupling to the output waveguide, h is Plank's constant, and ν is the lasing frequency. τ_e is the recombination rate of the electron-hole pairs and includes both the radiative recombination rate (into all modes) and the non-radiative recombination rate. Since the quantum-wells interact with many modes other than lasing mode, this rate is largely independent of the optical design. The symmetry in Equations 2.4 and 2.5 indicates that each stimulated emission event causes electron hole pair to recombine radiatively while emitting one photon into the lasing mode.

In steady state, the output power of the laser can be written in terms of dimensionless quantities:

$$P_{\text{out}} = P_0 \cdot \frac{\gamma}{\gamma + 1} \left(\frac{I}{I_{\text{tr}}} - (1 + \chi(1 + \gamma)) \right), \quad (2.7)$$

where

- $P_0 \equiv h\nu/\tau_e$ is a convenient constant.
- $I_{\text{tr}} \equiv q\bar{N}/\tau_e$ is the transparency current of the quantum wells. This is independent of the thickness of the quantum noise control layer.

- $\gamma \equiv \tau_{\text{int}}/\tau_{\text{ext}} = Q_{\text{int}}/Q_{\text{ext}}$ is the over-coupling factor.
- $N_{\text{th0}} \equiv 1/g\tau_{\text{int}}$ is the number of electrons at threshold with no external coupling ($Q_{\text{ext}} \rightarrow \infty$).
- $\chi \equiv N_{\text{th0}}/\bar{N}$ is the minimum inversion fraction to reach the lasing condition in the case that $\tau_{\text{ext}} \rightarrow \infty$.

Equation 2.7 groups the intrinsic photon cavity lifetime (τ_{int}) and the modal gain (g) into a single variable (χ). As discussed in Section 2.2, the photon cavity lifetime τ_{int} and the modal gain g are directly affected by the thickness of the quantum noise control layer. For moderate thickness of the quantum noise control layer ($t_{\text{QNCL}} < 150$ nm), in the case that the intrinsic losses are dominated by the losses of the InGaAsP layer and τ_{int} can be written as:

$$\tau_{\text{int}}(t_{\text{ox}}) = \tau_{\text{int}}(0) \cdot \frac{\Gamma_{\text{InGaAsP}}(t_{\text{ox}} = 0)}{\Gamma_{\text{InGaAsP}}(t_{\text{ox}})}. \quad (2.8)$$

The temporal differential gain g (equal to $W_{\text{spont}}^{(l)}$) is proportional to the confinement factor in the quantum well layer of the resonator. Numerical simulations (Figure 2.5b) indicate that the confinement factor in the quantum wells is proportional to that of the InGaAsP. This is due to the exponential nature of the field in the quantum wells. g can thus be written in terms of the confinement factor in the InGaAsP:

$$g(t_{\text{ox}}) = g_0 \cdot \frac{\Gamma_{\text{InGaAsP}}(t_{\text{ox}})}{\Gamma_{\text{InGaAsP}}(t_{\text{ox}} = 0)}. \quad (2.9)$$

In this limit, χ , and thus the minimum threshold of the laser, is *independent* of the thickness of the quantum noise control layer.

The output power (P_{out}) is now only a function of the over-coupling factor $Q_{\text{int}}/Q_{\text{ext}}$. If this factor is kept constant as t_{QNCL} is varied, the output power of the lasers can be kept constant. We can break down the effect of the over-coupling factor into two different phenomena. The first is that it changes the slope efficiency of the laser: $\frac{\gamma}{1+\gamma}$ implies that if the laser is over-coupled, the useful output power becomes the dominant optical loss mechanism enabling the slope efficiency to approach unity. The second is the effect on the threshold current seen in $\chi(1 + \gamma)$. If the external coupling is large compared to the intrinsic losses, the threshold of the lasing mode can increase. The external losses are controlled by changing the length of the Bragg mirrors on either side of the resonator defect and are defined lithographically when patterning the optical resonator in silicon.

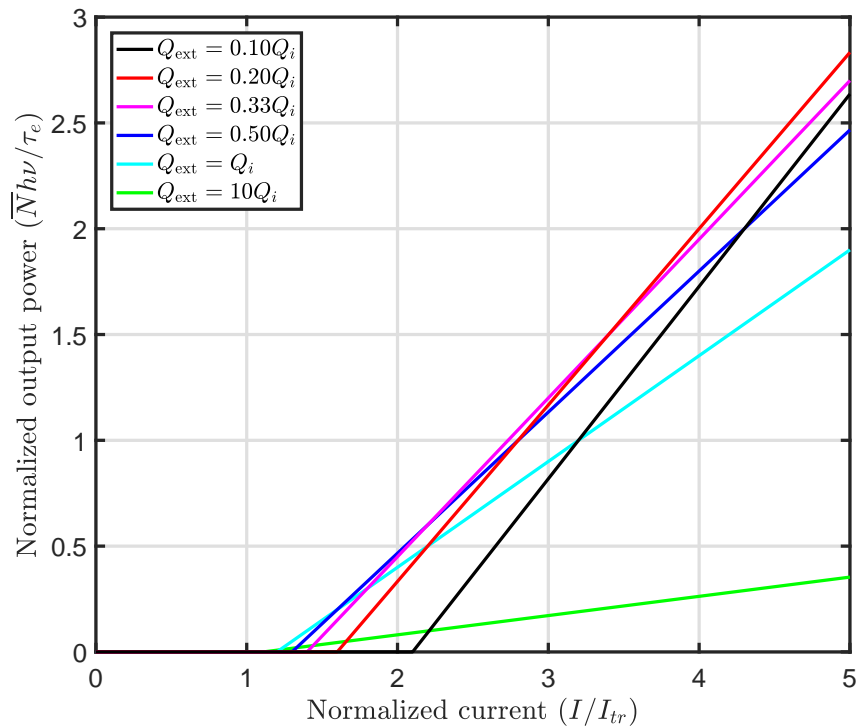


Figure 2.7: Normalized output power as a function of the normalized current (I/I_{tr}) for various values of the external coupling quality factor. We note that for $I/I_{tr} \approx 4$, the optimal value for Q_{ext} is between $0.3Q_i$ and $0.5Q_i$. For $Q_{ext} = Q_i$, often known as critical coupling, the output power is reduced by up to 25% of the optimal value.

We plot the normalized output power as a function of the normalized pump current for various values of the external quality factor in Figure 2.7. We find that for an operating current of $\approx 4I_{th}$, Q_{ext} should take a value between $0.3Q_i$ and $0.5Q_i$ to maintain a large total quality factor and high output power. In the under-coupled regime, $Q_{ext} \gg Q_i$, the output power is greatly diminished. Figure 2.8 summarizes the total Q as a function of $\gamma = Q_{ext}/Q_i$ as well as the output power for $I = 4I_{tr}$.

2.4 Final platform design parameters

For the remainder of this thesis, we will consider lasers with two different thicknesses of quantum noise control layers: 50 nm and 90 nm. The quality factor and other important design parameters for the lasers are summarized in Table 2.1. The dimensions and simulation of the transmission spectra of a resonator with quality factor 1×10^5 are shown in Figure 2.9 showing the predicted location of the mode with respect to the band edge and Bragg frequency of the mirrors.

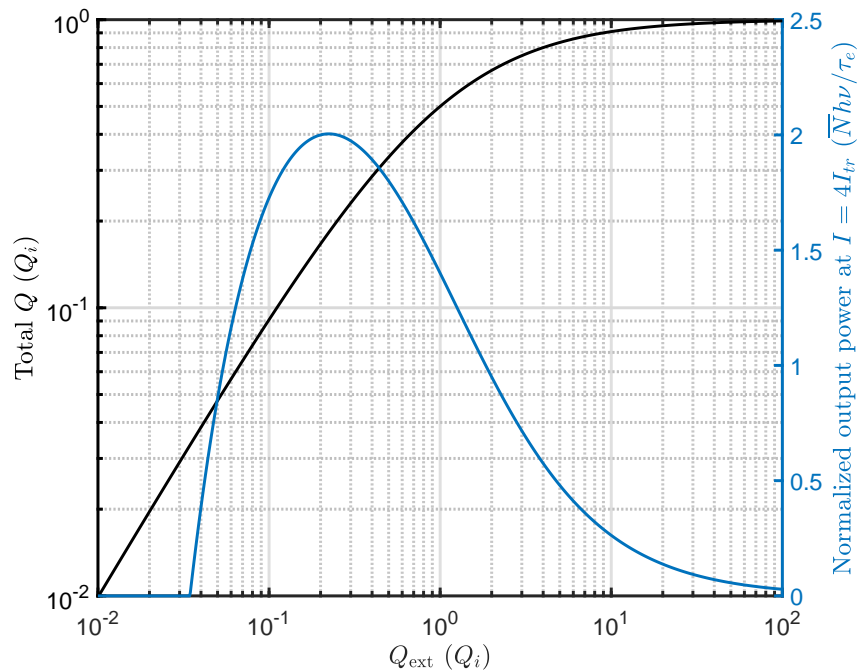


Figure 2.8: Normalized output power as a function of the normalized current (I/I_{tr}) for various values of the external coupling quality factor. We note that for $I/I_{tr} \approx I_{tr}$, the optimal value for Q_{ext} is between $0.3Q_i$ and $0.5Q_i$. For $Q_{ext} = Q_i$, often known as critical coupling, the output power is reduced by 25% of the optimal value.

Parameter	Value
Grating hole pitch	235, 237.5, 240 nm
Number of grating holes in defect (two sides)	1000
Waveguide etch width	2.5 μm
Etch depth (in silicon)	60 μm
Hole size in mirror	300 nm \times 120 nm
Minimum hole size in defect (donor mode)	225 nm \times 120 nm
Maximum hole size in defect (acceptor mode)	515 nm \times 120 nm

Table 2.1: High-Q resonator parameters.

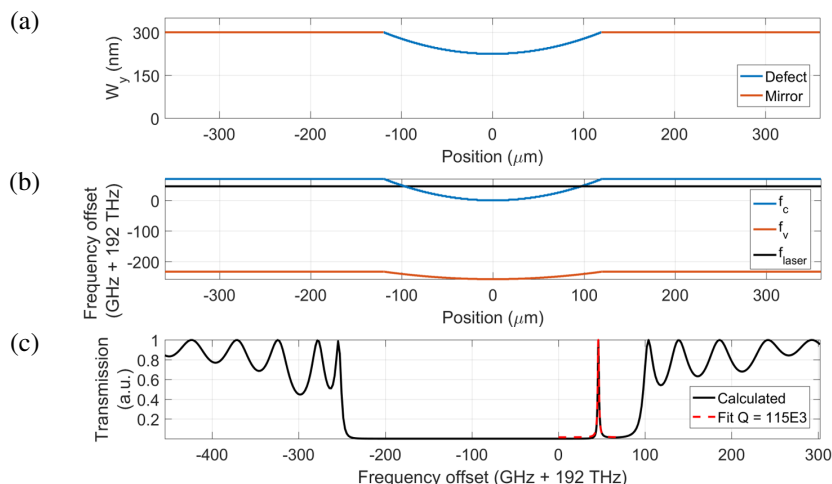


Figure 2.9: a) Width of the grating throughout the resonator as a function of the position away from the center of the defect. b) Band edges of the unit cell as a function of the position along the grating. The black line shows the location of the optical mode with respect to the center of the band gap. c) Simulated transmission spectrum obtained using coupled mode equations.

2.5 Conclusions

We have summarized the basic platform parameters for the high-coherence lasers that will be studied in the next two chapters. We discussed how engineering the fraction of the optical mode that resides in the silicon and the InGaAsP using a thin layer of silicon dioxide can increase the intrinsic quality factor of the resonator by orders of magnitude. It has been shown that the quantum limited frequency noise power spectral density is decreased by a factor proportional to the square of the quality factor of the resonator ($\delta\nu_{\text{ST}} \propto Q^{-2}$). Finally, we argued that the output power of well designed QNCL lasers is independent of the thickness of the QNCL in the regime where the quality factor is limited by the losses in the III-V. In the following chapters, we will explore how flip chip bonding can help increase the operating temperature of these lasers. Finally, we will show how these lasers are inherently less sensitive to optical feedback compared to their all-III-V counterparts.

THERMAL PROPERTIES OF HIGH-Q SILICON/III-V LASERS

In this chapter, we explore the thermal considerations that need to be taken when designing quantum noise controlled lasers. We explore what strategies may be undertaken to decrease the effects of the generated heat on the performance of the lasers and the challenges involved in our high-Q silicon/III-V platform. We model the thermal properties of the lasers using the 2D heat equation to estimate the temperature rise at the quantum wells, then propose and demonstrate how flip-chip bonding the lasers to a ceramic ceramic submount can greatly improve the thermal properties of the lasers.

We find that the buried oxide layer adds significant thermal impedance to the structure. On the other hand, the thick p-mesa structure in our lasers acts as a heat spreader decreasing the thermal impedance of the lasers. To further decrease the thermal impedance of the laser, and thus decrease the rise in temperature in the active layer, we propose and demonstrate how flip-chip bonding to a ceramic submount can increase the operating current from ≈ 200 to 300 mA. We show that flip-chip bonding can greatly improve the performance of lasers with thicker quantum noise control layers by circumventing the QNCL layer – another layer of high thermal impedance SiO_2 .

3.1 Thermal characteristic of semiconductor lasers

Semiconductor lasers are characterized by two important temperatures: T_0 , the characteristic temperature and T_1 , the above threshold characteristic temperature [55]. The characteristic temperature describes how the threshold current is affected by the temperature of the laser is given by the empirical value of T_0 that best describes

$$I_{\text{th}}(T) = I_0 e^{T/T_0}. \quad (3.1)$$

The above threshold characteristic temperature describes how the slope efficiency of the laser is affected when the temperature increases. It relates the above threshold current ($I_p = I - I_{\text{th}}$) to the operating temperature of the laser and T_1 :

$$I - I_{\text{th}}(T) \Big|_{P=P_0} = I_P(0) e^{T/T_1}. \quad (3.2)$$

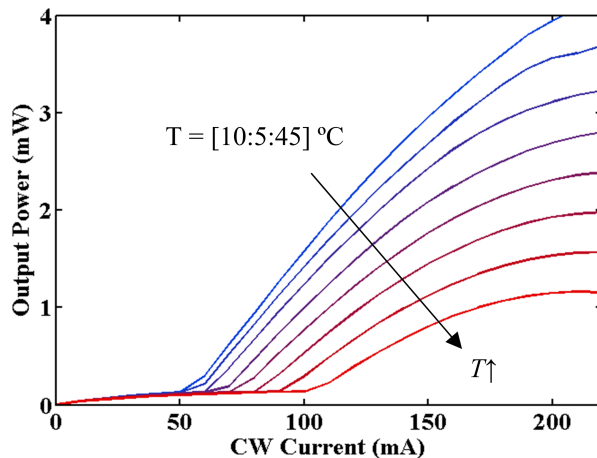


Figure 3.1: Light current characteristic of a 50 nm QNCL laser when the stage temperature is varied. The laser has a value of 51 °C and 81 °C for T_0 and T_1 respectively.

Figure 3.1 shows the light-current characteristics of a laser with a QNCL thickness of 50 nm as the stage temperature is varied. This particular laser has a value of 51 °C and 81 °C for T_0 and T_1 respectively. The thermal properties can be improved by using quantum dots, having reported characteristic temperatures as high as 161 K [56], but these typically have lower material gain than their quantum well counterparts, making them challenging to use [57]. It is henceforth desirable to improve the thermal performance of the lasers without changing the materials used for the optical waveguide and gain medium.

When current flows through the laser, heat is generated in the active medium causing the temperature of the laser to rise proportionally to the thermal impedance between the heat sources and the temperature controlled stage. The rise in temperature under load limits the maximum drive current of the laser setting upper bounds on the output power of the device.

3.2 Thermal challenges for heterogeneously integrated lasers

In Chapter 2, we discussed how integrating III-V material on silicon could be used to create semiconductor lasers with a narrow linewidth. In Chapter 4 we discuss how these same lasers are resilient to optical feedback and avoid the coherence collapse regime. It is therefore desirable to devise strategies where the heat generated by the gain medium does not significantly affect the performance of the lasers.

Our heterogeneously integrated lasers are normally mounted to a temperature controlled copper block by placing the lasers down on their silicon handle. This exposes

the electrical p and n contacts on the InGaAsP for straightforward electrical and optical testing. The main challenge in operating these lasers in this fashion is that the heat source, the emitting InGaAsP, and the copper heat sink, are separated by the buried SiO₂, a thermally insulating material. This increases the temperature of the quantum wells compared to the case of an all III-V laser where the thick buried oxide layer does not exist. Furthermore, the small air gap used to define the ridge silicon waveguide also offers additional thermal insulation.

Two challenges exist in moving away from sinking the heat through the silicon handle. First, the buried oxide cannot be made much thinner than 1 μm since it would cause increased leakage of the optical mode into the substrate. Second, because all electrical contacts are on the same side of the wafer, traditional epi-side down flip-chip bonding used to bond lasers onto submounts cannot be done without a matching submount design [58]. Other methods of thermal management have had encouraging results (e.g. thermal shunts [59]) but require additional processing steps before initial testing is possible.

To this end, a submount, made of aluminum nitride (AlN), a thermally conductive ceramic, is used to create a direct thermal path between the quantum wells and the temperature controlled heat sink. In the following sections, we will simulate the thermal impedance of the lasers before as they are without any thermal management strategy, and after flip-chip bonding to a ceramic submount. Using a patterned submount allows the lasers to be tested without adding any additional complexity to the fabrication of high-coherence silicon/III-V lasers.

3.3 Thermal impedance of high-coherence silicon III-V lasers

In this section we consider the thermal impedance of our heterogeneously integrated silicon III-V lasers. To simplify the analysis, we will consider a high-coherence laser with a nominal length of 1 mm, with the geometry described in Section 2.4. The total rise in temperature at the quantum wells T_{QW} can be written as a sum of the three sources of heat q , the p, n, and quantum wells (QW), multiplied by their respective thermal impedance $R_{x \rightarrow \text{QW}}$ as seen by the quantum wells:

$$T_{\text{QW}} = R_{\text{n} \rightarrow \text{QW}} q_{\text{n}} + R_{\text{QW} \rightarrow \text{QW}} q_{\text{QW}} + R_{\text{p} \rightarrow \text{QW}} q_{\text{p}}. \quad (3.3)$$

While the p-layers and quantum well layers are located directly above the optical mode in the waveguide, the n-layer is distributed over an ≈ 90 μm channel and as such will have a different thermal path through the device. We simulate the 2D thermal diffusion equation ($-k\nabla T = q$, where k is the local thermal conductivity,

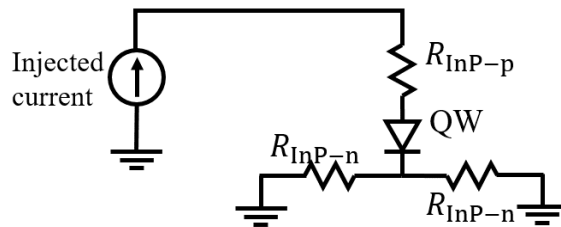


Figure 3.2: The electrical model for the three different sources of heat in the system. The p and n cladding layers are modeled as resistors while the heat generated in the quantum wells is modeled as the energy lost in an ideal diode.

T is the local temperature, and ∇ indicates the gradient, and q is the generated heat density) using a finite element solver (Comsol 5.1) to estimate the temperature of the active layers in the epitaxially grown InGaAsP when a current is applied. We will consider two structures, the first being the laser placed silicon side down onto a temperature controlled copper block, and the second being the laser flip-chip bonded onto an AlN submount designed to decrease the thermal impedance of the device.

Thermal sources

On average, the lasers that we fabricated had a turn on voltage of roughly 0.9 V and a small signal resistance of approximately 11 Ω . The heat generated in the p and n layers is assumed to be ohmic ($q = I^2R$, where q is the total heat, I is the current through the p or n cladding, and R is the resistance of the layer) and the heat generated in the quantum wells is taken to be the product of the driving current and the turn on voltage. The electrical model of our QNCL lasers is shown in Figure 3.2.

The theoretical resistivity of the p and n layers can be estimated by considering the mobility of the majority carriers in the respective layers. We assume a hole mobility of $30 \text{ cm}^2\text{V}^{-1}\text{s}^{-1}$ for the heavily doped p-layer [60] having an average dopant concentration of $\approx 0.5 \times 10^{18} \text{ cm}^{-3}$ in the channel. This gives the p-channel an average resistivity of $520 \text{ }\Omega/\square$. For the $1.7 \text{ }\mu\text{m}$ thick p-layer, and a 1 mm long laser, the resistance of the p-channel is estimated to be approximately $0.9 \text{ }\Omega$. To calculate the heat generated in the two n-channels, we assume an n channel with a mobility of $1250 \text{ cm}^2\text{V}^{-1}\text{s}^{-1}$, giving the 110 nm thick n-channel an approximate sheet resistivity of $435 \text{ }\Omega/\square$. For a 1 mm laser, this corresponds to a resistance of approximately $20 \text{ }\Omega$ per n-channel that connects the quantum wells near the waveguide to the metal pads on either the side of the device. Together, the p and n

Layer name	Material	Thermal conductivity (W/cm °C)	Thickness
Aluminum nitride submount	AlN	1.70	150 μm
Gold tin solder (80/20)	AuSn	0.68	$\approx 4 \mu\text{m}$
Gold contacts	Au	3.17	200 nm
p-doped InP	InP	0.70	1.7 μm
Separate confinement layers	InGaAsP	0.15	80 nm
Quantum well	InGaAsP	0.10	235 nm
Separate confinement layers	InGaAsP	0.15	80 nm
n-doped InP	InP	0.70	150 nm
Quantum noise control layer	SiO ₂	0.011	0 \rightarrow 150 nm
Silicon device layer	Si	1.3	500 nm
Buried oxide layer	SiO ₂	0.011	1 μm
Silicon handle layer	Si	1.3	150 μm

Table 3.1: Summary of the thermal conductivities used to simulate the temperature at the quantum wells for the high-coherence lasers. Note that many of the small layers in the epi-InGaAsP wafer have been combined to speed up the simulation. Values for the conductivity of the AlN were taken from [61] as the exact thermal conductivity changes from manufacturer to manufacturer of the ceramic. The thermal conductivity of the InP, silicon, gold, and silicon dioxide were taken from the built-in materials in Comsol while the thermal conductivity of the quantum well layers is taken from [62].

channels give the total device a resistance of approximately 11 Ω . The heat generated in the quantum wells is assumed to be equal to the current injected multiplied by the voltage drop across the diode (0.9 V). While the length of the lasers varies by a few hundred microns, we consider the average laser with a nominal length of 1 mm to help guide the thermal design of the laser.

Table 3.1 summarizes the thermal conductivity used in the different layers during the thermal simulations.

Figure 3.3 shows a 2D cross-section of the approximate generated heat in the III-V structure when the laser is operated at 200 mA. While the total heat generated by the n-layer is comparable to the heat generated by the quantum wells, the n-channel is distributed greatly decreasing the heat density in the thin layer as summarized in Figure 3.3c.

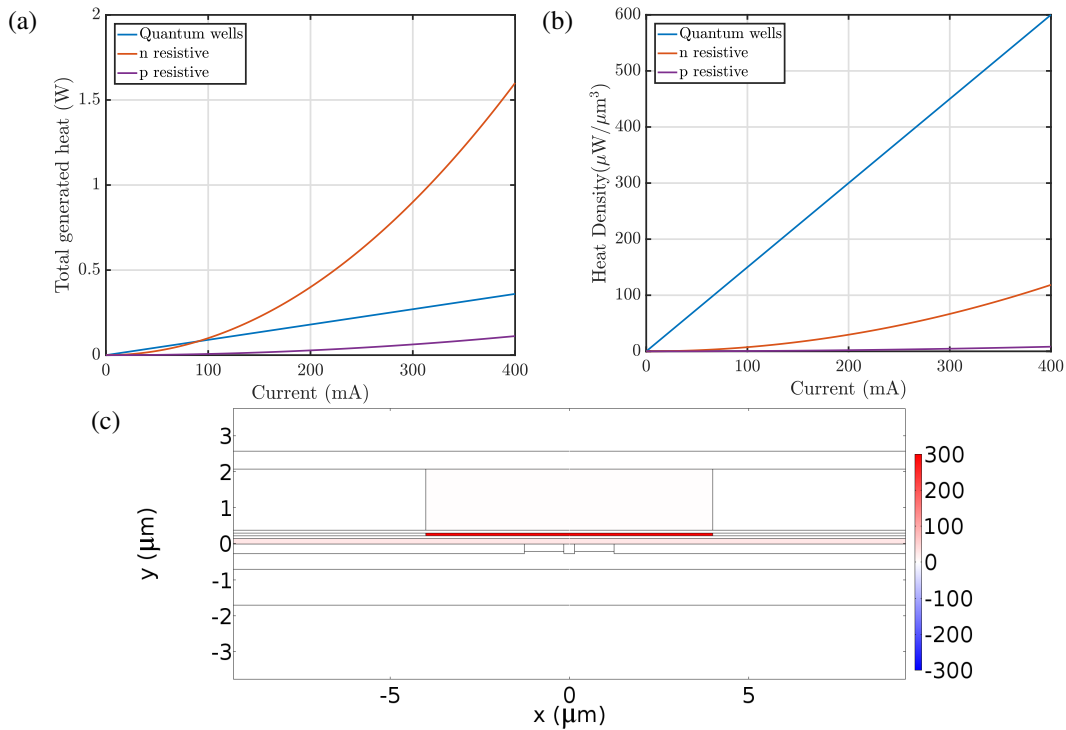


Figure 3.3: a) Total heat generated by the p, n, and quantum well layers in the laser. b) Heat density generated by the p, n, and quantum well layers in. c) 2D profile of the heat density generated in the laser for a drive current of 200 mA in $\mu\text{W}/\mu\text{m}^3$.

Thermal simulations

To analyze the contribution of the different heat sources, we conduct separate thermal simulations where each of the three identified sources are simulated individually. We begin by analyzing the contribution of the p-contact region. The heat generated in this layer is found to only increase the temperature of the quantum wells by less than 1°C , at 200 mA, an insignificant amount considering that the lasers have characteristic temperatures of 51°C and 80°C . Results from the 2D simulation of the temperature and heat flux in the laser are shown in Figure 3.4a.

The simulations of the temperature increase in the laser when considering the heat generated from the n-layer are shown in Figure 3.4b when the laser is operated at 200 mA. Two interesting aspects are observed. First, the hottest region in the laser is not in the center of the waveguide, but rather near the center of the trench used to define the optical waveguide where the III-V does not make direct contact with the QNCL. Second, although heat is generated through the $90\ \mu\text{m}$ contact layer, the heat flux outside the central $10\ \mu\text{m}$ flows away from the optical mode toward the unetched region outside the trench. This indicates that the $1.9\ \mu\text{m}$ thick mesa acts

as a low impedance path between the heat generated in the n-contact layer to either side of the laser. The total increase in temperature due to the heat generated in the n-contact is estimated to be 6 °C.

Finally, the quantum wells generate a significant amount of heat from non-radiative recombination that cannot be ignored. In fact, below 200 mA, the quantum wells are the dominant source of heat in the laser as shown in Figure 3.3c. At 200 mA, the heat generated at the quantum wells contributes to an increase of approximately 6 °C in the active region. As was the case for the heat generated in the n-layer, we also observe that heat flows from the center of the waveguide to regions on either side of the trench, utilizing the 1.9 μm mesa as a heat spreader.

Figure 3.4 shows the 2D profile of the temperature across the facet of the laser while Figure 3.5b summarizes the temperature of the quantum wells assuming a quantum noise control layer of 100 nm as a function of the distance from the center of the waveguide for currents of 50 mA, 100 mA, and 200 mA and breaks down the contribution from the three different heat sources. Figure 3.5a shows the temperature along the vertical dimension at the center of the waveguide when the temperature of the silicon handle, assumed to be 150 μm thick, is held at a constant temperature of 293 K. As expected, a large temperature gradient is established between the burier silicon dioxide layer. For an operating current of 200 mA, the 1 μm of buried oxide increases the temperature of the device by approximately 7 °C while the 100 nm quantum noise control layer increases the temperature of the device by 2 °C. Using the above simulation, we can determine the thermal impedance for all three sources of heat to be 15, 32 and 33 °C/W for the n-contact layer, p-contact layer, and quantum wells respectively.

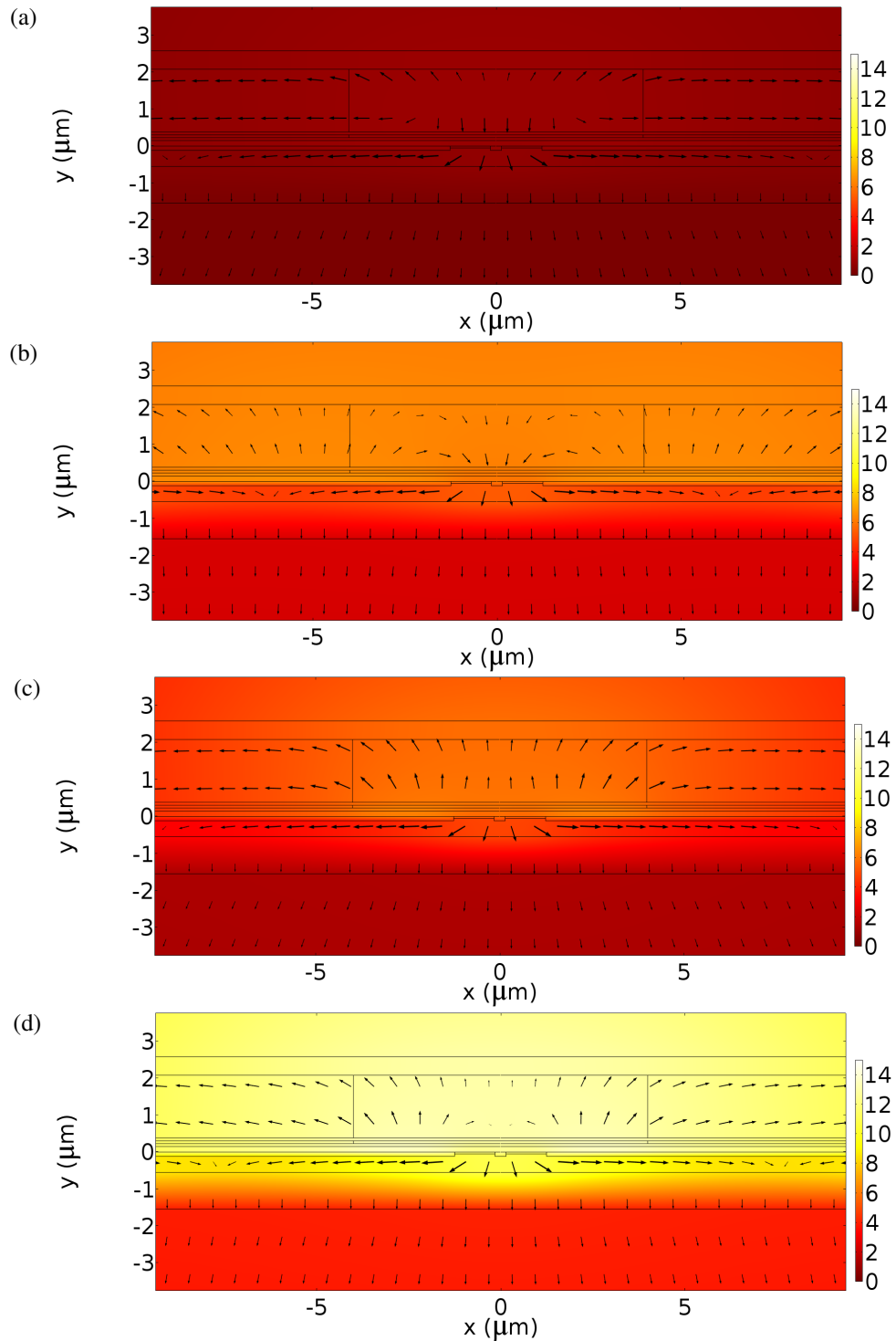


Figure 3.4: Temperature profile (color) and heat flux (arrows) across the laser when a current of 200 mA is applied to the laser. The contribution of the temperature rise is broken up between the 3 different thermal sources, the finite resistivity of the p, n, and voltage drop across the quantum well layer are shown in a), b), and c), respectively, while the total temperature rise is shown in d).

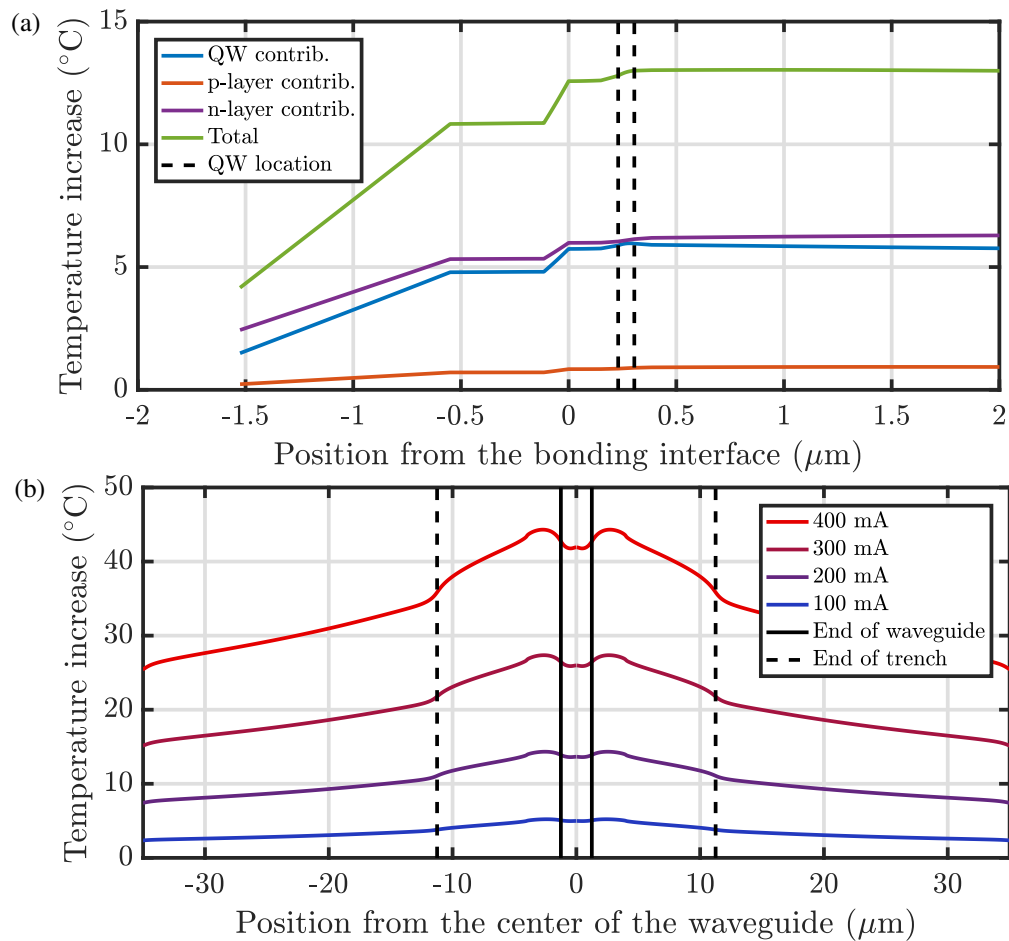


Figure 3.5: a) Temperature along the center of the waveguide ($x = 0$) as a function of the position from the III-V bonding interface. b) Temperature along the bottom of the quantum wells for different drive currents.

The effect of the mesa-width on the temperature of the quantum wells

In this section, we consider the effect of the mesa width on the temperature at the quantum wells in the case where the device is placed with the silicon side down onto the copper heat sink. While decreasing the length of the n-contact layer reduces the total resistance of the channel, since the generated heat density remains constant, little effect is predicted at the photon generating quantum wells. In fact, since the mesa acts as a heat spreader, a narrow mesa can actually increase the temperature at the quantum wells.

Figure 3.6c shows how the temperature of the quantum wells changes when the width of the III-V mesa is varied between 10 μm and 70 μm when the laser is operated at 200 mA, assuming that the trench ends 11.25 μm away from the center of the waveguide. While the temperature profile at the center of the quantum wells remains constant for mesa widths between 35 and 70 μm , it rapidly increases when the mesa becomes narrower than the trench (22.5 μm wide). This is because the un-etched silicon outside of the trench can no longer be used as a lower impedance thermal path for the heat generated in the quantum wells, as shown in Figure 3.6b. In this case, the generated heat must to be funneled through the narrow 2.5 μm waveguide, increasing the temperature of the quantum wells. Since the choice of the mesa width makes little difference in the predicted temperature of the quantum wells, it is desirable to keep the mesa width larger than $\approx 50 \mu\text{m}$ to ease making electrical contact with the lasers with larger DC and RF probes, and to ease flip-chip bonding.

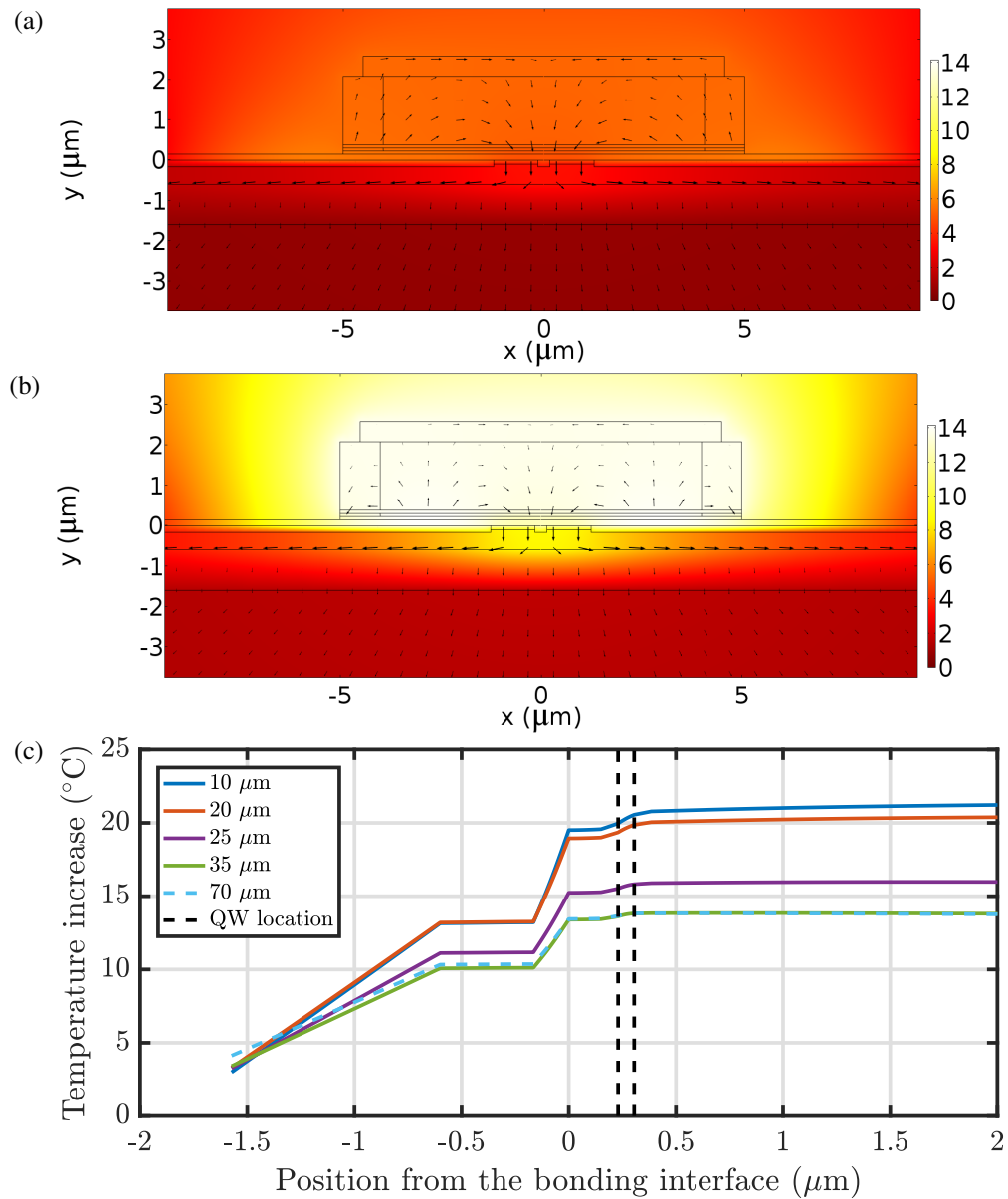


Figure 3.6: 2D thermal simulation of the temperature increase (color in $^{\circ}\text{C}$) and thermal gradient (arrows) considering only the heat generated by the n contact layer in (a) and by the quantum wells (b) when the mesa is defined to be 10 μm wide instead of 70 μm wide as designed. The n-metal layers have been brought closer accordingly and are start at 10 μm away from the end of the mesa. c) Temperature profile across the center of the waveguide when the width of the mesa is varied.

The effect of quantum noise control on the temperature of the laser

Finally, we consider the effect of increasing the oxide thickness between the silicon device layer and the InGaAsP structure on the temperature of the quantum wells known as the quantum noise control layer. As shown for the case of 100 nm thick quantum noise control layer, a temperature increase of 2 to 3 degrees is predicted across the thin SiO₂ layer. Figure 3.7 shows the temperature profile across the center of the waveguide as the thickness of the SiO₂ QNCL is increased. A laser with a 150 nm QNCL has an average thermal impedance $\approx 25\%$ larger than a heterogeneously integrated laser without a QNCL between the silicon and the III-V. While this is not detrimental to the performance of QNCL lasers, it is there desirable to find a strategy to mitigate the effect of the QNCL on the temperature of the laser. This same technique could also be applicable to optical platforms that make use of even thicker oxide for multiple layers of waveguides [63]–[67] proposed for massive photonic integration.

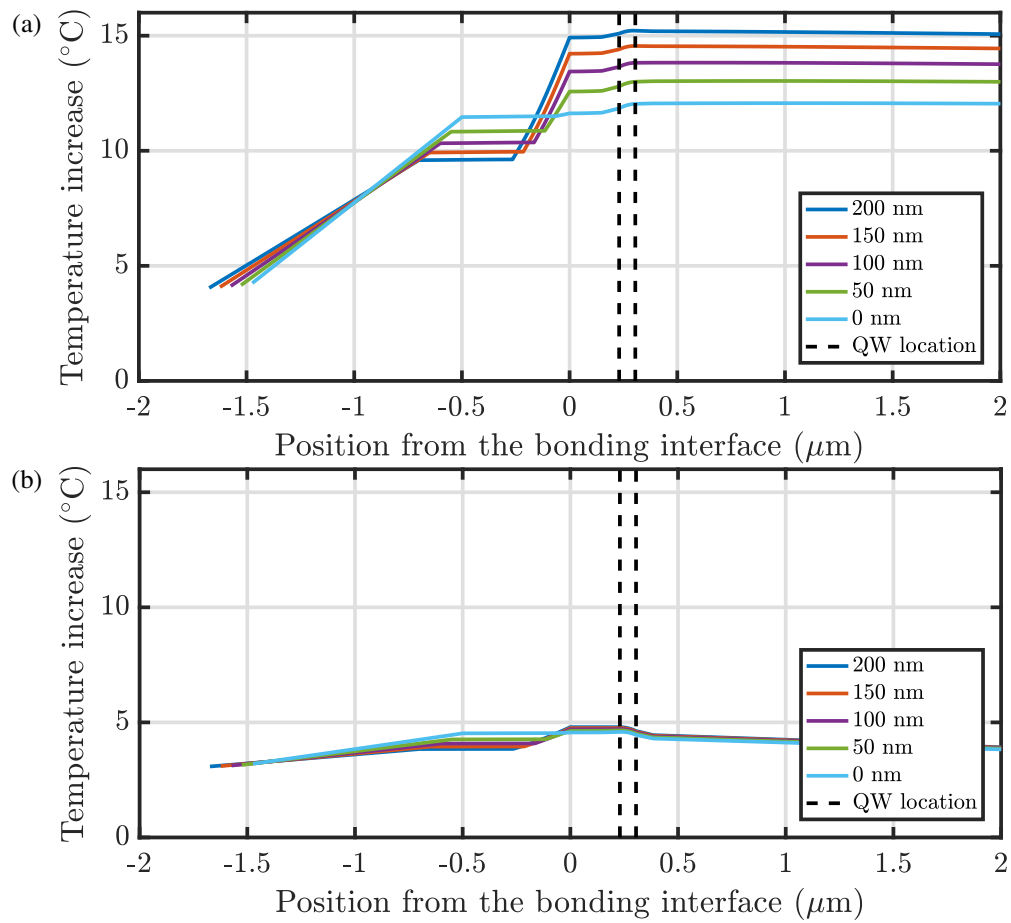


Figure 3.7: a) Temperature profile across the center of the waveguide when the width of the thickness of the quantum noise control layer is varied. 0 microm corresponds to the Si/III-V bonding interface. b) Temperature profile across the center of the waveguide with flip-chip bonding the thickness of the QNCL is varied.

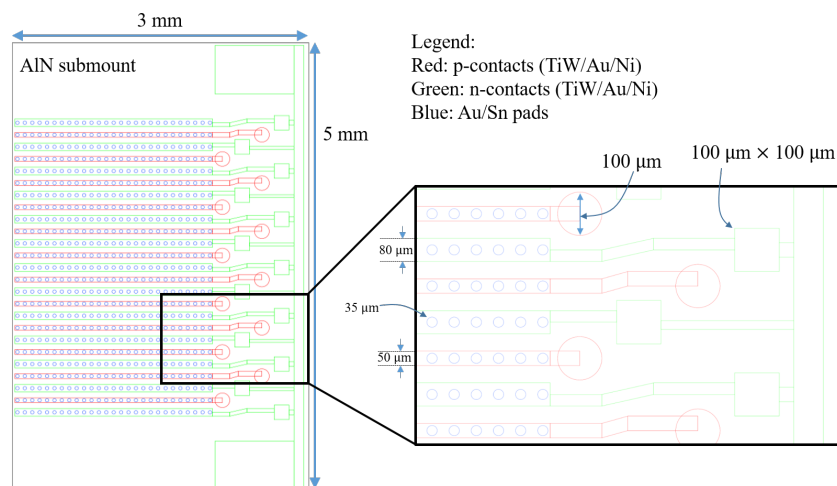


Figure 3.8: Schematic of the aluminum nitride (AlN) submount to which a bar of 12 lasers can be flip-chip bonded on to.

3.4 Flip-chip bonding for decreased thermal impedance

To decrease the thermal impedance of the devices, we design aluminum nitride (AlN) submounts to which the cleaved laser bars can be flip-chip bonded to enable lower thermal impedance path between the lasers and the temperature controlled copper heat sink. These submounts also make the individual laser bars compatible with wire-bonding, a process typically requiring thermo-sonication and our previous attempt have proven to destroy the fragile mesa.

The submounts are designed to accommodate cleaved laser bars with 12 lasers with a pitch of $250\ \mu\text{m}$ between lasers, each laser having a length up to $2\ \text{mm}$. On the $150\ \mu\text{m}$ thick AlN submount, metal traces made of Ti/W, Au and Ni (with nominal thicknesses of $600\ \text{nm}$, $3\ \mu\text{m}$ and $100\ \text{nm}$ respectively) are deposited to match the p and n contact of the laser bars. All n-contacts are shorted together and large pads $100\ \mu\text{m}$ in diameter are included for each p and n contact to make contact with DC probes and for ease of wire bonding for further packaging. A schematic of the submount is shown in Figure 3.8 with the relevant dimensions labeled.

To bond to the III-V mesa structure, Au/Sn pads (80/20 in composition by weight), $35\ \mu\text{m}$ in diameter and $\approx 4\ \mu\text{m}$ thick, are deposited onto traces on the submount. Bonding is accomplished using a flip-chip bonder (Finetech Fineplacer Lambda) that ensures adequate the alignment between the submount and the laser bars as shown in Figure 3.10d. During the bonding procedure, the lasers are lowered onto the submount with $10\ \text{N}$ of force while the submount and laser bar are heated to $300\ ^\circ\text{C}$ (just above the eutectic temperature of $290\ ^\circ\text{C}$ for the Au/Sn alloy) for 15

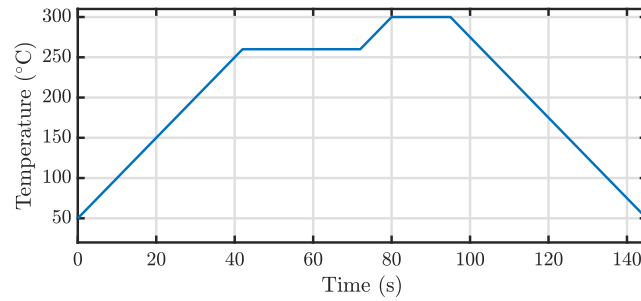


Figure 3.9: The bonding profile settings for the Fineplacer Lambda bonder used to bond the laser bar to the AlN submount.

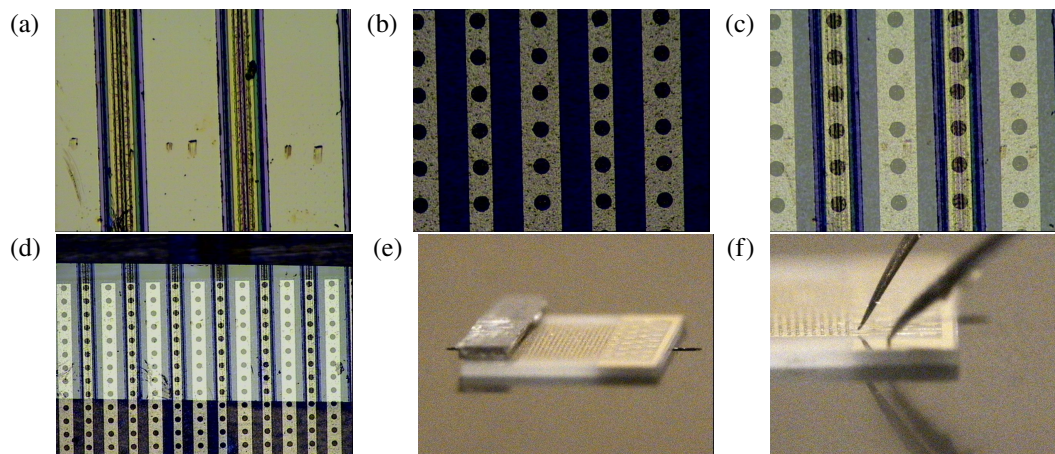


Figure 3.10: a-d) Different views of the device and submount before they are bonded during the alignment phase. A beam blocker can be positioned to hide either the device or the submount showing each in isolation. Figures c) and d) show the view from the camera when the beam blocker is not used showing how the p and n contacts of the devices are oriented when they are aligned. Figure d) shows the overhang of the lasers used to ensure that the output beam is unaffected by the submount. Figures e) and f) show side views of the device immediately after the bonding procedure is complete and how probes can be used to test the diode characteristics to ensure good contact between the laser and the submount.

seconds before cooling off. The temperature profile of the flip-chip bonder during the bonding process is shown in Figure 3.9. Images taken during the bonding procedure and resulting devices are shown in Figure 3.10.

Thermal simulations of the flip-chip bonded lasers

We repeat the previous simulations considering the case where a thermal pathway exists between the p and n metal contacts directly to a heat-sink through an AlN submount. We assume that after bonding, the Au/Sn layer makes contact with the p-contact metal over a width of 50 μm . Figure 3.11 shows the 2D thermal profile when the laser is flip-chip bonded and driven with 200 mA when considering all sources of heat and Figure 3.11c shows the thermal profile along the center of the waveguide as the driving current is varied. From these 2D simulations, we can estimate that the thermal impedance from the heat generated in the n-contact layer, p-contact layer, and quantum wells is 5.3, 10, and 13 $^{\circ}\text{C}/\text{W}$ respectively, a decrease by a factor of 2 to 3 for the different sources of heat compared to the case without flip-chip bonding. The simulations indicate that the temperature increase equivalent to that of the laser driven at 200 mA without flip-chip bonding is approximately equivalent to a laser with driven with 400 mA using an AlN submount.

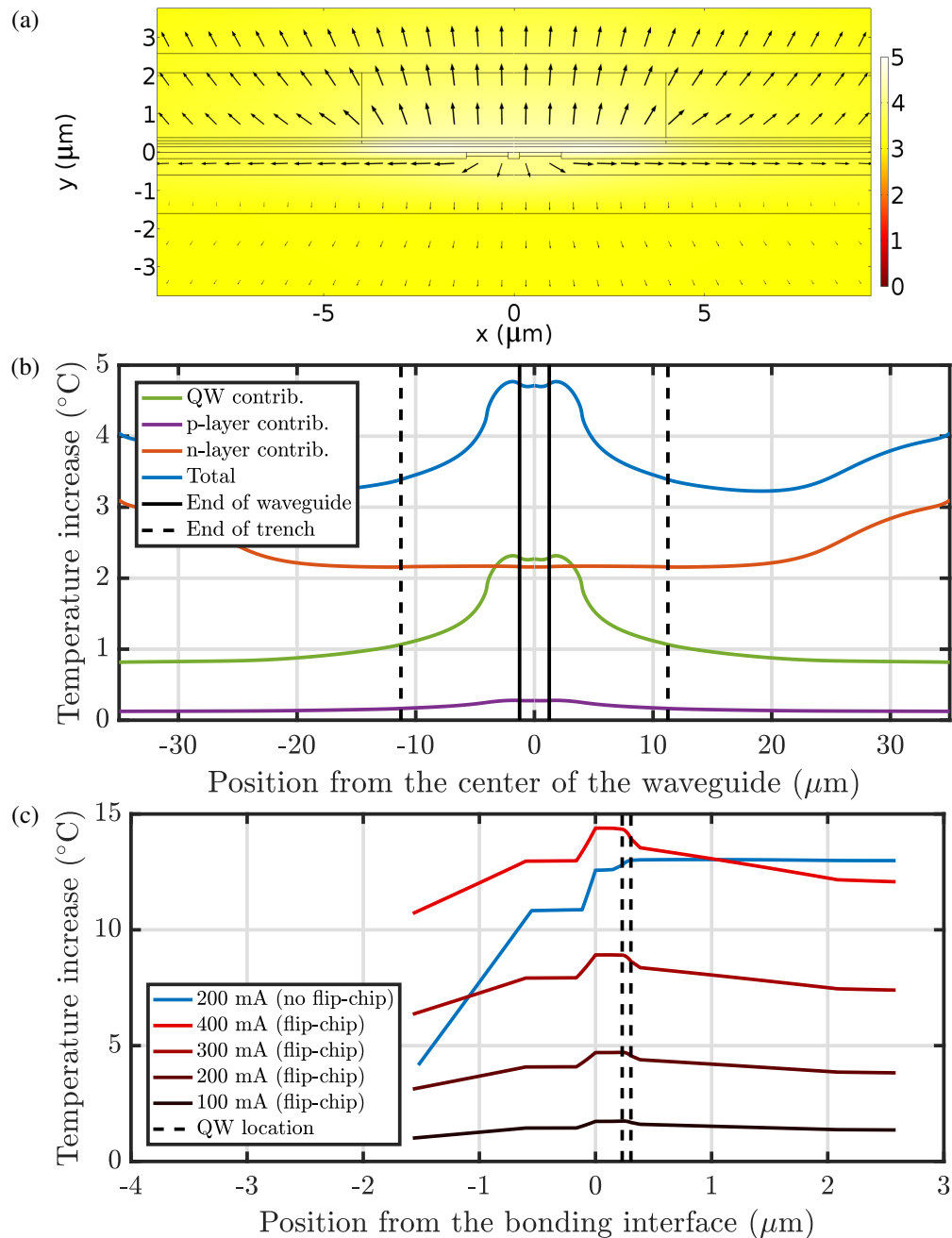


Figure 3.11: Thermal simulation results of a laser flip-chip bonded onto an AlN submount. Unless otherwise noted, the laser is driven with 200 mA of current. a) 2D thermal simulation of the laser when it is flip-chip bonded to an AlN submount. The submount makes thermal contact with a stage held at constant temperature near $y = +150 \mu\text{m}$. b) The temperature of the quantum wells as a function of the position from the center of the waveguide. The temperature increase due to the N-layer increases near the end of the mesa due to the fact that it can no longer spread laterally at that location. c) Temperature increase along $x = 0$ as a function of the driving current when flip-chip bonding is used. The result for the laser without flip-chip bonding for a current of 200 mA is included as a visual guide.

3.5 Flip-chip bonding results

We present the light-current characteristics of flip-chip bonded lasers before and after bonding them to AlN submounts. We consider both Fabry-Perot lasers, where the optical mode is uniform across the laser, and mode-gap lasers with different QNCL thicknesses.

Flip-chip bonding of Fabry-Perot lasers

Figure 3.12 summarizes the output characteristics of Fabry-Perot lasers before and after flip-chip bonding. All lasers were obtained from the same bar. The thickness of the silicon handle was approximately 150 μm thick. Before flip-chip bonding, the lasers interfaced a temperature controlled copper mount through the silicon handle and heat paste was used to ensure adequate thermal contact between the silicon handle and copper mount. After flip-chip bonding, the AlN was placed on the same temperature controlled copper mount with thermal paste to ensure good thermal contact between the AlN and copper block. The temperature of the copper stage is held at 20 $^{\circ}\text{C}$ for all experiments. On average, the thermal roll-off current for the FP lasers increased from 184 mA to 284 mA while increasing the maximum output power from an average 2.7 mW to an average maximum power of 10.4 mW.

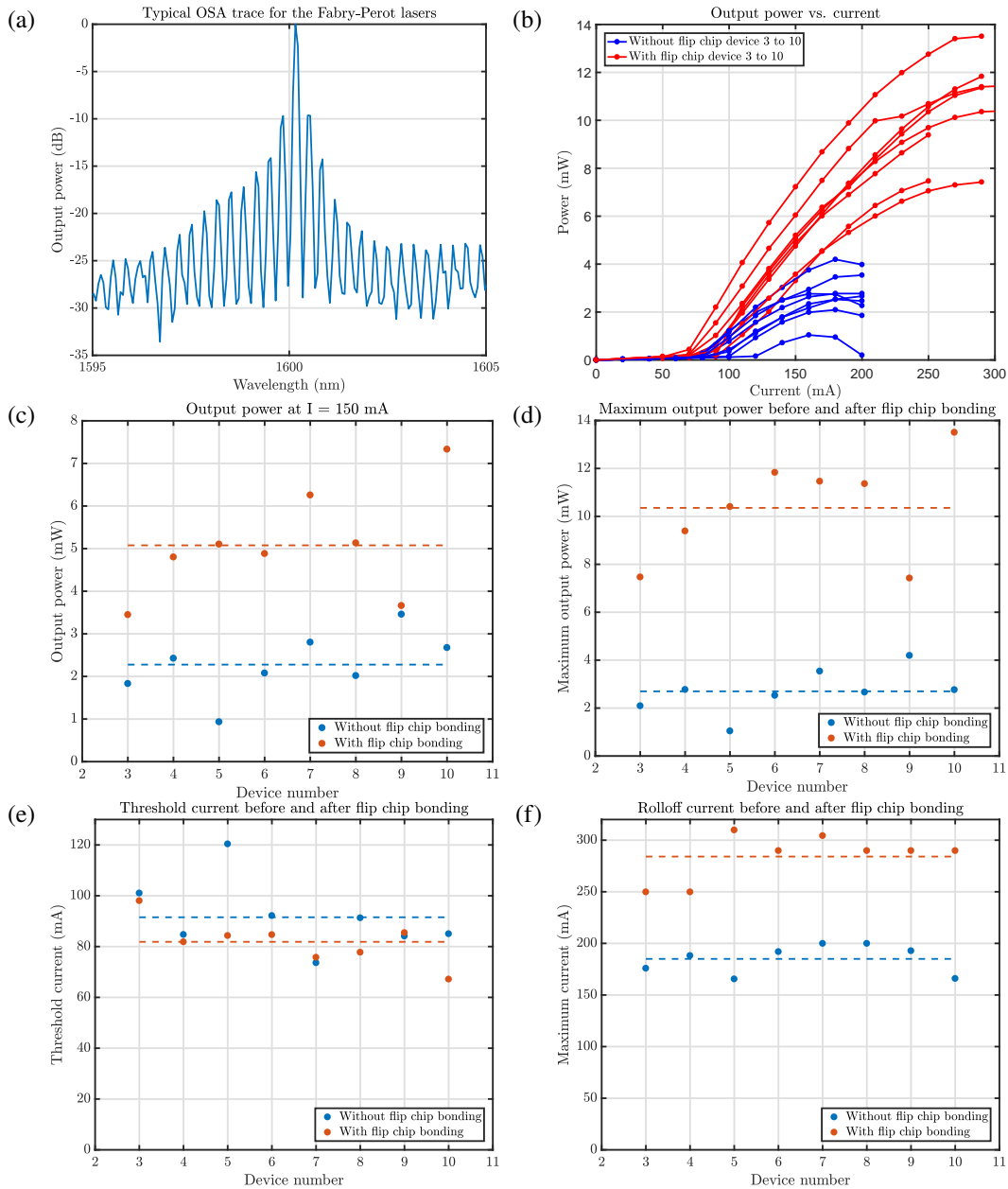


Figure 3.12: a) Typical OSA trace of the Fabry-Perot lasers above threshold. b) Luminosity vs. drive current for a bar of Fabry-Perot lasers before and after flip-chip bonding. c-f) Output power at 150 mA, maximum power, threshold current, and thermal roll-off current before (blue) and after (red) flip-chip bonding for 8 working lasers on a bar of 12 lasers. The dashed line shows the average property across the bar before and after flip-chip bonding.

Flip-chip bonding of single mode QNCL lasers

Figure 3.13 shows the results of various lasers (from different bars) that were successfully flip-chip bonded onto AlN submounts and their output power characteristics. As expected, the maximum output power and operating current of the lasers increased. One laser with an QNCL thickness of 120 nm only lased after flip-chip bonding. Few lasers also experienced a small increase in the threshold current. We attribute this to impartial bonding along the p and n contact which can lead to the mirror portion of the resonator being preferentially pumped, leading to a slightly larger threshold current. As was observed in the FP lasers, many of the lasers observed a markedly improved slope efficiency, allowing them to reach much larger output powers. Our simulations likely underestimated the temperature increase at the quantum wells. Taking the thermo-optic coefficient of silicon to be 1.8 K^{-1} [68], we estimate that the temperature in the silicon increased by $25 \text{ }^\circ\text{C}$ at the maximum operating current, slightly larger than the expected $\approx 15 \text{ }^\circ\text{C}$. This is attributed to imperfect thermal contact between the device and the temperature controlled stage.

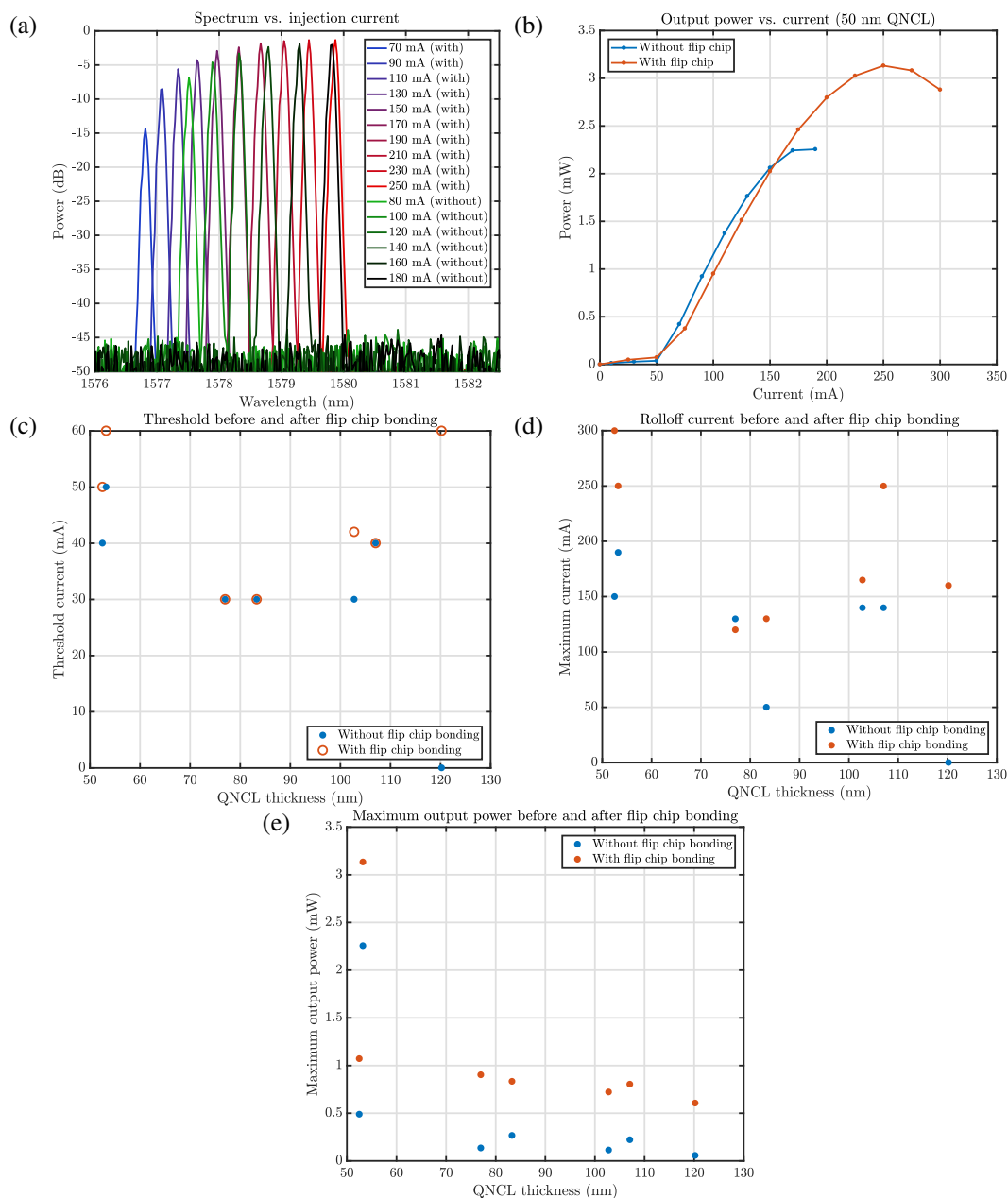


Figure 3.13: a) OSA trace of a flip-chip bonded laser with a 50 nm QNCL layer. b) Luminosity vs. drive current for a the laser shown in a) before and after flip-chip bonding. c-e) Maximum output power (one sided), threshold current, and thermal roll-off current before (blue) and after (red) flip-chip bonding for a variety of flip-chip bonded lasers with different QNCL layer thicknesses. The exact thickness of the QNCL was dithered on the plot to allow the unique identification of the lasers across different plots.

3.6 Flip-chip bonding limitations

While flip-chip bonding does avoid additional fabrications steps compared to alternative thermal management strategies for thermal management such as thermal shunts [59], it is not without its own drawbacks. The main challenge in flip-chip bonding involves the uniformity of bonding the device across its entire length. The AuSn 80/20 alloy leaches gold from the evaporated contacts to increasing composition of gold in the alloy, increasing the melting point [69]. This makes it difficult to reflow the solder in the case of non-planar contact during the initial the bonding process. Non-planar contact can cause the mirrors of the mode-gap resonator to be preferentially pumped and cause hot spots where bonding voids are present. Because the laser becomes enclosed on all sides after this procedure, it is difficult to diagnose the source of issues without destructively taking the lasers apart.

Finally, the analysis above has ignored the finite thermal impedance between the device under test and the temperature controlled stage. While efforts were made to use thermal paste to minimize the effects of small air gaps, we do not ignore that it can often have measurable effects on the device's performance.

3.7 Conclusions

In this chapter, we have developed a thermal model for our QNCL high-coherence lasers and modeled the temperature rise for lasers that where the heat is sunk through the silicon handle, and for lasers that are flip-chip bonded to an AlN submount. Flip-chip bonding to an AlN submount provides an excellent path for removing heat from the laser decreasing the thermal impedance of QNCL lasers by a factor of 2 to 3. Flip-chip bonding Fabry-Perot lasers has shown an increase of the driving current from 184 to 284 mA corresponding to an increase in the output power from 2.7 mW to 10.4 mW for approximately 1 mm long lasers. While single mode lasers only observed an output power increase between 1.4 and 2× using flip-chip bonding, this strategy promises to be important in more complex platforms that utilize increasingly thicker layers of buried oxide, or even multiple layers of waveguides to achieve larger optical device density.

Acknowledgments

We would like to acknowledge the help of Dr. Gustavo Rios in developing the bonding procedure used to bond the laser bars to the aluminum nitride submounts.

*Chapter 4***FEEDBACK SENSITIVITY OF HIGH-COHERENCE SI-III/V LASERS**

Optical reflections in communication and sensing systems are unavoidable and can cause the performance of lasers to degrade. Currently, the consistent performance of semiconductor lasers is only guaranteed through the use of optical isolators. These non-reciprocal optical devices inhibit reflections in the optical network from reaching the laser resonator, and thus decrease the laser sensitivity to optical feedback. Optical feedback has been studied both theoretically [21], [70], [71], and experimentally [72], [73] and it was shown that uncontrolled optical feedback can degrade the highly sought property of coherence in lasers for even mild levels of optical reflections.

In this chapter, we will explore how the optical feedback sensitivity of high-coherence QNCL lasers is affected as the thickness of the thin quantum noise control layer is increased. We find that, using the same technique we used to increase the coherence of the lasers, lasers can be engineered to be insensitive to large levels of optical feedback. The presented approach does not require integrated garnet materials on the optical platform making this a good strategy for future high density optical circuits [74], [75].

4.1 Optical feedback sensitivity review

We consider how undesired but unavoidable optical reflections affect single mode laser resonators where a single lasing mode exists with a large side mode suppression ratio. For lasers with two or more competing modes, or degenerate modes, as is the case for ring lasers, the main effect of optical feedback will be to break the degeneracy and cause one of the two competing modes to become dominant [76]. We therefore consider lasers designed around single mode resonators such as the mode gap resonators described in Chapter 2. We assume that the gain margin of the lasing mode is not significantly affected by the small level of optical feedback.

In the case of single mode resonators, the main effect of optical feedback can be modeled as changing the effective reflectivity of the output mirror [21] as shown graphically in Figure 4.1. For the case of weak feedback, the effective reflectivity of

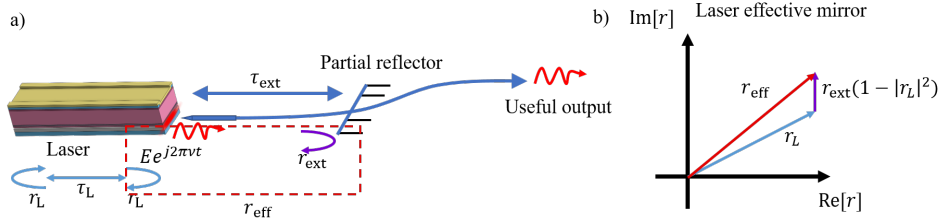


Figure 4.1: The effective reflectivity of a laser in the presence of an external reflector. The source of the partial reflector can be either a small piece of dust, a bad connector, an optical component with a finite reflection, a bad fiber splice, or even an unconnected fiber.

the resonator's output mirror (r_{eff}) is given by the sum of original reflectivity of the mirror (r_L) and the reflectivity of the external reflector (r_{ext}) viewed at the position of the laser's original mirror and can be written as

$$r_{\text{eff}} = r_L + r_{\text{ext}}(1 - |r_L|^2). \quad (4.1)$$

The reflectivity of the mode gap resonator evaluated at the frequency of the lasing mode can be found by considering the resonator as possessing two frequency dependent mirrors on the output side. The (complex) reflectivity of the two mirrors of our modegap resonator can be computed using the coupled mode equations by simulating the resonator as two halves each containing half the distributed defect as shown in Figure 4.2. The group delay can be found by solving the coupled mode equations [6] for each half the resonator. For our resonators, described in Table 2.1, the round trip time in the cavity is found to be approximately 6 ps, roughly equivalent to the round trip time of a Fabry-Perot cavity the length of the distributed defect. The advantage of the mode gap resonator is that the mirrors are of extremely high reflectivity and the nature of the distributed defect dictates that only a *single* high quality mode may exist. The reflectivity of the mirror as a function of the mirror length is found in the same simulation and summarized in Figure 4.3. Due to the phase matching condition of the mode gap resonator, the lasing mode exists at an offset when compared to the center of the band gap which necessitates the use of the coupled mode formalism to correctly estimate the reflectivity of the mirror at the lasing wavelength. If one assumes that the reflectivity of the mirrors is given by $R(\nu_L) = \tanh^2 \kappa L$, the external quality factor of the resonator can be overestimated by as much as a factor of ten (10), as illustrated in Figure 4.3.

The lasing frequency can be determined by requiring a phase retardation of some multiple of 2π per round trip for a frequency within the band gap of the grating,

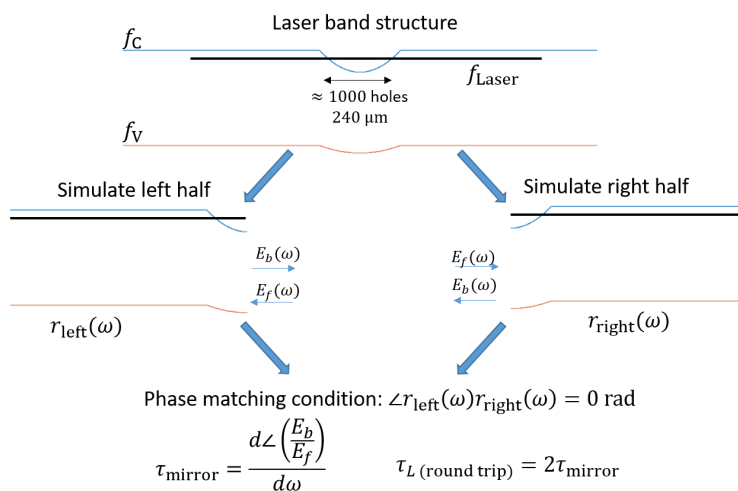


Figure 4.2: The simulation strategy to find the reflectivity as well as the round trip time inside the mode gap resonator, two necessary parameters that help understand the feedback properties of the resonator. In the top figure, the full donor mode resonator is shown with the conduction band in blue and the valence band in red. The location of the optical mode with respect to the band edges is shown in black.

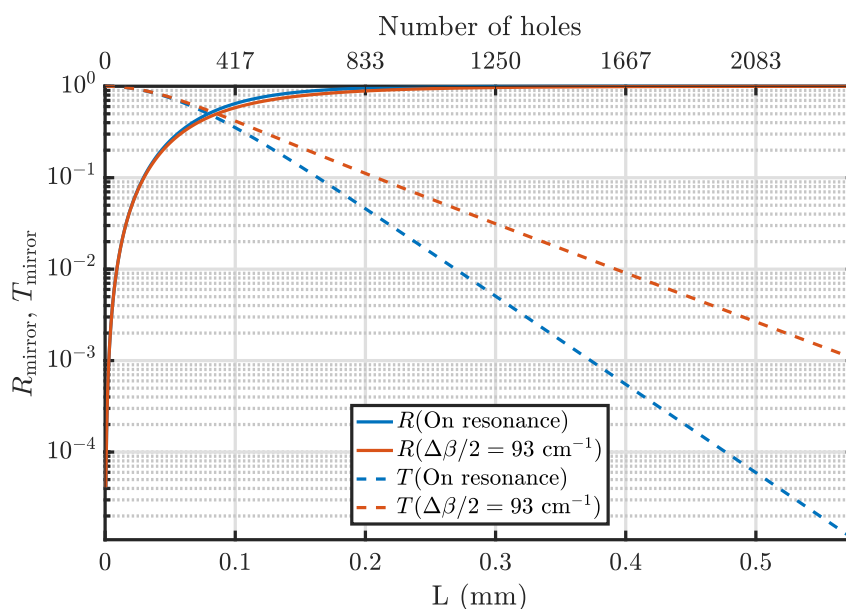


Figure 4.3: The reflection (R) and transmission (T) coefficient of the mirror portion of the resonator when the frequency is resonance with the mirror $\delta\beta = 0$ and when the frequency is offset by 93 cm^{-1} for a grating with $\kappa = 110 \text{ cm}^{-1}$.

taking into consideration the complex frequency dependent reflectivity of the two gratings. The quality factor of the high-Q resonance can be found by using the group delay (τ_{RT}) of the mode and the transmission (T) or reflection (R) evaluated at the resonance frequency (ν_0):

$$Q = 2\pi\nu_0 \cdot \tau_{RT} \cdot \frac{1}{-\ln R(\nu_0)} \approx 2\pi\nu_0\tau_{RT} \frac{1}{1 - R(\nu_0)} = 2\pi\nu_0\tau_{RT} \frac{1}{T(\nu_0)}, \quad (4.2)$$

For high-Q resonators, R approaches unity and it is therefore more convenient to describe the quality factor as a function of the transmission (or external loss).

Regimes of optical feedback

Now that we have established the tools necessary to analyze the passive resonator of the laser we are ready to analyze the properties of the laser in the presence of external optical reflections. Previous studies of optical feedback identify five (5) distinct regimes of optical feedback [77]. The first regime corresponds to small levels of optical feedback and gives rise to small changes in the lasing frequency while causing the linewidth of the laser to narrow or broaden depending on the phase of the optical reflector. In the second regime, two modes meet the phase matching condition and mode hopping is often observed. In the third regime, mode hopping is suppressed due to gain saturation and the laser oscillates in a single wavelength. This regime is found to occupy a small range of feedback power ratio and as such is often ignored. The fourth, and most detrimental regime occurs at moderate levels of optical feedback where multiple modes can lase simultaneously regardless of the phase of the optical reflector causing the linewidth to suddenly broaden dramatically. The fifth regime is that of an external cavity laser, where the system can be thought of as a large laser with a small gain section.

We will focus the discussion on the fourth regime known as the coherence collapse regime. In this regime, the location and the phase¹ of the reflector do not significantly affect onset of coherence collapse. For many lasers, the onset occurs quickly at relatively low feedback fractions near -40 dB [77]. One proposed strategy has been to increase the reflectivity of the quarter wave shift DFB grating by increasing the reflectivity of the mirrors in a quarter wave shift DFB laser (by increasing the product κL) [21]. Unfortunately, doing so often exacerbates any issues arising from spatial hole burning [78] and can decrease the absolute output power of the laser as it becomes increasingly under-coupled. As discussed in Section 2.3, if the quality

¹The phase of the reflection is determined in part by the location of the reflector to within a fraction of the wavelength.

factor of the resonator becomes limited by the intrinsic quality factor ($Q_{\text{ext}} > Q_i$), a rapid decrease in the output power is observed. It is therefore necessary to increase the *intrinsic quality factor* of the passive resonator before increasing the reflectivity of the external mirrors.

The feedback sensitivity of lasers is summarized by the feedback coefficient

$$C = \frac{\tau_{\text{ext}}}{\tau_{\text{RT}}} r_{\text{ext}} \frac{1 - |r_L|^2}{r_L} \sqrt{1 + \alpha^2}, \quad (4.3)$$

where τ_{ext} is the round trip time of the reflector, α is the linewidth enhancement factor [17], [79], r_{ext} is the reflectivity of the external reflector, and r_L is the complex reflectivity of the laser mirror at the output facet. As r_L approaches unity, as is the case for high-Q resonators, Equation 4.3 becomes

$$C = \frac{\tau_{\text{ext}}}{\tau_L} r_{\text{ext}} T_L \sqrt{1 + \alpha^2}, \quad (4.4)$$

where the $T_L = 1 - |r_L|^2$. In this form, it is clear that decreasing the transmission from the output facet has a crucial impact on the feedback coefficient of the laser. The phase matching condition for the case of weak feedback is given by

$$\Delta\phi_L(\nu) = 2\pi\tau_L(\nu - \nu_0) + r_{\text{ext}} \frac{1 - |r_L|}{r_L} \sqrt{1 + \alpha^2} \sin(2\pi\nu\tau_{\text{ext}} + \arctan \alpha), \quad (4.5)$$

where $\Delta\phi_L$ is the phase matching condition of the laser in the presence of optical feedback, ν is the frequency, and ν_0 is the lasing frequency in the absence of any optical feedback. A graphical representation of how the phase matching condition changes with increased feedback is shown in Figure 4.4. Near $C = 1$, the two modes satisfy the phase matching condition and will start to compete. For even larger values of C , the number of modes starts to increase giving rise to competition between multiple modes. One important distinction between the small feedback regime, and the regime of large feedback that causes coherence collapse is that the onset of coherence collapse is relatively independent of the location of the reflector. This is because in the case of coherence collapse with large τ_{ext} , a multitude of modes with a separation of $1/\tau_{\text{ext}}$ exists. The mode separated from the original lasing mode ν_0 by the relaxation resonance of laser will compete with the main lasing peak causing a dramatic increase in noise. As such, coherence collapse is typically characterized by measuring the relative intensity noise of the laser and observing a large increase near the relaxation resonance frequency.

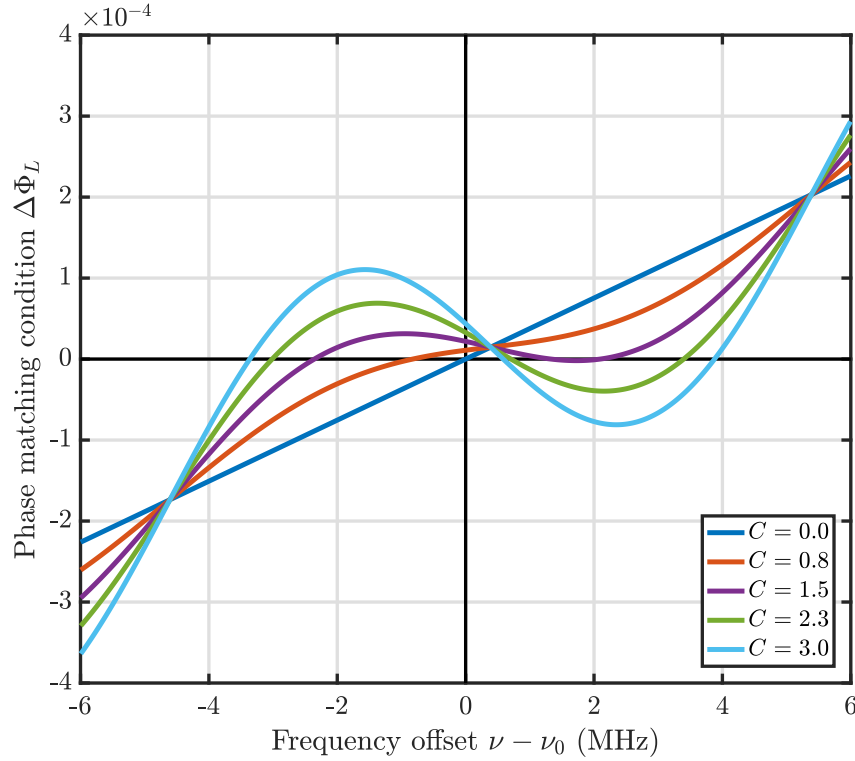


Figure 4.4: Phase matching condition as a function of the lasing frequency offset without feedback (ν_0) as C is increased. Plots are shown for $\alpha = 4$, $\tau_{\text{ext}} = 100$ ns, $Q_{\text{ext}} = 1 \times 10^5$.

4.2 Feedback sensitivity of high coherence Si/III-V lasers

In the previous section, we established how the feedback coefficient (C) is related to a variety of feedback parameters. Here we describe how the feedback sensitivity of the laser changes as a function of the thickness of the quantum noise control layer. We keep the laser structure of the QNCLs the same as we vary the QNCL thickness with the exception of the length of the end mirror section. This keeps τ_L constant as the thickness of the quantum noise control increases. In Section 2.3 we established that if the ratio between the external quality factor and internal quality factor is kept constant, the output power remains constant so long as the intrinsic quality factor is not limited by the losses in the high-Q material, silicon. The feedback coefficient can be expressed as a function of the external quality factor and the external reflector

$$C = \frac{\tau_{\text{ext}}}{\omega} r_{\text{ext}} \cdot \frac{Q_{\text{ext}}^{-1}}{r_L} \approx \frac{\tau_{\text{ext}}}{\omega} r_{\text{ext}} \cdot Q_{\text{ext}}^{-1}. \quad (4.6)$$

In the pursuit of high coherence lasers, we have shown that in the case of low-loss silicon $Q_{\text{Si}} \gg Q_{\text{III-V}}$ (in our case, $Q_{\text{Si}} > 1 \times 10^6$) we were led to the condition $|r_l| \approx 1$ which is the limit leading to Equation 4.6. But this is the condition for which most

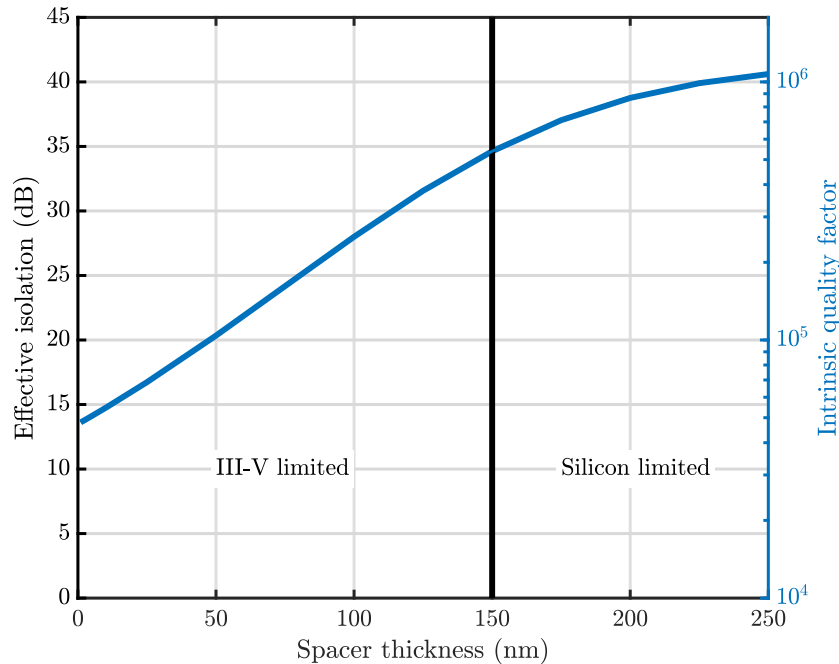


Figure 4.5: The effective increase in optical isolation (on the left axis) and intrinsic quality factor (right axis) of the laser as the thickness of the quantum noise control layer (spacer) is increased.

of the externally reflected field incident on a mirror r_l is reflected back from the laser resonator hence the feedback insensitivity is, to us unexpected, a side benefit of designing high-coherence hybrid Si/III-V semiconductor lasers. The effective isolation of a laser can therefore be compared to that of its all III-V counterpart through

$$\text{Effective isolation} = 20 \log \frac{Q_{\text{QNCL}}}{Q_{\text{III-V}}}. \quad (4.7)$$

Figure 4.5 summarizes the effective isolation and quality factor as a function of the thickness of the QNCL layer. A QNCL thickness of 150 nm is roughly equivalent to 35 dB or a single stage isolator. In applications where a single isolator is necessary, a QNCL with an SiO₂ thickness of approximately 150 nm can operate *without any isolator* obviating the need for the magneto-optic material in the photonic platform. Other heterogeneously integrated platforms can use the strategy outlined here to design even higher-Q cold cavities for lasers that will be even more insensitive to optical reflections **sin_lasers**, **sio2_lasers**

4.3 Measurement of the feedback sensitivity of QNCL lasers

We estimate the transition of the coherence collapse regime as the fraction of power reflected into the laser that causes the fringe visibility (β) of an interferometer with

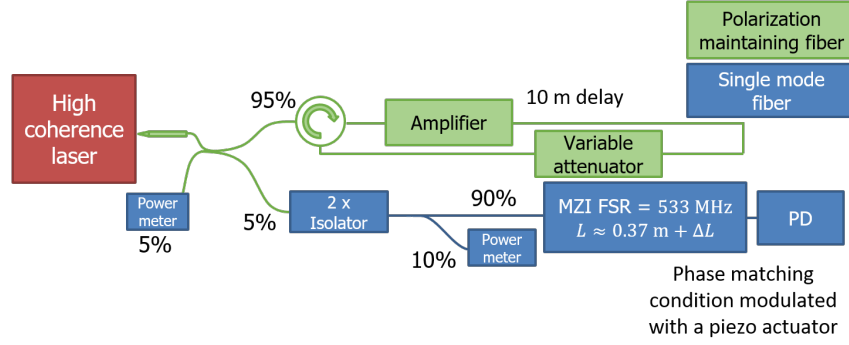


Figure 4.6: Experimental setup used to measure the onset of coherence collapse. Polarization maintaining fiber is used in the top path used to control the magnitude of the reflection is in polarization maintaining fiber to ensure that the reflection is in the same polarization as the lasing mode. A booster optical amplifier (BOA) is used to enable R_{ext} to approach unity while accounting for the losses in coupling to fiber and in various passive components. The fringe visibility of the MZI is characterized as the magnitude of the reflection is increased.

a free spectral range (FSR) of 533 MHz to be reduced to 70 % of its maximum value of 1. We define the fringe visibility of the interferometer as the ratio between the amplitude of the interference term as measured on a photodetector and the DC term as the path length mismatch of the interferometer is changed by a few wavelengths. It can be computed using:

$$\beta = \frac{V_{\text{max}} - V_{\text{min}}}{V_{\text{max}} + V_{\text{min}}}. \quad (4.8)$$

The experimental setup is shown in Figure 4.6. The output of the laser is divided into two separate paths, a feedback path in polarization maintaining fiber, and a characterization path. In the feedback path, a semiconductor amplifier (Thorlabs BOA1004P), followed by a variable attenuator are used to control the feedback fraction into the laser. Calibrated power taps are used to estimate the optical power in fiber, and the external reflectivity is estimated as $R_{\text{ext}} = P_{\text{reflected}}/P_{\text{forward}}$. The amplifier is necessary to overcome the finite coupling efficiency of light into single mode fiber (typically on the range of 20 – 40% for our lasers) as well as the finite insertion loss in the couplers and attenuator used (1 – 2 dB per component). As the reflectivity is increased, the onset of coherence collapse is determined by measuring the fringe visibility (β) of the voltage measured on the photodetector (V_{PD}) when the phase condition of the interferometer ($\frac{2\pi}{\lambda/n} \Delta L$) is changed

$$V_{\text{PD}}(\Delta L) = V_0 \left(1 + \beta \sin \left(\frac{2\pi}{\lambda/n} L + \frac{2\pi}{\lambda/n} \Delta L \right) \right), \quad (4.9)$$

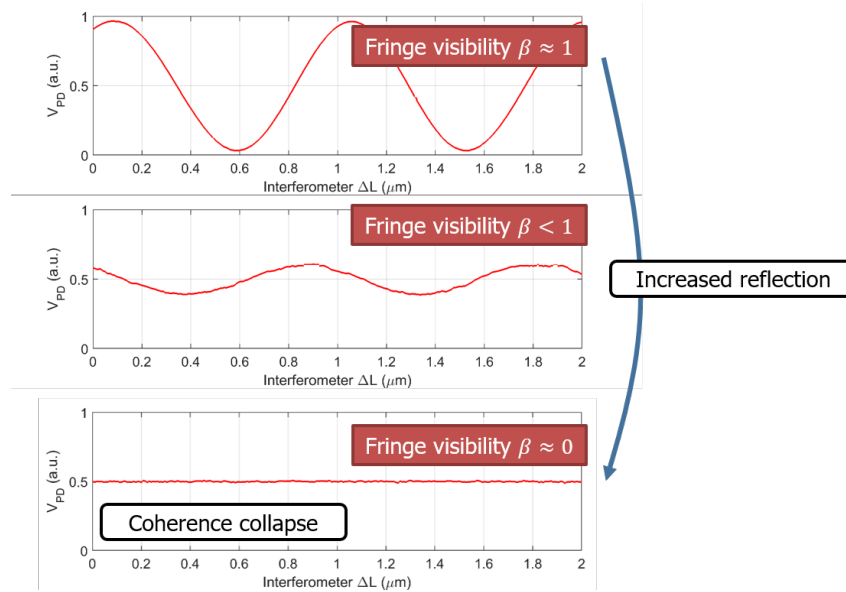


Figure 4.7: Progression of the fringe visibility from the MZI as the length of the interferometer is changed by a few micrometers. When the reflection is small, the fringe visibility (β) is close to 1. At the onset of coherence collapse, the fringe visibility starts to decrease until no fringes are seen.

where L is the nominal path length mismatch of the interferometer, n is the refractive index of fiber, c/nL is the free spectral range of the interferometer, λ is the wavelength of laser, and ΔL is the small change in path length of the Mach-Zehnder interferometer as the Piezo electric motor is actuated (typically on the order of a few micrometers). The interferometric length of the interferometer is varied by stretching one arm of the fiber by a few micro meters with a piezo electric actuator at a frequency of 1 kHz. The fringe visibility of the interferometer will drop rapidly once the linewidth of the laser becomes comparable or larger than the free spectral range of the interferometer. Figure 4.7 shows an example of the progression of the fringe visibility as the reflection is increased. In all measurements, the fringe visibility is measured 10 times for a given value of the external reflector.

Amplifier effect on the coherence collapse measurement

To confirm that the amplifier does not change the determination of the onset of coherence collapse, we compare how an DFB laser with one facet coated with a high reflectivity coating and the other coated with an anti-reflective (HR-AR) coating (part number Q-Photoncis QDFBLD-1550-5AX, ML9XX11 series DFB) is affected when the circulator, amplifier, and attenuator are replaced by a high-reflectivity gold mirror. Figure 4.8 shows the results of the two experiments showing good agreement

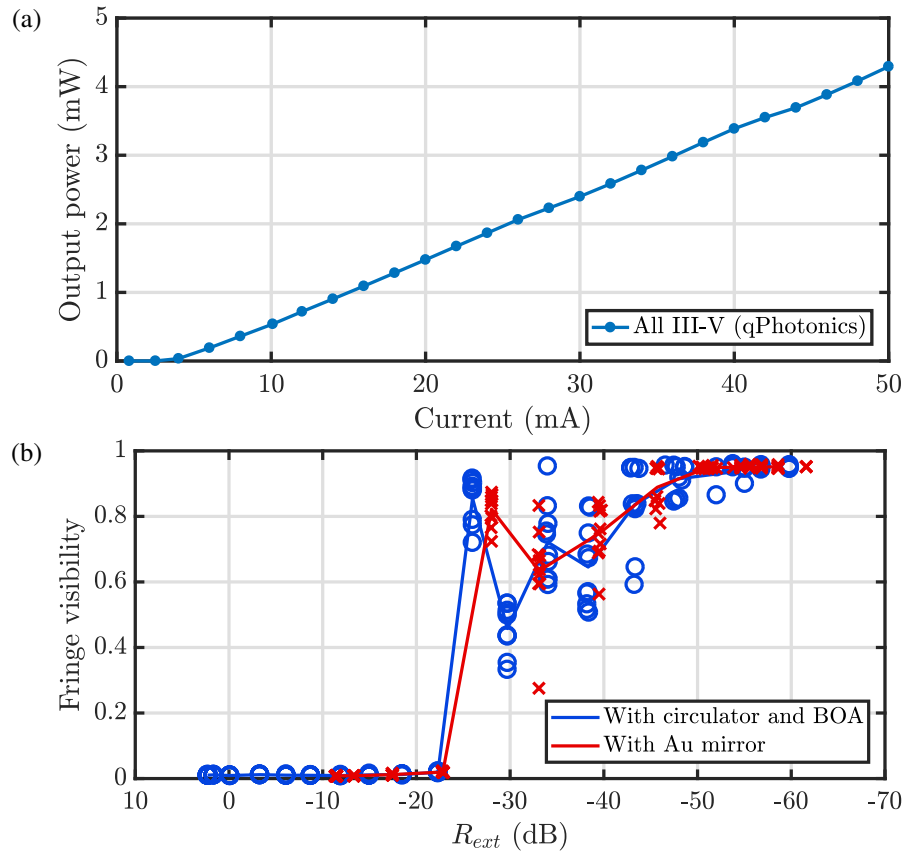


Figure 4.8: a) Light-current characteristics of the all III-V Q-Photonics QDFBLD-1550-5AX laser used in the coherence collapse experiments. b) Coherence collapse of a commercially available laser when measured with a polarization maintaining fiber mirror and when measured with a circulator and amplifier when operated at 30 mA ($I_{th} = 5$ mA). In both cases, the onset of coherence collapse occurs near 50 dB, indicating that the presence of an amplifier does not affect the measurement o the onset of coherence.

between the experiment with and without an amplifier. A coupling efficiency of 50 % was assumed for the commercially available laser. With an amplifier, the maximum reflectivity is increased from -10 dB to above 0 dB. While reflectivity greater than 0 dB indicates lasing in the external cavity, the ability to reach near unity reflectivity is important for measuring the onset of coherence collapse for QNCL lasers.

Coherence collapse measurements for QNCL lasers

Figure 4.9 compares the fringe visibility for three lasers, a commercial off-the shelf HR-AR coated DFB laser, a 50 nm QNCL, and a 90 nm QNCL laser at a bias current 200 mA ($\approx 2.5 \times I_{threshold}$). Figure 4.9a shows the luminosity as a function of current

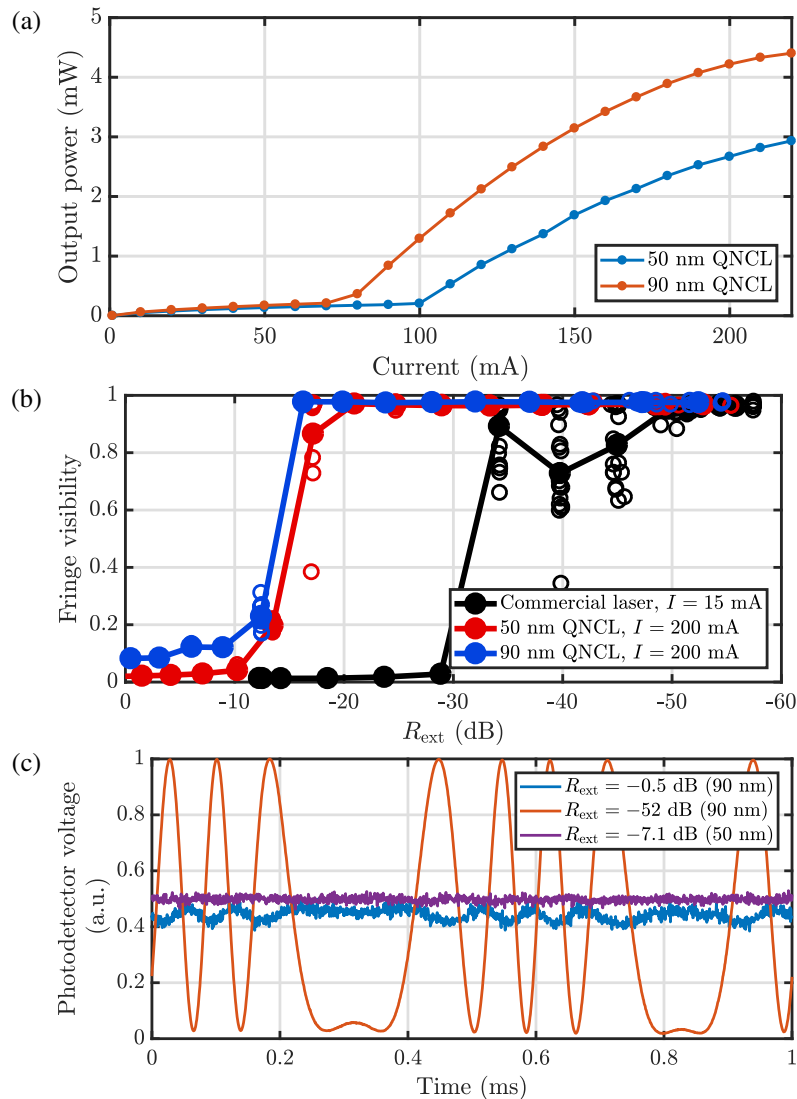


Figure 4.9: a) Light-current characteristics of the two QNCLs tested for their feedback sensitivity. b) Fringe visibility measurement for the two QNCL lasers as well as the commercial III-V DFB. c) Raw data obtained from the fringe visibility experiment of the QNCLs. Fringes remain visible for the 90 nm QNCL even in the coherence collapse regime.

for the two silicon/III-V lasers tested with QNCL thickness of 50 nm and 90 nm. In these experiments, the optical path length of the reflector was 10 m in fiber. The 50 nm QNCL maintains its high coherence properties up to an external reflectivity of -20 dB while the 90 nm QNCL maintains a fringe visibility near unity up to a reflectivity of -15 dB.

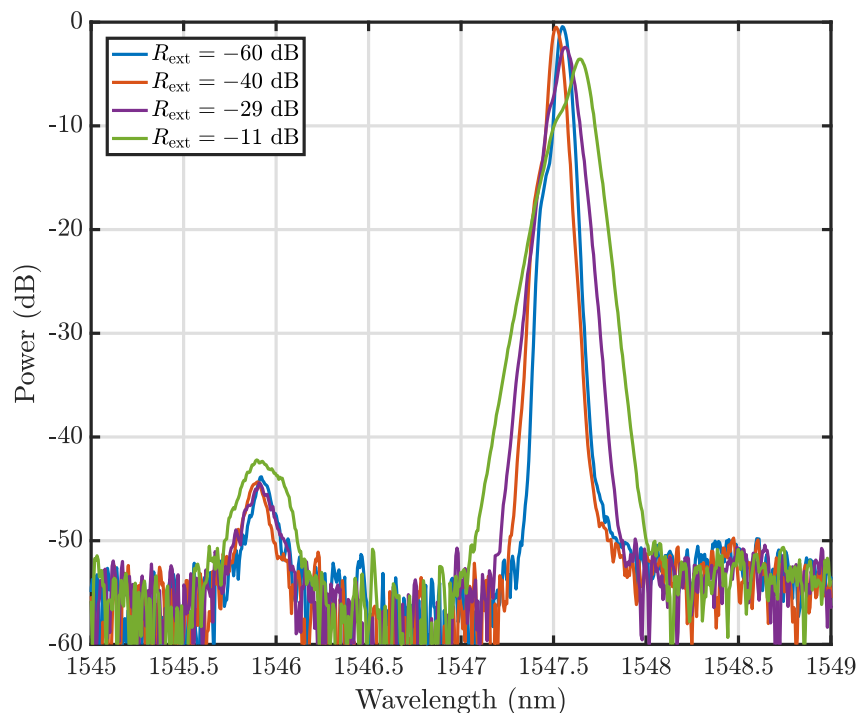


Figure 4.10: OSA spectra of the commercial HR/AR coated DFB taken with a resolution bandwidth of approximately 0.08 nm. A slight broadening of the 30 dB bandwidth starts to broaden for $R_{\text{ext}} > -40$ dB. At higher levels, $R_{\text{ext}} > -28$ dB, the 10 dB bandwidth of the spectrum begins to broaden.

Optical spectrum of QNCL lasers with external reflections

The optical intensity spectrum of a laser, as measured with an optical spectrum analyzer, can broaden in the presence of optical feedback. This has been previously used to characterize the onset of coherence collapse for semiconductor lasers. Figure 4.10 shows the optical spectrum of the HR/AR DFB laser as the reflectivity of the external reflector is varied and the laser transitions from the coherent regime into the coherence collapse regime (HP71450), using a resolution bandwidth of approximately 0.08 nm (≈ 10 GHz at 1550 nm). For an external reflectivity of -40 dB, the 30 dB bandwidth begins to broaden. Once an external reflectivity of approximately -28 dB is reached, it becomes clear that the spectrum is wider than in the case of no external reflector. If this metric is used to determine the transition of the coherence collapse regime, the 90 nm QNCL would *never reach coherence collapse* as shown in Figure 4.11. The optical spectrum of the 90 nm QNCL lasers is not observed to broaden on a scale measurable by typical spectrum analyzers. Similarly, the 50 nm QNCL does not experience any noticeable broadening in the measured spectrum on the OSA even when the external reflectivity approaches unity.

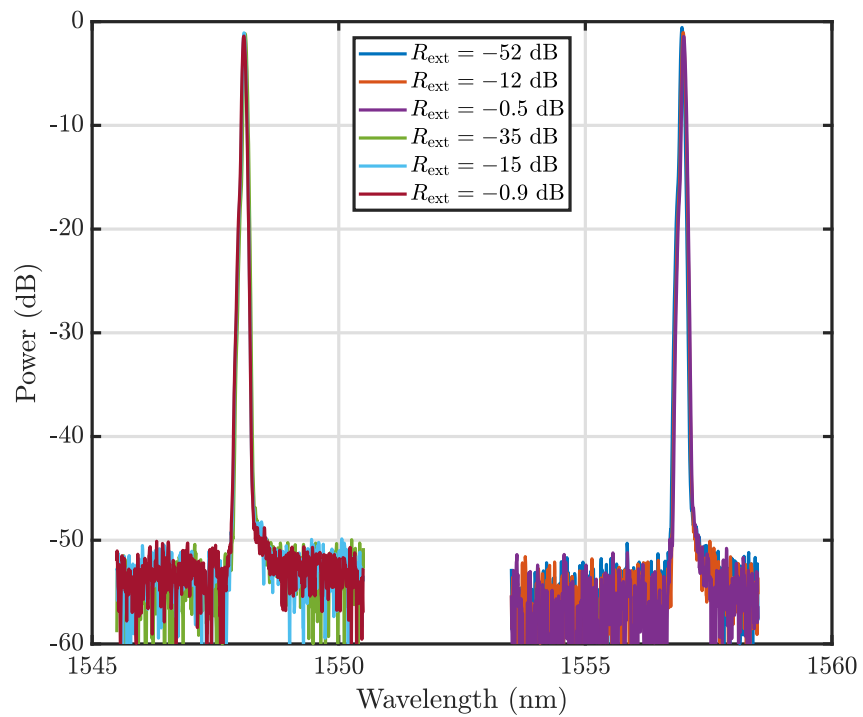


Figure 4.11: OSA spectra of the 90 nm QNCL laser under various levels of optical feedback. We observe that the optical spectrum remains virtually identical even for optical feedback levels approaching 0 dB.

Relative intensity noise of QNCL lasers with optical feedback

To explain why the transition of the coherence collapse regime is not observable on the OSA, we measure the relative intensity noise of the lasers on a high speed electrical spectrum analyzer. The setup is identical to the one shown in Figure 4.6 with the exception that the MZI, which is not needed in intensity measurements, is removed and replaced with a high speed photodetector (Optilab BPR-20-M, 18 GHz 3 dB bandwidth) and a radio frequency spectrum analyzer (HP8560E, 50 GHz bandwidth). The electrical spectrum is measured as a function of R_{ext} and summarized in Figure 4.12 for the case of the HR/AR coated DFB laser. The RF spectrum of the high coherence lasers 50 nm and 90 nm QNCL under different levels of optical feedback is shown in Figure 4.13 and Figure 4.14 respectively. From the three figures, one observes that the onset of coherence collapse is also heralded by the appearance of a peak in the intensity spectrum and that the peak is centered on the relaxation resonance frequency as measured by the intensity modulation response (black curve). An important consequence of the reduced relaxation resonance frequency of the QNCL Si/III-V lasers is that the RF noise spectra limits the bandwidth of the relative intensity noise induced by optical feedback to frequencies below the relaxation resonance frequency, approximately equal to 500 MHz for the 90 nm QNCL. This means that for the 90 nm QNCL laser, the linewidth of the laser, even in the coherence collapse regime, will not greatly exceed a few multiples of 533 MHz. Using this insight, it is clear why the OSA cannot resolve the increased noise in the optical spectrum of QNCL lasers. Furthermore, the limited bandwidth of the noise explains why the fringe visibility of an MZI in the case of the 90 nm QNCL did not reach a value of 0 in the coherence collapse regime. The fringe visibility (β), is related to the free spectral range (FSR) and the linewidth of the laser by ($\delta\nu$) by

$$\beta = e^{-\delta\nu/\text{FSR}}. \quad (4.10)$$

In the case of the 90 nm QNCL the fringe visibility decreases to approximately 0.08 for the case of a large external reflector, giving the laser an approximate linewidth of 1.3 GHz, consistent with the bandwidth of the relative intensity noise measured in Figure 4.14c.

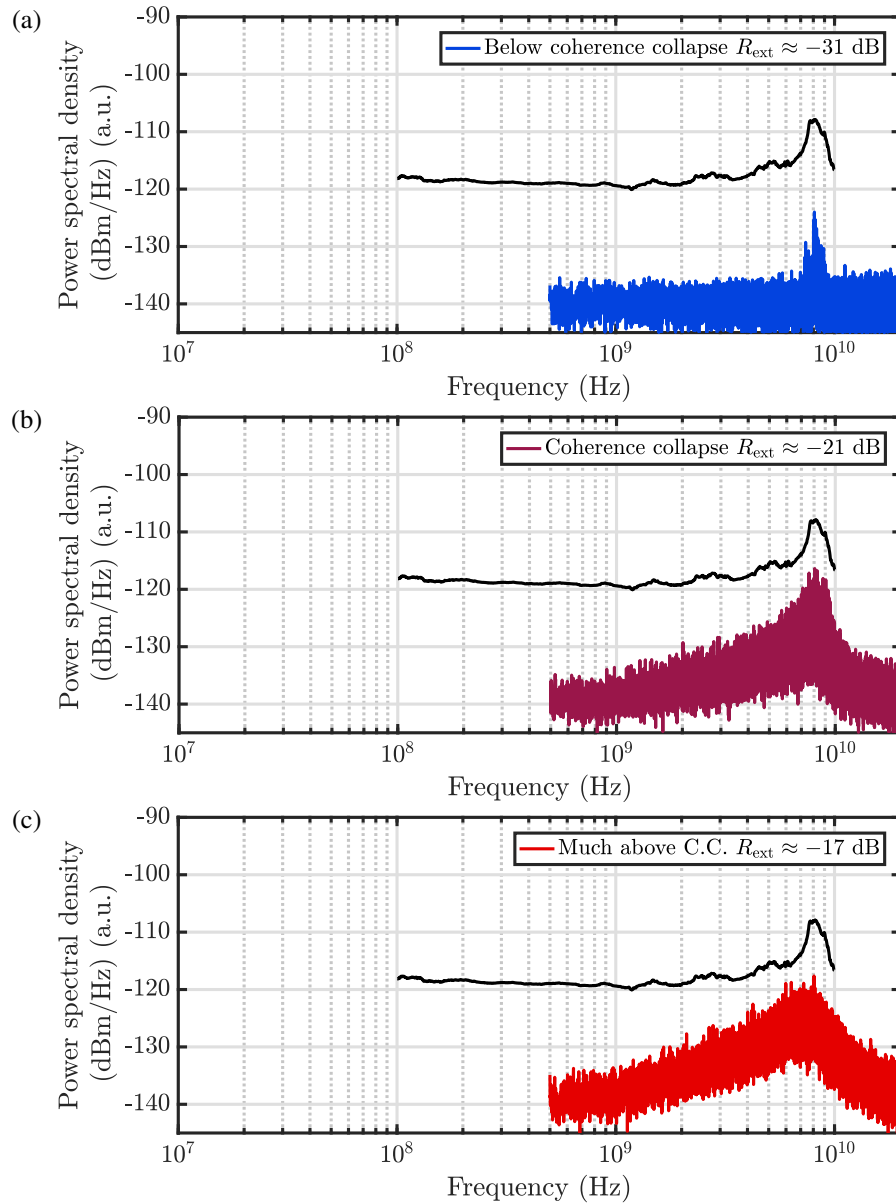


Figure 4.12: Relative intensity noise a commercial laser as the external reflectivity R_{ext} is varied when the laser is biased at 20 mA. The black line shows the shape of the intensity modulation response of the laser as a visual guide. We note that the first sign of coherence collapse occurs at the relaxation resonance frequency.

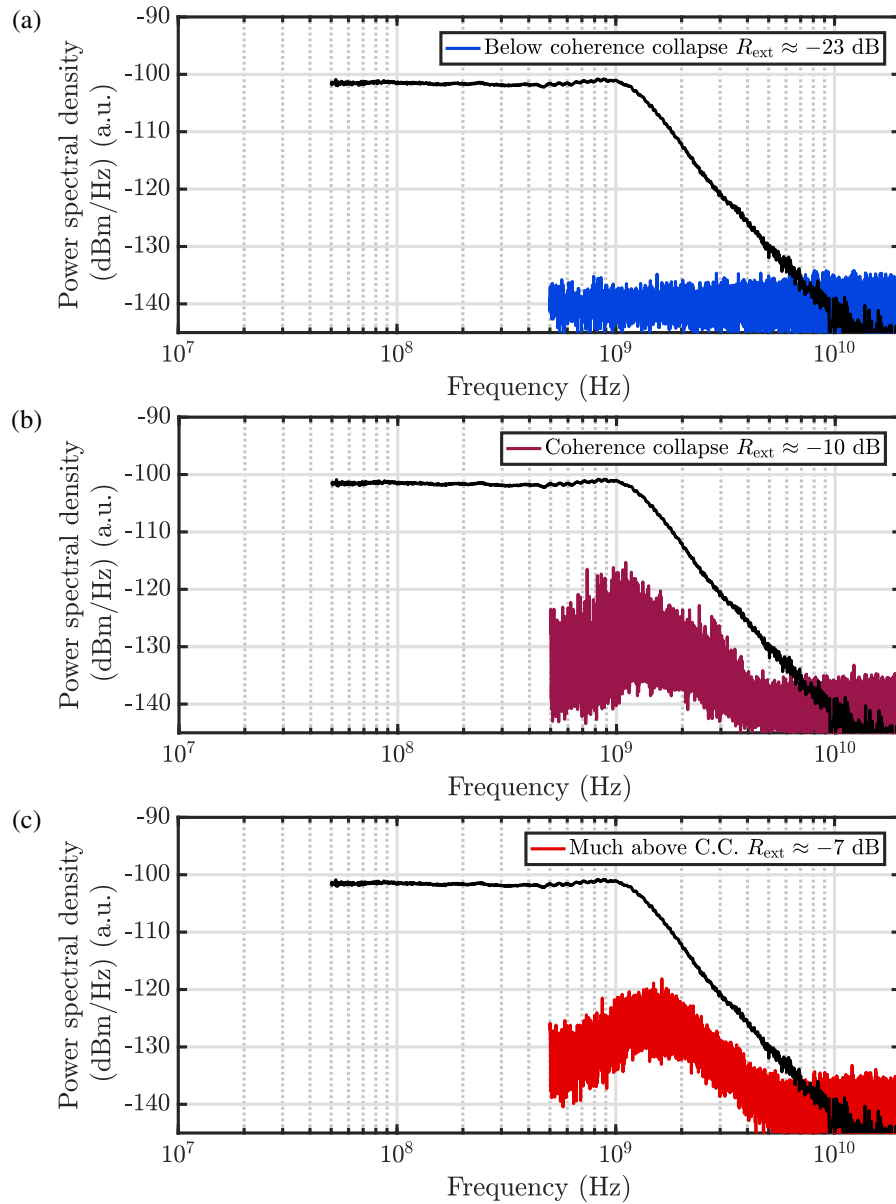


Figure 4.13: Relative intensity noise of 50nm QNCL laser as the strength of the external reflector is varied. The black line shows the measured intensity modulation response of the laser as a visual guide. The onset of coherence collapse first appears near the relaxation resonance frequency.

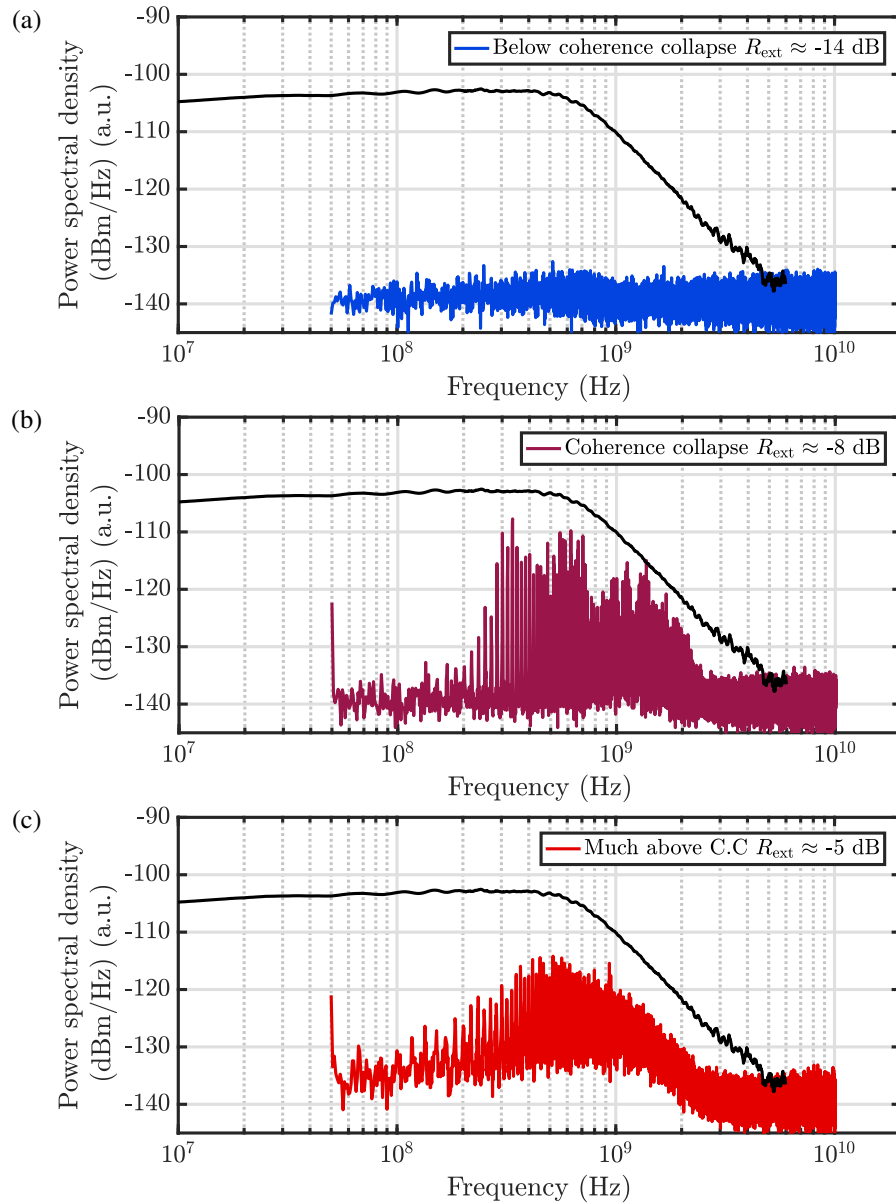


Figure 4.14: Relative intensity noise of 90nm QNCL laser as the strength of the external reflector is varied. The black line shows the measured intensity modulation response of the a similar laser as a visual guide. The onset of coherence collapse first appears near the relaxation resonance frequency.

4.4 Conclusions

To conclude, we investigated the transition of the coherence collapse regime for high-coherence lasers. We found that in high-coherence QNCL lasers the onset of coherence collapse as measured through both a fringe visibility measurement and through measuring the relative intensity noise occurs at 20 dB higher reflection levels compared to their conventional all III-V counterparts. We attribute the increase of the onset of coherence collapse to the larger external quality factor of the laser's cold cavity. Using modal engineering and quantum noise control, the quality factor of QNCL lasers can be increased to approach that of the low loss silicon cavity ($Q \sim 10 \times 10^6$). By taking advantage of the low intrinsic losses in the silicon layer, the external quality factor can be increased by utilizing higher reflectivity mirrors without sacrificing optical power. The low optical transmission through the mirror decreases the change in the reflectivity of the output mirror, keeping the laser stable in the presence of uncontrollable external reflectors.

The QNCL design explored in this chapter paves the path for the design of single mode lasers that can function without the need for optical isolators. Optical isolators necessitate the use of magneto-optic materials and thus increase the cost of optical systems that include them. These lasers take advantage of the high-Q silicon cavity obviating the need for isolators. It is envisioned that future advances in material growth and fabrication techniques could allow the quality factor of low loss semiconductor resonator to increase beyond the demonstrated value of 1×10^6 to further decrease the sensitivity to optical feedback of semiconductor lasers. Since the incorporation of magnetic isolators is not compatible with CMOS manufacturing used to fabricate hybrid Si/III-V lasers, the prospect of optical circuitry free of isolators has an immense economic value.

Part II

3D imaging with swept frequency semiconductor lasers

SWEPT SOURCE SEMICONDUCTOR LASERS FOR 3D IMAGING

Swept source 3D imaging has become an important tool for many scientific and industrial applications due to its high dynamic range, and high axial resolution [80]. Applications include LIDAR (light detection and ranging) [81], high-accuracy optical profilometry [28], fingerprint detection [29], and many *in vivo* biomedical diagnostic applications [30]–[33].

Swept source optical coherence tomography (SSOCT), first proposed in [23], utilizes the large optical bandwidth of swept frequency lasers, up to 10s of THz, to acquire detailed 3D images in a reflection configuration. One advantage of SSOCT compared to other embodiments of OCT [82] is the ability to measure the location of scatterers along the axial dimension without the need for any moving parts. 3D imaging systems based on SSOCT typically employ beam steering to acquire volumetric 3D imaging characterizing each lateral location in isolation.

In this section, we will review the basics of swept frequency reflectometry and detail the optical sources that are used in the experiments outlined in Chapters 6 and 7 to obtain high axial resolution 3D images using full field illumination and swept frequency lasers without any moving parts.

5.1 Swept frequency reflectometry

Swept frequency reflectometry, also known as chirped radar [83], [84], frequency modulated continuous wave LIDAR [81], or swept source optical coherence tomography (SSOCT), uses a laser, with continuous output power but changing carrier frequency, to measure the distance between a target and a mirror at a known location in a reflection geometry. One implementation of such a ranging system using a laser is shown in Figure 5.1.

The imaging system is composed of a swept frequency laser [13], a photodetector and a Michelson interferometer where one arm is formed by the reflections of the sample we wish to quantify. All optical fiber is assumed to be single mode and polarization maintaining to ensure mode-matching between the reference wave from the mirror and reflected wave from the targets we wish to quantify. The complex

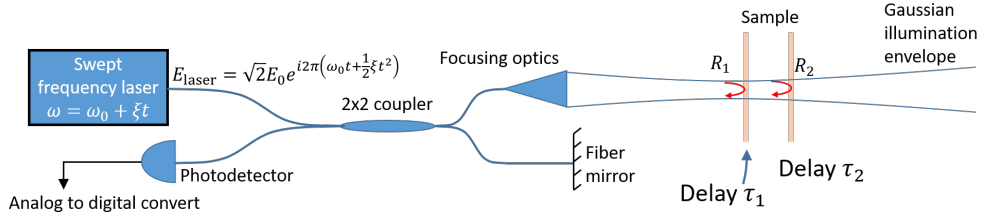


Figure 5.1: A typical swept frequency reflectometry setup using a linearly swept frequency laser. The key elements include a 50:50 coupler, and a high speed photodetector as well as electronics used for computation and control. Focusing optics are used to ensure adequate illumination and collection into single mode fiber from a target at distance τ_j from the reference mirror, located within a given depth of field of the optical elements.

optical field (E_{laser}) of the swept frequency laser can be written as:

$$E_{\text{laser}} = \sqrt{2}E_0 e^{i2\pi(\omega_0 t + \frac{1}{2}\xi t^2)}, \text{ for } t \in [-T/2, T/2], \quad (5.1)$$

where $\sqrt{2}E_0$ is the complex amplitude of the electrical field, ω_0 is the optical frequency at $t = 0$ in Hz, and ξ is the chirp rate in Hz/s. While not necessary for swept source optical coherence tomography [85], a linear chirp simplifies the mathematical discussion, data analysis, and can simplify the hardware implementation. In our experiments, the assumption that the chirp rate ξ is constant is enforced through the use of a feedback system [86] outlined in Section 5.5. The bandwidth of the chirp, B , given by $B = T\xi$, determines the axial resolution of the ranging system ($\Delta z = c/2B$ where c is the speed of light).

At the detector, the field from the reflectors j is delayed compared to the field received from the mirror by a time τ_j determined by the optical path length difference (d_j) between the mirror and the reflectors. The optical delay is given by $\tau_j = 2d_j n_{\text{bulk}}/c$, where n_{bulk} is the bulk refractive index where the reflector resides. For the duration of the chirp ($t \in [-T/2, T/2]$), the electric field at the photodetector can be written as:

$$E_{\text{PD}}(t) = \frac{1}{\sqrt{2}} \left(E_{\text{mirror}}(t) + \sum_j E_j(t) \right) \quad (5.2)$$

$$= \frac{1}{\sqrt{2}} \left(E_0 e^{i2\pi(\omega_0 t + \frac{1}{2}\xi t^2)} + \sum_j r_j E_0 e^{i2\pi(\omega_0(t-\tau_j) + \frac{1}{2}\xi(t-\tau_j)^2)} \right). \quad (5.3)$$

The photocurrent is proportional to the magnitude squared of the electric field at the

detector $E_{\text{PD}}E_{\text{PD}}^*$ and can be expressed as

$$I_{\text{PD}}(t) = \frac{1}{2} \left(I_0 + I_0 \sum_j R_j + \sum_j 2\sqrt{R_j I_0^2} \cos(2\pi\omega_0\tau_j + 2\pi\xi\tau_j t) \right),$$

for $t \in [-T/2, T/2]$, (5.4)

where the beat terms involving two reflectors in the target arm of the interferometer have been ignored. This assumption holds for the case of weak reflectors ($R_j \ll 1$) where shot noise from the reference mirror may overcome the weak signal from the two reflectors. In general, one can control the fraction of power received from the mirror (I_m) and the amount of power launched onto the target (I_t). In this case, Equation 5.4 can be written as

$$I_{\text{PD}}(t) = I_m + \sum_j R_j I_t + \sum_j 2\sqrt{R_j I_t I_m} \cos(2\pi\omega_0\tau_j + 2\pi\xi\tau_j t),$$

for $t \in [-T/2, T/2]$. (5.5)

Choosing $I_m \gg \sum_j R_j I_t$ ensures that the beat term is large enough to overcome the shot noise due to dark current of the photodetector, allowing the signal to noise ratio to approach the shot-noise limited regime. The power launched onto the target is limited by safety considerations [87] and cannot be arbitrarily increased, even if the use of amplifiers make it possible. In our discussion, we will assume that the optical delay between the mirror and the reflector is much smaller than the coherence time of the laser. In the in this case, the effect of the finite coherence length of the laser can be ignored. For reflectors near or beyond the coherence length of the laser, amplitude of the beating term rapidly decreases [6], [88].

The finite duration of the chirp can be modeled mathematically by a rect function in the time domain

$$I_{\text{PD}}(t) = \left[I_m + \sum_j R_j I_t + \sum_j 2\sqrt{R_j I_t I_m} \cos(2\pi(\omega_0\tau_j + \xi\tau_j t)) \right] \cdot \text{rect}\left(\frac{t}{T}\right), \quad (5.6)$$

where

$$\text{rect}(t) = \begin{cases} 1 & \text{for } |t| < \frac{1}{2} \\ 0 & \text{for } |t| > \frac{1}{2} \\ 0.5 & \text{for } |t| = \frac{1}{2}. \end{cases} \quad (5.7)$$

The linearity of the chirp ensures that the difference in the optical frequency between the reference and received wave is constant for the duration of the chirp, as shown in

Figure 5.2. The optical delay of the reflector τ_j with respect to the reference mirror is thus proportional to the beat frequency $\xi\tau_j$ of the photodetector. Identifying the precise delay of the reflector can be accomplished by finding the peak of the Fourier transform of the photocurrent.

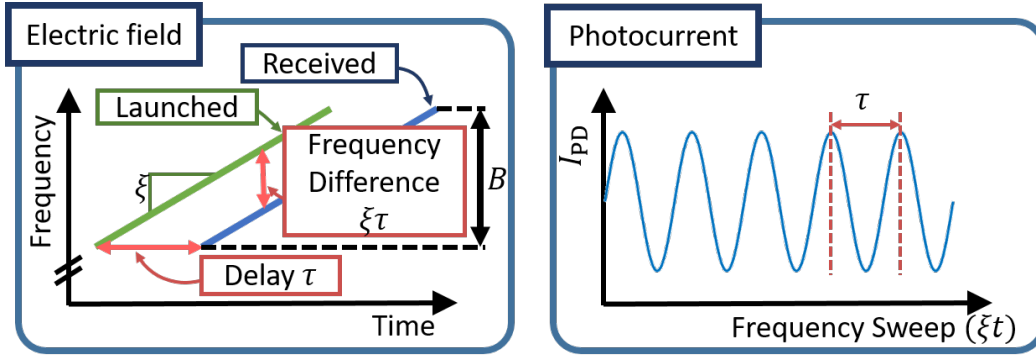


Figure 5.2: Cartoon of the received optical frequency as a function of time from the reference mirror and the target located at an optical delay τ . For a linear chirp, the generated photocurrent is a sinusoid that oscillates at a constant frequency $\xi\tau t$.

The depth of field (δz) and the lateral resolution (δx) of OCT systems are limited by the numerical aperture (NA) imaging optics and related by [89]:

$$\delta z = \frac{\lambda}{2(\text{NA})^2} \quad \delta x = 0.82 \frac{\lambda}{\text{NA}}. \quad (5.8)$$

For conventional imaging systems, δz is typically considered to be the axial resolution. Swept source optical coherence tomography (SSOCT) is able to discern the location of reflections *within* the depth of field (δz). As the lateral resolution is improved, the depth of field decreases imposing a trade off that needs to be considered in the design of imaging systems.

Axial point spread function of swept-frequency ranging systems

Taking the Fourier transform¹ of the received photo-current in Equation 5.6 gives:

$$\begin{aligned} \tilde{I}_{\text{PD}}(\nu) = & \left[\left(I_m + \sum_j R_j I_t \right) \delta(\nu) + \right. \\ & \left. \sum_j \sqrt{R_j I_t I_m} \left(e^{j2\pi\omega_0\tau_j} \delta(\nu - \xi\tau_j) + e^{-j2\pi\omega_0\tau_j} \delta(\nu + \xi\tau_j) \right) \right] * \frac{T}{2} \text{sinc}\left(\frac{\pi\nu T}{2}\right), \quad (5.9) \end{aligned}$$

¹We define the Fourier transform of a deterministic signal $\mathcal{F}[x(t)] = \tilde{x}(\nu) = \int_{-\infty}^{\infty} x(t)e^{-i2\pi\nu t} dt$. Using this definition, the convolution theorem is given by $\mathcal{F}[x(t) \cdot y(t)] = (\tilde{x} * \tilde{y})(\nu)$.

where ν denotes the beat frequency in Hz, $*$ denotes the convolution operator, and

$$\text{sinc}(\nu) = \begin{cases} \frac{\sin \nu}{\nu} & \text{for } \nu \neq 0 \\ 1 & \text{for } \nu = 0. \end{cases} \quad (5.10)$$

Recasting Equation 5.9 in terms of the bandwidth of the chirp (B) and the location of the reflector (τ_j) and the optical delay ($\tau = \nu/\xi$)

$$\begin{aligned} \tilde{I}_{\text{PD}}(\tau) = \frac{B}{2\xi^2} & \left[\left(I_m + \sum_j R_j I_t \right) \delta(\tau) + \right. \\ & \left. \sum_j \sqrt{R_j I_t I_m} \left(e^{j2\pi\omega_0\tau_j} \delta(\tau - \tau_j) + e^{-j2\pi\omega_0\tau_j} \delta(\tau + \xi\tau_j) \right) \right] * \text{sinc}\left(\frac{\pi\tau B}{2}\right). \end{aligned} \quad (5.11)$$

In this form, it is clear that the Fourier transform of the photocurrent is a map of the location of the reflectors, known as an A-scan, where τ corresponds to the position of the reflector, and the magnitude of the Fourier transform is the product of the strength of the received signal and the reference signal. Ideally, each reflector would appear as a delta function with infinitesimally small width in the optical delay domain. Due to the finite bandwidth of the chirp (B), each reflector appears as having a width of approximately $\delta\tau = 1/B$, referred to as the axial resolution of the ranging system. Often, a window function is applied to the received photocurrent prior to taking the Fourier transform to improve the dynamic range of the point spread function (PSF), albeit at a small expense of the resolution; in this case no window was applied resulting in a sinc PSF [90]. Ranging systems employ beam scanning, typically through the use of galvanometric scanners [28], to acquire individual axial scans at different lateral locations to form a volumetric 3D scan.

Three dimensional imaging and profilometry

The general 3D imaging problem involves finding all the reflectors in a given volume. An important metric for these systems is the minimum separation between two independent depth slices known as the resolution. The axial resolution is given by the optical bandwidth of the chirp and cannot be improved by increasing the signal to noise ratio. Figures 5.3 and 5.4 show the beat acquired signal in the time domain for two closely spaced reflectors when imaged with swept lasers with different optical bandwidths. A chirp with a larger bandwidth allows the system to unambiguously distinguish two closely spaced reflectors. This is especially important for many biological applications where one is interested in quantifying the shape of arbitrary biological tissue [91].

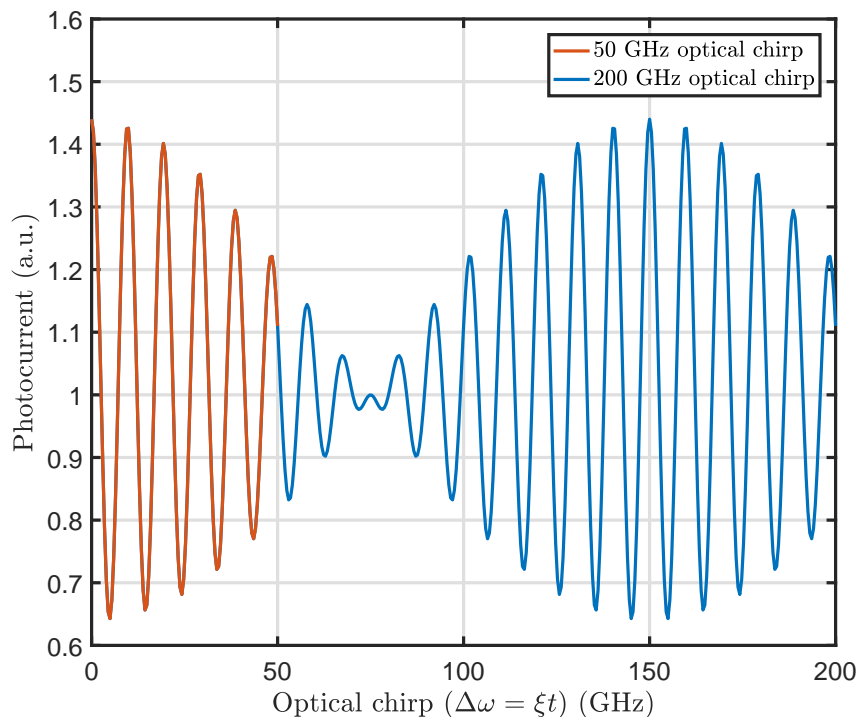


Figure 5.3: The photocurrent received in a simulated experiment with two reflectors located at optical delays of 0.1 ns and 0.107 ns corresponding to physical locations of 15 mm and 16 mm. Once acquired utilizing an optical chirp of 50 GHz in red and 200 GHz in blue.

On the other hand, many real world objects are opaque and thus appear as a single reflector to imaging systems. In this case, the acquisition system need not consider the case where multiple reflectors exists along the illumination axis. The metric of interests changes and defines a different problem, namely profilometry. In this case, one is interested in precisely determining the location of a *single* reflector. The precision of the measurement along the illumination axis becomes dependent on the signal to noise ratio and limited not by the bandwidth of the chirp. Profilometers are limited by their ability to precisely estimate the single beat frequency often determined by the accuracy of the sampling rate of the analog to digital converter [92], [93].

5.2 Optical sources for swept frequency reflectometry

Vertical cavity surface emitting lasers (VCSELs) and distributed feedback lasers (DFBs) have both been shown to be good sources for swept-frequency ranging [13], [86]. Their wide availability, low cost, and rapid repetition rates ($T \approx 1$ ms), compared to mechanically tuned external cavity lasers, make them ideal for 3D

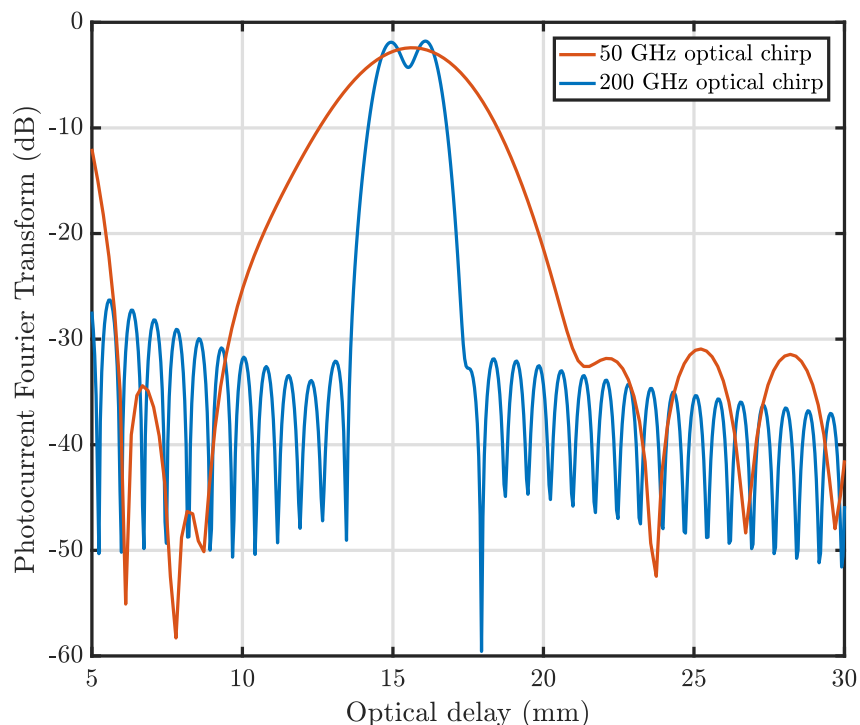


Figure 5.4: Fourier transform of the signal measured in Figure 5.3 after a Hamming window is applied. In the case of the 50 GHz sweep (3 mm resolution), the two reflectors are not resolved, while in the case of the 200 GHz chirp (0.75 mm resolution) two reflectors are resolved.

ranging. Both DFBs and VCSELs can be tuned through the injection current, which in turn heats the optical cavity and changes the refractive index of the laser through the thermo-optic coefficient [94]. Using the thermo optic effect, VCSELs and DFBs can change their lasing frequency by a few hundred GHz.

More recently, MEMS VCSELs [95], [96] have been demonstrated with optical chirp repetition rates between $T \approx 1$ and $10 \mu\text{s}$ limited by the mass and stiffness of the MEMS mirror. Rather than changing the temperature of the laser, MEMS VCSELs are tuned by applying a voltage to a floating membrane that changes the physical length of the cavity. The lasing frequency can change by up to 25 THz, corresponding to an axial resolution of $\approx 6 \mu\text{m}$ in vacuum. The main drawback of MEMS VCSELs is their large cost and decreased coherence length compared to other VCSELs.

While the 3D imaging demonstrations in the following chapters utilize DFB and VCSELs, the techniques developed are compatible with MEMS VCSELs enabling the systems to greatly improve their axial resolution should MEMS VCSELs be

used.

5.3 Reference mirror location

The choice of the location of the reference mirror plays an important role in the design of OCT systems. The reference mirror can be placed so as to minimize the path length difference between the mirror and the targets, decreasing any effects of the finite coherence length of the swept source. It must also be chosen as to ensure that the beat frequency beat frequency originating from the furthest expected reflector ($\xi\tau_{\max}$) is smaller than the bandwidth of the photodetector. Two other important considerations must be taken when designing the interferometric system:

1. Reflectors at $\pm\tau_j$ appear at the same location in the Fourier transform of the acquired signal. It is therefore beneficial to place the closest reflector away from $|\tau_j| = 0$ so as to remove this ambiguity.
2. Unwanted reflections, stemming from imperfect connections in fiber or imperfect coating in bulk optical elements, will typically appear at predetermined locations once the system is assembled. The location of the reference mirror must be chosen as not to confound the targets with these imperfections.

5.4 The linearly swept frequency laser

During the previous discussion, we have assumed that the laser had both a perfectly linear sweep, $\omega(t) = \omega_0 + \xi t$, and constant output power. While this is not often the case, we have developed electronic systems around VCSELs and DFB lasers, that enforce these two assumption through the use of electronic feedback [86], depicted in Figure 5.5. Fluctuations in the output power are suppressed through a feedback loop that adjusts the gain (or loss) of an amplifier (or attenuator) as the injection current to the laser is changed during the chirp.

An independent feedback loop enforces the linearity of the chirp by comparing the beat signal from a reference Mach-Zehnder interferometer (MZI) to that of an electronically generated sinusoidal tone. A perfectly linear chirp yields a signal at the photodetector oscillating at a constant frequency ($\xi\tau_{\text{MZI}}$), where τ_{MZI} is the optical path length mismatch between the two arms of the MZI. Before any feedback is enabled, a good estimate, called the predistortion, of the current that yields a nearly linear chirp is applied to the laser. This initial estimate can, in certain cases, provide enough linearity, such as for the suppression of stimulated Brillouin scattering [27]. For swept source optical coherence tomography, the linearity of the chirp determines

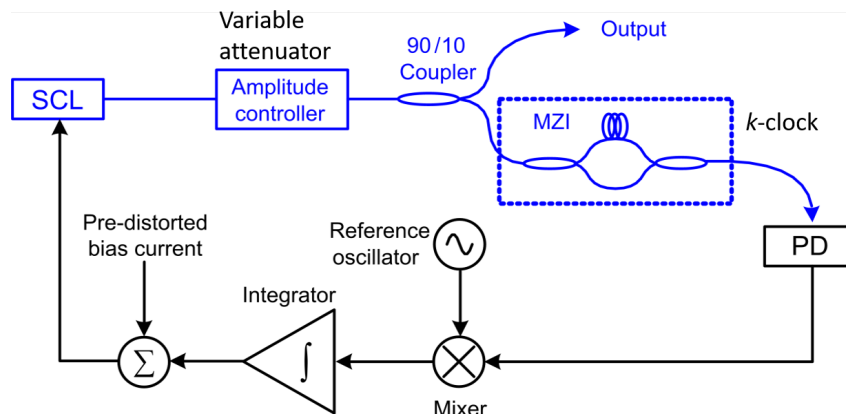


Figure 5.5: The electro-optic system used to linearize the semiconductor laser (SCL) adapted from [86]. The amplitude controller can be either a variable attenuator or a semiconductor optical amplifier.

the point spread function of the ranging system in the depth dimension, and therefore a precisely linear chirp is preferable. Once the estimate is found, the signal to from the MZI is compared to the RF reference in real time and deviations from a linear chirp are corrected by precisely changing the injection current. A phase-lock loop is used to ensure that the frequency and phase of the signal from the MZI track that of the electrical reference oscillator. Using this feedback loop ensures that *all* chirps have the same precisely targeted chirp rate and starting frequency (ω).

The linear chirp rate ensures a transform limited point-spread function in the axial dimension for the imaging system. Ensuring that the same starting frequency is maintained chirp to chirp allows coherent sums to be taken between multiple measured signals. This is necessary for the operation of tomographic imaging camera (TomICam) detailed in Chapter 6, where the raw measurements from successive sweeps are added together to obtain the measurement of the reflectivity of the imaged scene. While the described system utilizes a *feedback* loop to ensure the linearity of the sweep, this requirement can be relaxed by using a *feed-forward* system. Demonstrated feed-forward systems use the beat signal from the reference MZI to resample on a linear scale or synchronize data acquisition in the system [85].

5.5 Linearly swept frequency lasers at 850 nm and 1064 nm

We briefly describe the properties of the linearly swept frequency lasers operating at 850 nm and 1064 nm that are used as optical sources in the following chapters. These systems are chosen due to the wide availability of single mode fiber optical components at the two operating wavelengths and the availability of the optical

sources, as well as the ability for inexpensive CCD and CMOS cameras to detect the radiation from these sources. While the responsivity of CCD and CMOS cameras is higher at 850 nm, light with a wavelength of 1064 nm experiences less scattering in tissue, making it a good choice in applications where deep tissue penetration is important [97].

Custom electronics were developed to enable locking the chirp of both these lasers to an on board RF oscillator as well as to synchronize the modulation of the intensity modulator that will be described in Section 6.2.

Linearly swept 850 nm VCSEL

The experiments conducted at 850 nm utilize a VCSEL (Raycan RC13xxx2-T) with a chirp rate $\xi = 351$ GHz/ms and a duration of $T = 1.74$ ms, giving the sweep a bandwidth of $B = 612$ GHz. This bandwidth gives the ranging system a resolution of $245 \mu\text{m}$ in free space.

The laser's amplitude is kept constant using a traveling wave semiconductor amplifier (Superlum SOA-372) and the sweep is linearized using a MZI with a free spectral range of 2.88 GHz. Figure 5.6 shows the Fourier transform of the beat signal of the reference MZI once the system is locked. The two sidebands on either side of the main peak are artifacts from the finite electrical bandwidth of feedback loop. For the experiments described in the later sections, a second semiconductor optical amplifier (Superlum SOA-372) is used as an intensity modulator. The average output power from the amplifier in all experiments is roughly 2 mW.

Linearly swept 1064 nm DFB

The experiments conducted at 1064 nm utilize a QDLaser DFB (QLD1061) with a chirp rate $\xi = 106$ GHz/ms and a duration of $T = 1.8$ ms giving the sweep an optical bandwidth of $B = 190$ GHz. This resulting ranging system has an axial resolution of approximately $788 \mu\text{m}$ in free space.

The laser's amplitude is kept constant using an electronically controlled variable attenuator and the sweep is linearized using a MZI with a free spectral range of 207 MHz. Figure 5.7 shows the Fourier transform of the beat signal of the locking MZI once the system is locked. For the experiments described in the later chapters, a booster optical amplifier (Thorlabs BOA1137P) is used as an intensity modulator. The average output power from the amplifier in all experiments is roughly 15 mW.

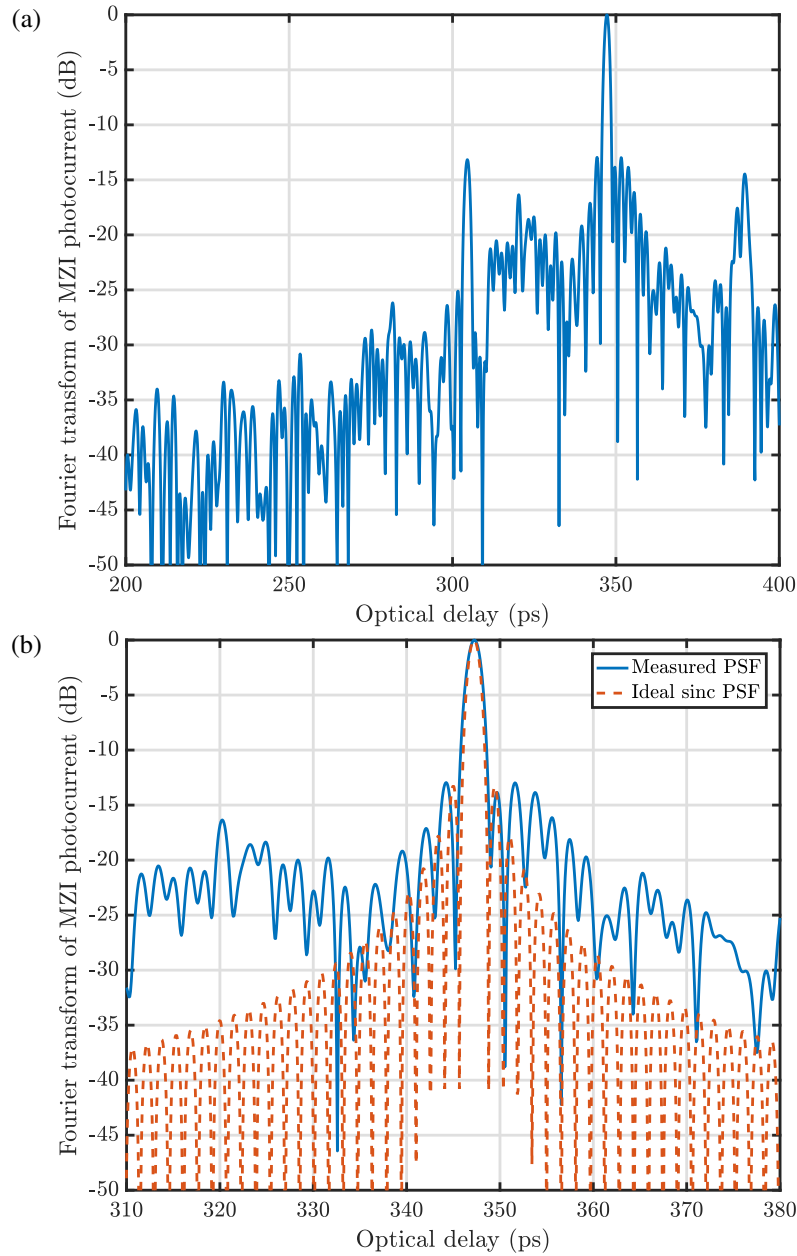


Figure 5.6: a) The PSF of the 850 nm swept frequency laser. The phase noise limited regime is apparent for delays ± 100 ps away from the delay of the MZI. The white noise floor is observable away from this region. b) Zoomed in view in to the point spread function showing excellent agreement with the expected sinc point spread function.

5.6 Conclusions

In this section, we have established the mathematical and physical foundations behind swept source optical ranging. We have defined how the optical sweep bandwidth relates to the system's ability to resolve the axial location of reflectors.

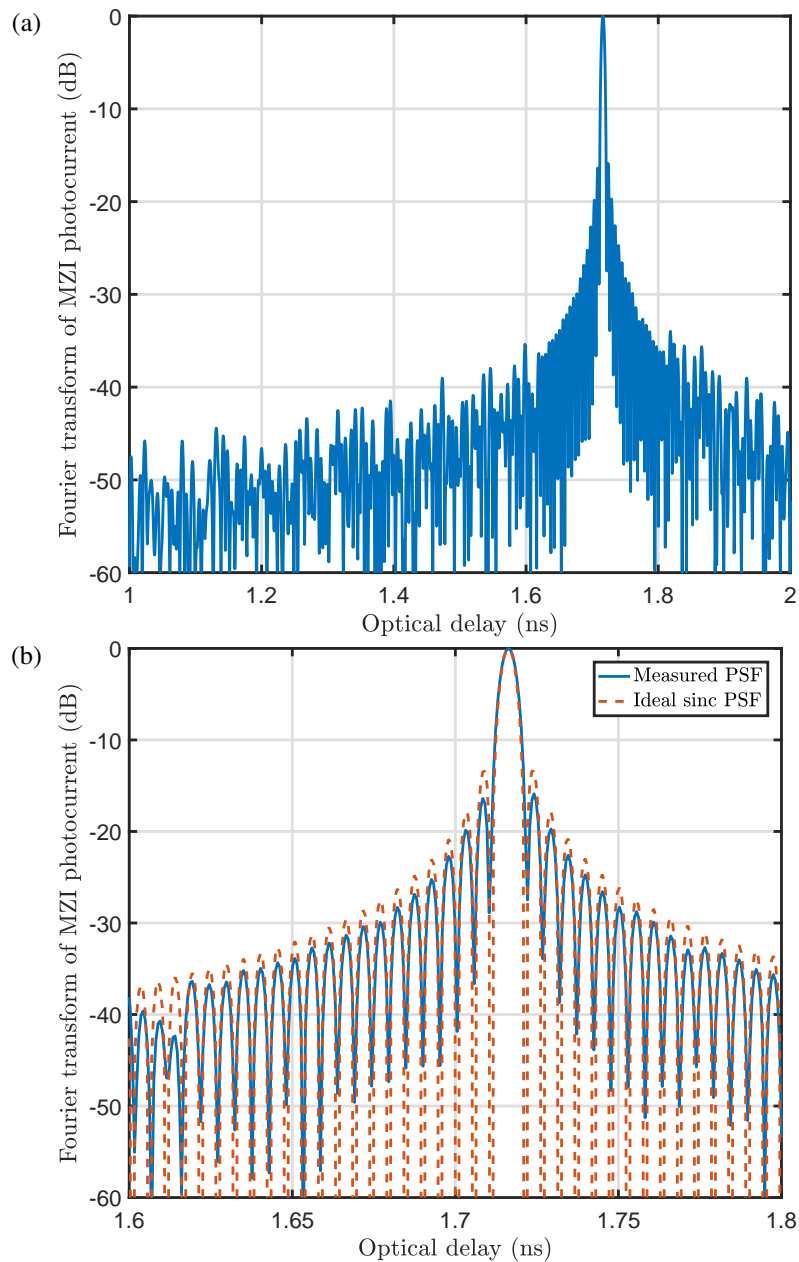


Figure 5.7: a) The point spread function of the 1064nm swept frequency laser. b) Zoomed in view in to the point spread function showing excellent agreement with the expected sinc point spread function.

We have also described the electro-optic feedback systems that ensure a linear sweep and identical starting frequency between chirps. Finally, we have highlighted the specific performance metrics of the two lasers that will be used in the subsequent experiments. In the following two chapters, we will explore how the use of swept frequency lasers in conjunction with an intensity modulator can achieve volumetric 3D imaging without the need for any moving components.

Chapter 6

3D IMAGING WITH THE TOMOGRAPHIC IMAGING CAMERA

Conventional 3D imaging acquisition using OCT involves scanning a beam over the desired field of view and acquiring axial scans at the desired lateral locations. In this chapter, we develop a novel 3D imaging modality we call the tomographic imaging camera (TomICam). Using a swept frequency laser and en-face illumination, the TomICam captures entire 2D images of reflectors originating from a particular depth, without any moving parts or beam steering technology, acquiring one tomogram with the axial resolution of OCT every four camera frames with a conventional CCD or CMOS camera sensor. Full 3D reconstruction is possible by varying the imaged depth over the desired volume of interest. In this chapter, we will describe the principle of operation of the TomICam, compare different configurations of the platform, and show experimental results utilizing both a VCSEL and a DFB as the swept source for illumination.

6.1 High resolution 3D imaging

Current 3D swept source OCT embodiments utilize rapidly sweeping MEMS VCSELs along with beam steering optics to scan the beam over the desired field of view as shown in Figure 6.1(a). While volumetric acquisition is approaching rates of 1 volume per second for images with 1000×1000 unique locations in the lateral dimensions [97], this approach poses two main challenges for future applications:

1. The frame rate decreases as the field of view increases. This is important when monitoring planar objects at high resolution.
2. Because of the potentially large time delay between the acquisition of the beat signal in adjacent pixels, the phase of the beat signal in the image may not be consistent pixel to pixel. In Chapter 7, we show how interferometric consistency across the entire field of view can be used to digitally refocus the image far beyond the conventional depth of the field of the lens.

To extend the current SSOCT imaging modality over the full field of view, it would be desirable to have an array of fast detectors, each recording the beat signal from an independent location across the field of view. Unfortunately, such high speed

detector arrays are often prohibitively expensive [98], and generate large datasets that need to be analyzed to extract the relevant information.

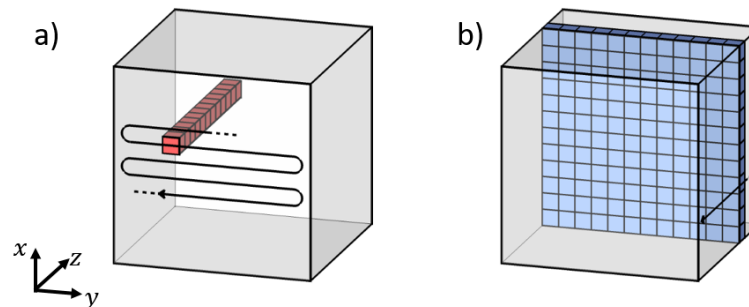


Figure 6.1: a) The 3D image acquisition strategy for many OCT imaging modalities. The axial scans (shown in red) are acquired in quick succession, utilizing a swept source. Beam steering is required to acquire information over the desired field of view. The voxels indicate the lateral (determined by the focusing optics) and depth resolution (determined by the chirp bandwidth of the optical source) of the imaging system. b) The proposed imaging system whereby individual depth slices, shown in in blue, are acquired one at a time with a standard digital sensor. The location of the interrogated depth is electronically controlled.

For many applications, it is desirable to rapidly extract the desired depth information without the need for mechanical parts or beam steering. In the following sections, we describe a novel imaging modality that utilizes a swept frequency laser, flood light illumination, along with an intensity modulator to obtain 2D sections at an electronically selected depth as illustrated in Figure 6.1(b). The computer receives information that is directly proportional to the square root of the reflectivity at the desired depth obviating the need for any costly computing. A 3D volume can be reconstructed by combining many tomographic slices over the volume of interest.

6.2 TomICam principle of operation

A system diagram of a typical configuration of the tomographic imaging camera (TomICam) is shown in Figure 6.2. All the components in front of the beam expander are based on polarization maintaining fiber making it possible to tightly package most of the required apparatus. Without the presence of any modulator, the signal received at each pixel on the camera has a large DC component, representing the average received power, with high frequency components containing the information about the depth of the reflectors. Since the bandwidth of each pixel in a typical digital camera is extremely low, the high frequency information is lost. To measure

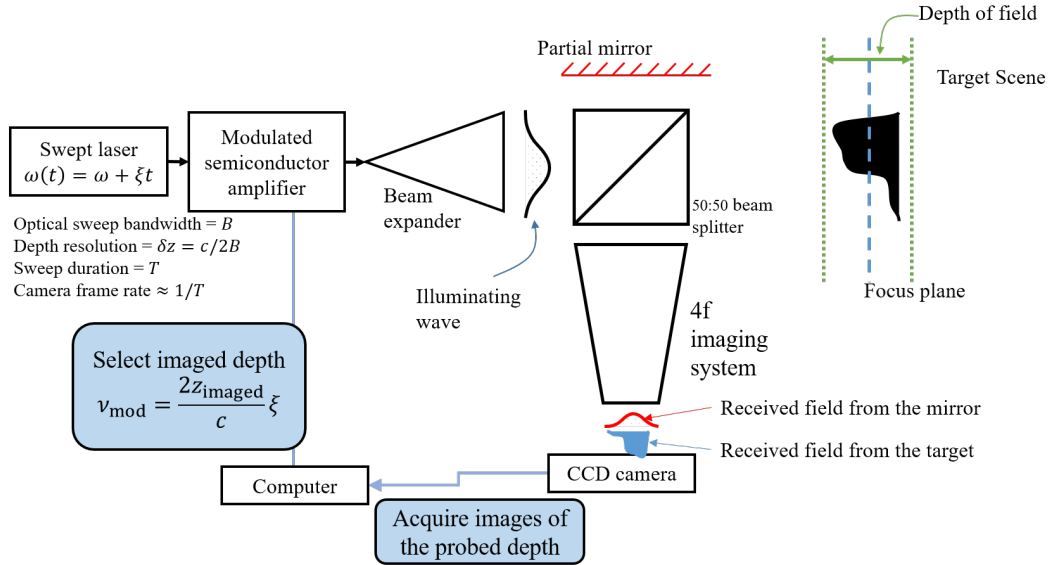


Figure 6.2: The system diagram of the tomographic imaging camera. The swept frequency laser is assumed to have a linear chirp. A computer selects the imaged depth by changing the modulating frequency of a semiconductor amplifier used as an optical intensity modulator. A 50:50 beam splitter is used to illuminate both a reference mirror and the target scene (placed within the depth of field of the lens). A $4f$ imaging system is used to simultaneously image the reference mirror and target scene.

the depth of the reflectors, a single fiber coupled optical intensity modulator is utilized to shift the high frequency information to DC where it can be recorded by the camera. In Section 6.6, we will extend our discussion to include the use of amplitude and frequency optical modulators to obtain the same measurement. The electric field out of the beam expander in the presence of an intensity modulator is given by:

$$E(t) = \sqrt{2}E_0 e^{i2\pi(\omega_0 t + \frac{1}{2}\xi t^2)} \sqrt{1 + \sin(2\pi\nu_{\text{mod}}t + \phi_{\text{mod}})} \cdot \text{rect}\left(\frac{t - T/2}{T/2}\right), \quad (6.1)$$

where ν_{mod} and ϕ_{mod} are the chosen modulation frequency and phase for the particular sweep. Because the modulator is placed in the common path, both the field from the mirror and the illuminated scene are modulated. The duration of the sweep (T) is made to match the exposure of the camera. Since the modulation frequency is electronically controlled, its value is only limited by the bandwidth of the modulator, typically in the GHz range. Following a similar derivation to that detailed in Equations 5.2-5.5, the intensity of the light received at every pixel (x, y) in the

presence of an intensity modulator is given by:

$$\begin{aligned}
I_{\text{PD}}(t, x, y, \nu_{\text{mod}}, \phi_{\text{mod}}) &= \\
&\left| \sqrt{I_m} e^{i2\pi(\omega_0 t + \frac{1}{2}\xi t^2)} \cdot \sqrt{1 + \sin(2\pi\nu_{\text{mod}}t + \phi_{\text{mod}})} \cdot \text{rect}\left(\frac{t - T/2}{T/2}\right) + \right. \\
&\quad \left. \sum_j R_j(x, y) \sqrt{I_t} e^{i2\pi(\omega_0(t - \tau_j(x, y)) + \frac{1}{2}\xi(t - \tau_j(x, y))^2)} \right. \\
&\quad \left. \sqrt{1 + \sin(2\pi\nu_{\text{mod}}(t - \tau_j(x, y)) + \phi_{\text{mod}})} \cdot \text{rect}\left(\frac{(t - \tau_j(x, y)) - T/2}{T/2}\right) \right|^2 \\
&= (1 + \sin(2\pi\nu_{\text{mod}}t + \phi_{\text{mod}})) \cdot \text{rect}\left(\frac{t - T/2}{T/2}\right) \cdot \\
&I_m \left(1 + \sum_j R_j \frac{I_t}{I_m} + \sum_j 2\sqrt{R_j(x, y) \frac{I_t}{I_m}} \cos(2\pi(\omega_0\tau_j(x, y) + \xi\tau_j(x, y)t)) \right), \quad (6.2)
\end{aligned}$$

where R_j is the reflectivity of a scatter j located at τ_j . In the expression above, we have ignored the slight phase mismatch between the reflected wave from the scatterer and that of the reference mirror. This holds if $\nu_{\text{mod}}\tau_j \ll 1$. Each pixel on the camera integrates the received intensity over the exposure time, in effect computing the inner product between the chosen modulation format, in our case a sinusoid, and the interference signal to be characterized. The image on the camera at the pixel x, y is described by

$$\begin{aligned}
N_{\text{CAM}}(x, y, \nu_{\text{mod}}, \phi_{\text{mod}}) &= \frac{\eta}{h\nu} \int_{-T/2}^{T/2} I(t) dt \approx \frac{\eta}{h\nu} I_m \left[T \left(1 + \sum_j R_j \frac{I_t}{I_m} \right) + \right. \\
&\quad \left. \sum_j 2\sqrt{R_j(x, y) \frac{I_t}{I_m}} \int_{-T/2}^{T/2} \cos(2\pi\nu_{\text{mod}}t + \phi_{\text{mod}}) \cos(2\pi(\omega_0\tau_j + \xi\tau_j t)) dt \right], \quad (6.3)
\end{aligned}$$

where N_{CAM} is the number of electrons received in one pixel (x, y) for a given modulation frequency (ν_{mod}) and phase (ϕ_{mod}), η is the quantum efficiency of the detector, h is Plank's constant, and ω_0 is the central frequency of the optical sweep. From Equation 6.3 it can be seen that only the terms containing products of the modulation $\cos(2\pi\nu_{\text{mod}}t + \phi_{\text{mod}})$ and the beating term $\cos(2\pi(\omega_0\tau_j + \xi\tau_j t))$ change as the modulation frequency and phase are varied. After computing the integral, the

equation simplifies to

$$N_{\text{CMOS}}(x, y, \nu_{\text{mod}}, \phi_{\text{mod}}) \approx \frac{\eta}{h\nu} I_{\text{mirror}} T \left[\left(1 + \sum_j R_j \frac{I_t}{I_m} \right) + \sum_j \sqrt{R_j(x, y) \frac{I_t}{I_m}} \text{sinc}(\pi(\nu_{\text{mod}} - \xi\tau_j)T) \cdot \cos(\phi_{\text{mod}} - 2\pi\omega_0\tau_j) \right]. \quad (6.4)$$

We can break down the equation to better understand the measurement:

1. The DC term ($I_m + \sum_j R_j I_t$) is the signal that would be measured at the camera in the absence of any modulation. This term is constant and independent of the chosen modulation frequency or phase.
2. The coefficient in front of the interference terms ($\sum_j \sqrt{R_j}$) is now 1 instead of 2 because the inner product between two cosines of the same frequency and phase is 1/2.
3. The sinc factor originates from the finite bandwidth of the chirp B and the fact that envelope of the modulation was constant. It gives rise to the same point-spread function discussed in Section 5.1 for a reflector at location τ_j .
4. The cos factor indicates that only one quadrature of the original beat signal is measured during one exposure. To ensure that that a target at location τ_j is visible in the measurement, one must measure the in-phase and in-quadrature portions of the beat signal at frequency $\xi\tau_j$ in consecutive measurements.

Utilizing an intensity modulator enables one to measure a specific quadrature of an arbitrary component of the Fourier Transform by shifting the desired component to DC as shown in Figure 6.3, where it is measured in parallel by the entire camera. To reconstruct the full complex interference signal N_c at a chosen depth, one can use four measurements in the following fashion:

$$N_c(x, y, \tau_j) = (N_{\text{CAM}}(x, y, \nu_{\text{mod}}, 0) - N_{\text{CAM}}(x, y, \nu_{\text{mod}}, \pi)) + i(N_{\text{CAM}}(x, y, \nu_{\text{mod}}, \pi/2) - N_{\text{CAM}}(x, y, \nu_{\text{mod}}, 3\pi/2)), \quad (6.5)$$

where the first two measurements estimate the in-phase components of the beat signal and the second two measurements estimate the in-quadrature components of the beat signal at the chosen frequency ν_{mod} . These four measurements allow one to reconstruct a tomographic slice of the illuminated volume utilizing no moving parts at the frame rate of the camera.

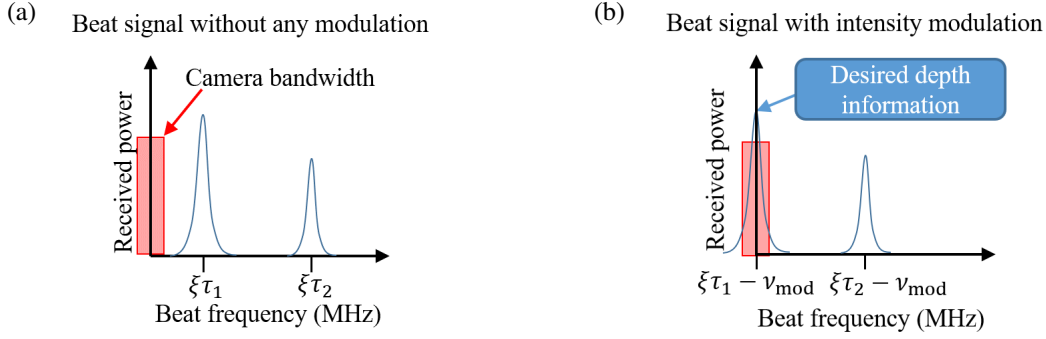


Figure 6.3: Cartoon depicting the operating principle of TomICam. Without any modulator (a), the information bearing signal is located at a much larger frequency than the bandwidth of the low frame rate camera. b) By modulating the intensity of the output light, the information is shifted to DC where it can be measured by the camera.

Tomographic reconstruction from raw measurements

To characterize the reflectivity of the scene at one depth, three components need to be quantified: the average DC power due to the non-interferometric terms, the in-phase component, and the in-quadrature term of the interference pattern. If one takes m measurements utilizing the same modulation frequency $\nu_{\text{mod}} = \xi\tau_j$, but with phases $2\pi k/m$ where k is an integer between 0 and $m - 1$, the average power is:

$$\bar{N}(x, y, \tau_{\text{mod}}) = \frac{\eta I_m T}{h\nu} = \frac{1}{m} \sum_{k=0}^{m-1} N_{\text{CAM}}(x, y, \tau_{\text{mod}}, 2\pi k/m), \quad (6.6)$$

for the case of weak reflectors $R_j \ll 1$. It is often advantageous to ensure this condition is met so as to operate the system in the shot noise limited regime, as opposed to being limited by the dark noise of the camera.

The complex interference pattern can then be estimated through

$$N_c(x, y, \tau_{\text{mod}}) = \sum_{k=0}^{m-1} \left(N_{\text{CAM}}(x, y, \tau_{\text{mod}}, 2\pi k/m) - \bar{N}(x, y, \tau_{\text{mod}}) \right) e^{i2\pi k/m}, \quad (6.7)$$

which simplifies to

$$N_c(x, y, \tau_{\text{mod}}) = \sum_{k=0}^{m-1} N_{\text{CAM}}(x, y, \tau_{\text{mod}}, 2\pi k/m) e^{i2\pi k/m}. \quad (6.8)$$

Once computed, the same signal from an swept-frequency measurement is recovered

$$N_c(x, y, \tau_{\text{mod}}) = \frac{\eta I_m T}{h\nu} \frac{m}{2} \sum_j \sqrt{R_j(x, y) \frac{I_t}{I_m}} \text{sinc}(\pi(\xi \tau_{\text{mod}} - \xi \tau_j) T) \cdot \exp(i2\pi\omega\tau_j). \quad (6.9)$$

To estimate the DC term, the in-phase, and the in-quadrature components of the interference signal we require $m \geq 3$. For static scenes, where \bar{N} can be assumed in a separate measurement, one only needs two measurements with $\theta_{\text{mod}} = 0, \pi/2$, each estimating the in-phase and in-quadrature components of the beat signal.

6.3 Comparison between different 3D imaging modalities

Another important 3D imaging modality, so far ignored in our discussion, is time domain OCT [82]. In contrast to swept-source OCT which utilizes a swept frequency laser [23], time domain OCT utilizes a large bandwidth white light source to quantify the location of the scatterer. In both cases, the optical bandwidth of the source defines the axial resolution of the system, but the choice of the source has important consequences in terms of the system design. Both OCT modalities provide much higher axial resolution than pulsed time of flight measurements (limited to the electronic bandwidth of the system) since they are only limited by the optical bandwidth of the light source (typically a few 100 GHz to 10s of THz) as opposed to that of the detector.

Briefly, time domain OCT relies on the ability to physically change the position of the reference reflector so that the time delay between the reference mirror and the interrogated depth slice is 0. Full field imaging is possible with time domain OCT and has been demonstrated as early as 1998 [99]–[102]. The demonstrated modality also acquires tomographic slices of the imaged scene and selects the interrogated depth by changing the position of the mirror so that it matches that of the reflector. If this condition is met, an interference signal is measured at the array of photodetectors. Moving the reference mirror requires either a piezo fiber stretcher, with limited depth range, or a free space setup whereby a mirror is physically scanned. Rapid acquisition of tomographic images can be of interest for PCB inspection [103] as well as in the development of 3D cell cultures [104] in novel biomedical applications. To date, swept source OCT systems have not made this leap forward without sacrificing the number of pixels acquired in the lateral resolution [105]. Full field swept source OCT could conceivably be implemented with a special detector array that measures high-frequency information as is demonstrated in [106], but since these detectors are

specialized components, that do not benefit from the advancements made in standard consumer and biomedical image sensors. If one utilizes a standard camera with SS-OCT without any modulator, a Fourier transformed of the large dataset needs to be computed before it can be meaningfully interpreted increasing the complexity of the imaging system. This is especially challenging in dynamic environments where even small movements can cause phase slips in the interference pattern, decreasing the received SNR. For these swept source OCT systems, the required frame rate is determined by the path length mismatch between the reference mirror and the scene to be imaged. Just as for the case of time domain OCT, this poses a stringent path-length matching requirement on the reference optics, which can burden the design of the imaging system and cannot be realized for cameras with ranges approaching a meter.

The proposed TomICam imaging system acquires depth slices in three to four camera frames with complete electronic control. Depth slices can be arbitrarily selected and monitored in any order, making it a versatile tool for biological or manufacturing applications. Since optical modulators can typically operate at rates up to GHz, the path-length matching requirements is greatly relaxed. As will be shown in Chapter 7, we will use the relaxed path length matching requirement to greatly extend the depth of field beyond that of the lens using holographic reconstruction.

6.4 Imaging optics

In the following section, we describe the imaging configurations used to obtain the requirement interferometric signal at the CCD camera. Two concerns are addressed in the design of the imaging system:

- The uniformity of the point spread function across the field of view.
- The optical power illuminating both the reference mirror and the target.

In the subsequent experiments, a Michelson configuration is used as shown in Figure 6.2. A beam expander is used to convert the approx $\approx 8 \mu\text{m}$ Gaussian beam from fiber to the desired beam size, approximately 10 to 30 mm in diameter. Once the beam is expanded a beam 50:50 beam splitter is used to send half the light to a wedged optical flat used as the reference partial mirror, and the other half of the light is used to illuminate the sample. In certain cases, the reflection from the wedged flat must be attenuated by neutral density filters as not to saturate the camera.

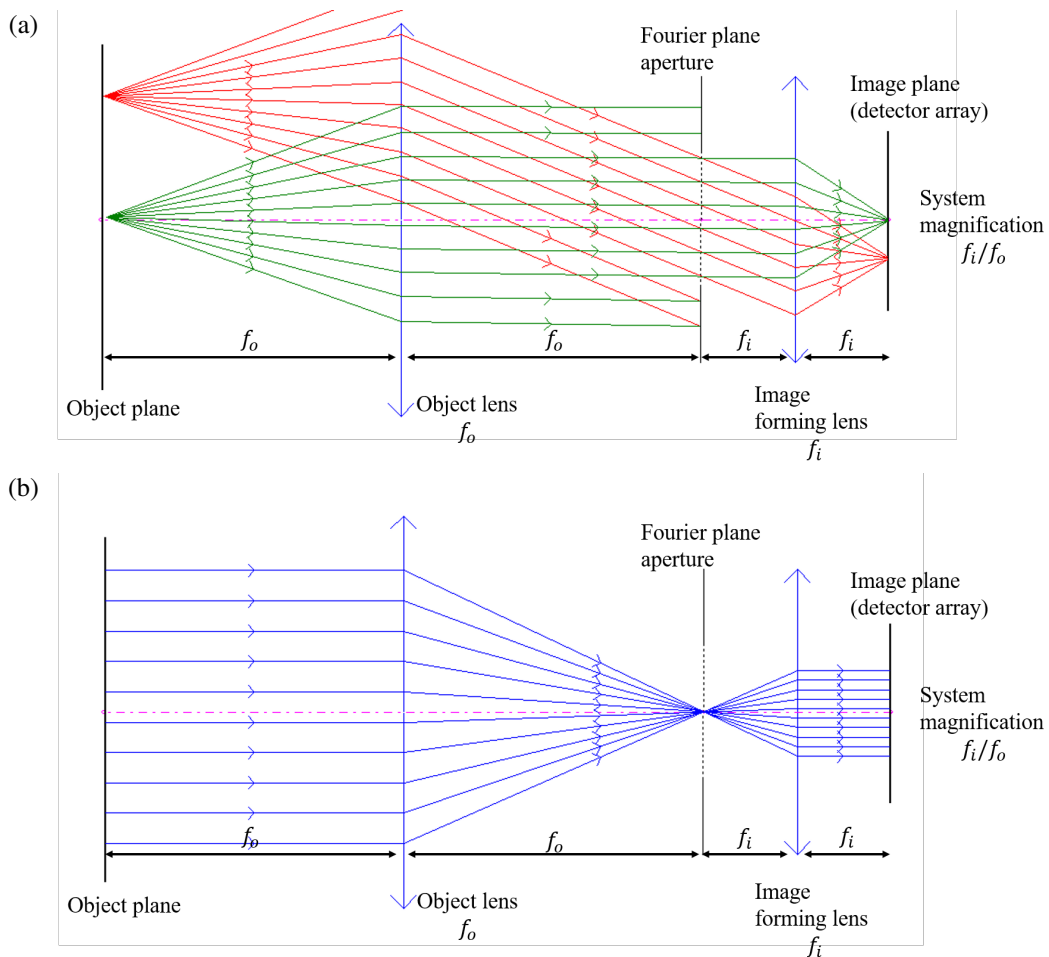


Figure 6.4: Cartoon of a $4f$ imaging system used in TomICam to simultaneously image the plane wave from the reference mirror and the object plane. A simple $4f$ system consists of two lenses placed away from an aperture at a distance exactly equal to their focal length. In this way, the object lens performs the Fourier transform of the electrical field at the object plane and the imaging lens performs the inverse transform, creating an image at the detector. The magnification is given by the ratio of the focal lengths f_i/f_o . a) Optical rays captured from two point sources located at the focus plane of the imaging system. b) A plane wave imaged through the $4f$ imaging system. At the image plane, a plane wave is recovered, allowing for a consistent interference pattern to be observed.

To image the sample and the optical reference simultaneously, a $4f$ imaging system is used. The system diagram is drawn in Figure 6.2 and the basic operating principles of a $4f$ imaging system are illustrated in Figure 6.4 obtained using ray tracing simulations. The $4f$ configuration ensures that the numerical aperture and chief ray angle are consistent over the entire field of view. This configuration guarantees that the interference pattern between the plane wave illumination and the image is

adequately sampled even at the edges of the field of view.

Within the depth of field of the imaging lens, the wavefront from scatterers can be considered to be a Gaussian beam with constant phase and a radius equal to the lateral resolution of the image. An important trade-off between lateral resolution and depth of field exists in any imaging configuration. As one increases the lateral resolution, the minimum separation between two resolvable reflectors δx decreases, but the depth of field decreases as $(\delta x)^2$. Typically, for a system with lateral resolution δx , the depth of field (δz) for a Gaussian beam is given approximately by:

$$\delta z \approx \frac{\pi}{\lambda} \left(\frac{\delta x}{2} \right)^2. \quad (6.10)$$

This limitation will be relaxed in Chapter 7 by computational refocusing the measured field profile.

6.5 Signal to noise ratio for shot noise limited measurements

The greatest challenge in acquiring images with the TomICam is illuminating the target with enough optical power to obtain a measurable signal. The camera used in our experiments has 640×480 pixels, meaning that the power in fiber is shared between 307×10^3 independent lateral locations. For weak diffuse scatterers, this makes shot noise [107] the dominant source of noise in the system. For larger optical chirps, chromatic dispersion can affect the point-spread function [108] but this limitation can be often be addressed by compensating the chirp for the expected dispersion by utilizing a non-linear chirp, or using the appropriate non-sinusoidal modulation format. An other important source of noise in the ranging system is the linearity of the optical chirp. If the chirp is non-linear, the point spread function deviates from that of a sinc function. In our implementation, the linearity of the chirp is enforced through the use of a feedback loop. Therefore, we consider the performance of the TomICam in the presence of shot noise for a given average power received from the mirror I_m and a fixed amount of average power sent onto a single reflector I_t .

For a given depth slice, measured with $m \geq 3$ measurements, the shot noise is determined by the total number of electrons collected at the camera in one pixel. Since shot noise is uncorrelated between measurements, the variance of the noise in one TomICam measurement is equal to the sum variance of the shot noise in each

measurement:

$$\text{Var} [N_c] = \sum_{k=0}^{m-1} \text{Var} [N_{\text{CMOS}}(x, y, \tau_{\text{mod}}, k \cdot 2\pi/m)] \quad (6.11)$$

$$= m \frac{\eta I_m}{h\nu} T. \quad (6.12)$$

For the case of a single reflector ($j = 1$) located at $\nu_{\text{mod}} = \xi\tau_j$, the power in the signal is given by taking the modulus square of Equation 6.8

$$|\text{Mean} [N_c]|^2 = \left| \frac{\eta}{h\nu} T \frac{m}{2} \sqrt{R_1(x, y) I_t I_m} \exp(i(\phi_{\text{mod}} - \omega_0 \tau_j)) \right|^2 \quad (6.13)$$

$$= \left(\frac{\eta}{h\nu} T \right)^2 \frac{m^2}{4} R_1(x, y) I_t I_m. \quad (6.14)$$

The signal to noise ratio (SNR) in the measurement is thus:

$$\text{SNR} = 10 \log_{10} \frac{|\text{Mean} [N_c]|^2}{\text{Var} [N_c]} = 10 \log_{10} \left(\frac{\eta}{h\nu} T \right) \frac{m}{4} R_1(x, y) I_t \quad (6.15)$$

$$= -6 + 10 \log_{10} m \left(\frac{\eta}{h\nu} T \right) R_1(x, y) I_t. \quad (6.16)$$

The equation above indicates that TomICam decreases the measured SNR by 6 dB compared to a time resolved swept-source OCT measurement. The decrease in the SNR by 6 dB originates from the fact that the inner product between two cosines is 1/2, giving the measurement 1/4 of the signal's original power.

6.6 Compatible modulation formats

We discuss different modulation formats that are compatible with a TomICam measurement setup that have the potential improve the SNR of the acquisition system. We define a TomICam measurement as one that is able to obtain depth resolved tomographic images with a resolution determined by the optical bandwidth of the swept source, utilizing a standard of-the-shelf camera.

Intensity modulation

The case of intensity modulation has been discussed with the typical system configuration shown in Figure 6.2. The intensity modulator must be modulated at a frequency proportional to the expected beat signal $\xi\tau_j$ where τ_j is the optical path-length mismatch between the reference mirror and sample. The intensity modulator must be used in the linear regime to ensure that each scatterer only appears as a single reflector in the axial domain. For example, gain saturation in semiconductor amplifiers can create harmonics of the fundamental frequency in the output power of the laser causing a single target to appear in multiple depth slices.

One important consideration that has so far been ignored is that the beating terms from two scatterers ($\xi(\tau_j - \tau_{j'})$) in the imaged scene will also be shifted to DC where it can be measured. This can make it hard to differentiate the signal of interest from beating terms originating from the product of two scatterers in the scene. To avoid this issue, one can bias the location of the reference mirror so that the beating terms of interest ($\xi\tau_j$) are located at high frequencies compared to the unwanted cross terms ($\xi(\tau_j - \tau_{j'})$).

Amplitude modulation

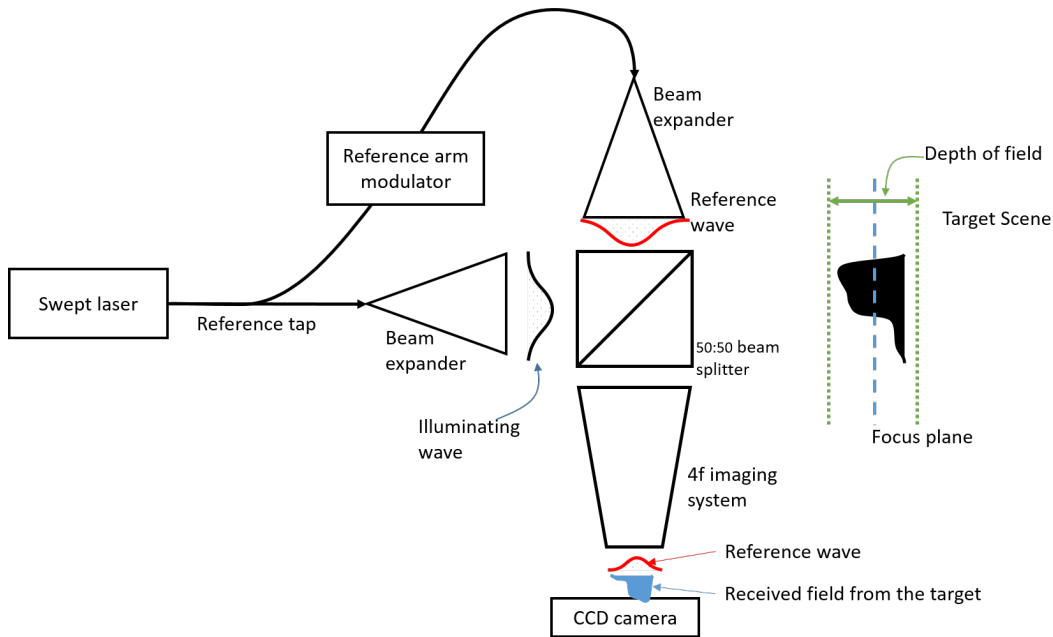


Figure 6.5: System diagram of the tomographic imaging camera utilizing a modulator in the reference arm and a Mach-Zehnder interferometer. The reference tap coupler need not be a 50:50 coupler. In this configuration, the modulator is only used to modulate the properties of the reference arm, enabling the use of amplitude and frequency modulators to obtain TomICam measurements.

An amplitude modulator can be used to obtain TomICam measurements if it is placed in one arm of the interferometer. Such a configuration using a Mach-Zehnder interferometer is shown in Figure 6.5. Contrary to the case of the intensity modulator, only the reference field of the interferometer is modulated. All properties of the illuminating field are kept constant during the measurement. In this system, E_{mirror} is given by

$$E_{\text{mirror}} = \sqrt{I_m^{(\text{AM})}} \cos(2\pi\nu_{\text{mod}} + \theta_{\text{mod}}). \quad (6.17)$$

We choose $I_m^{(\text{AM})} = 2I_m$ to ensure that the average power received from the mirror is the same as in the case of the intensity modulator. Equation 6.2 becomes

$$N_{\text{AM}}(x, y, \nu_{\text{mod}}, \phi_{\text{mod}}) = \frac{\eta}{h\nu} \int_{-T/2}^{T/2} I(t) dt \approx \frac{\eta}{h\nu} \left[T \left(I_m + \sum_j R_j I_j \right) + \sum_j 2\sqrt{R_j(x, y) I_t \cdot 2I_m} \int_{-T/2}^{T/2} \cos(2\pi\nu_{\text{mod}}t + \phi_{\text{mod}}) \cos(2\pi(\omega_0\tau_j + \xi\tau_j t)) dt \right], \quad (6.18)$$

yielding a measurement similar to that of the case where an intensity modulator is used:

$$N_{\text{AM}}(x, y, \nu_{\text{mod}}, \phi_{\text{mod}}) \approx \frac{\eta}{h\nu} T \left[\left(I_m + \sum_j I_t R_j \right) + \sum_j \sqrt{2R_j(x, y) I_m I_t} \text{sinc}(\pi(\nu_{\text{mod}} - \xi\tau_j)T) \cdot \cos(\phi_{\text{mod}} - 2\pi\omega_0\tau_j) \right], \quad (6.19)$$

with the key difference being that the interference term is $\sqrt{2}$ times larger than the case of acquiring TomICam with an intensity modulator, resulting an increase of 3 dB of the SNR. Equation 6.7 can be used to reconstruct the chosen depth slice τ_j . One challenge in using an amplitude modulator is that the most common amplitude modulator, an MZI modulator, is often not linear through the full range of operation [6] ($E_{\text{out}} = E_{\text{in}} \sin(V_{\text{applied}})$ and not $E_{\text{out}} = E_{\text{in}} \cdot V_{\text{applied}}$ as is required for a linear modulator). Any harmonics in the output field modulation can cause the targets to appear at locations equal to integer fractions of ν_{mod}/ξ in addition to their true location.

Frequency modulation

Using an acousto-optic frequency modulator can also yield a similar measurement to the two described above. In this case, the electrical field from the reference arm is shifted by the modulation frequency ν_{mod} :

$$E_{\text{mirror}} = \sqrt{I_m^{(\text{FM})}} \exp^{j(2\pi\nu_{\text{mod}}t + \theta_{\text{mod}})}, \quad (6.20)$$

with $I_m^{(\text{FM})} = I_m$. Equation 6.3 becomes:

$$N_{\text{FM}}(x, y, \nu_{\text{mod}}, \phi_{\text{mod}}) = \frac{\eta}{h\nu} \int_{-T/2}^{T/2} I(t) dt \approx T \left[\left(I_m + \sum_j R_j I_t \right) + \sum_j 2\sqrt{R_j(x, y) I_t I_m} \int_{-T/2}^{T/2} \cos(2\pi(\omega_0 \tau_j + \xi \tau_j t) - (2\pi\nu_{\text{mod}} t + \phi_{\text{mod}})) dt \right] \quad (6.21)$$

and simplifies to

$$N_{\text{FM}}(x, y, \nu_{\text{mod}}, \phi_{\text{mod}}) \approx \frac{T}{4} \left[\left(I_m + \sum_j I_t R_j \right) + \sum_j 2\sqrt{R_j(x, y) I_t I_m} \text{sinc}(\pi(\nu_{\text{mod}} - \xi \tau_j) T) \cdot \cos(\phi_{\text{mod}} - 2\pi\omega_0 \tau_j) \right], \quad (6.22)$$

yielding a similar result to the case of intensity modulation. In this case, the interference term of interest has a coefficient of 2 instead of 1, as the case using an intensity modulator resulting in an increase of the SNR by 6 dB. This makes the SNR of the TomICam system identical to that of a high-speed photodetector.

Summary of modulation formats

In Table 6.1 we summarize the different types of modulation formats that are compatible with TomICam.

Modulation format	Modulator placement	SNR reduction	Compatible modulators
Intensity modulator	Common arm	-6 dB	Semiconductor amplifier or linearized MZI modulator
Amplitude modulator	Reference arm	-3 dB	Linearized MZI modulator
Frequency modulator	Reference arm	0 dB	Acousto-optic frequency shifter

Table 6.1: Summary of the different modulators that can be used to obtain 3D measurements with the TomICam.

6.7 Experimental results at 850 nm

We begin with an experiment imaging a scene containing specular reflectors: a coin and a sheet of paper. The scene as imaged with light illumination is shown in Figure 6.6 (a). For the TomICam measurements, the laser illumination is concentrated

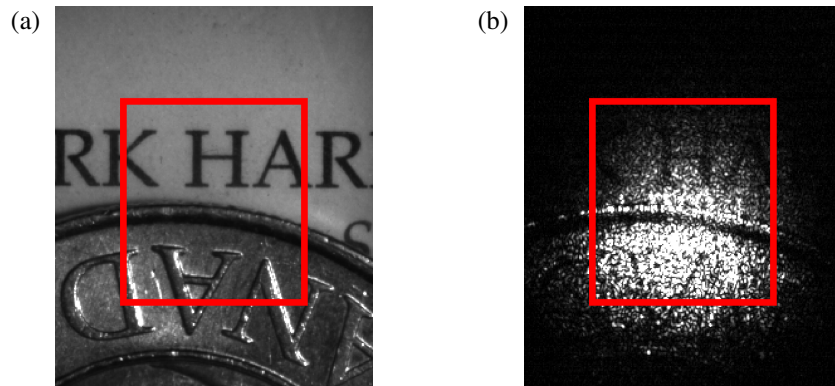


Figure 6.6: (a) The the imaged scene when illuminated with white light. No obvious depth discrimination is observed between the coin and the piece of paper. (b) The same image as illuminated with the 850 nm laser without the reference mirror or any modulation. The region of interest, 160×144 pixels in size, corresponding to 7.7×6.9 mm, is outlined in red.

on a small region (≈ 7 mm in diameter) highlighted in the aforementioned figure to reduce the exposure time. Each camera frame has an exposure of 2 ms, enough to capture a single sweep of the 850 nm VCSEL lasting 1.74 ms with a bandwidth of 612 GHz, giving the system an axial resolution of $244 \mu\text{m}$. The illuminated area of 160×144 pixels (Lucam Lu075M) is acquired at a rate of 40 frames per second (10 tomograms per second). Depth slices are interrogated sequentially from locations $z = 73$ mm to $z = 133$ mm in increments of $61.3 \mu\text{m}$ (or $1/4$ of the axial resolution (Δz)). We show tomographic measurements from three different depth slices in Figure 6.7 (a-c) corresponding to the depth of the coin, the bevel of the coin, and the paper. Each tomogram only shows the reflectors at the interrogated depth. Figure 6.7 (d) shows a depth slice within the depth of field of the image but where no scatterers exist, yielding a measurement of a nearly black frame, as expected.

Figure 6.8 shows the raw data acquired when the phase of the modulation is set to $\pi/2$ at a pixel located on the coin's face. The reconstructed A-scan on a dB scale is shown to illustrate the dynamic range of the system. Good agreement is seen between the A-scan obtained with the TomICam and the point spread function (PSF) of the swept frequency laser. The same sidebands that appear on the A-scan are the predicted true PSF shown in Figure 5.6. While these sidebands cause one target to appear as three targets, they can be minimized through better linearization of the laser. While the acquisition rate of a single A-scan using the TomICam is slower than scanned OCT embodiments, each tomogram is acquired in only four camera frames, for a total exposure of 8 ms. The noise-level of the acquisition system

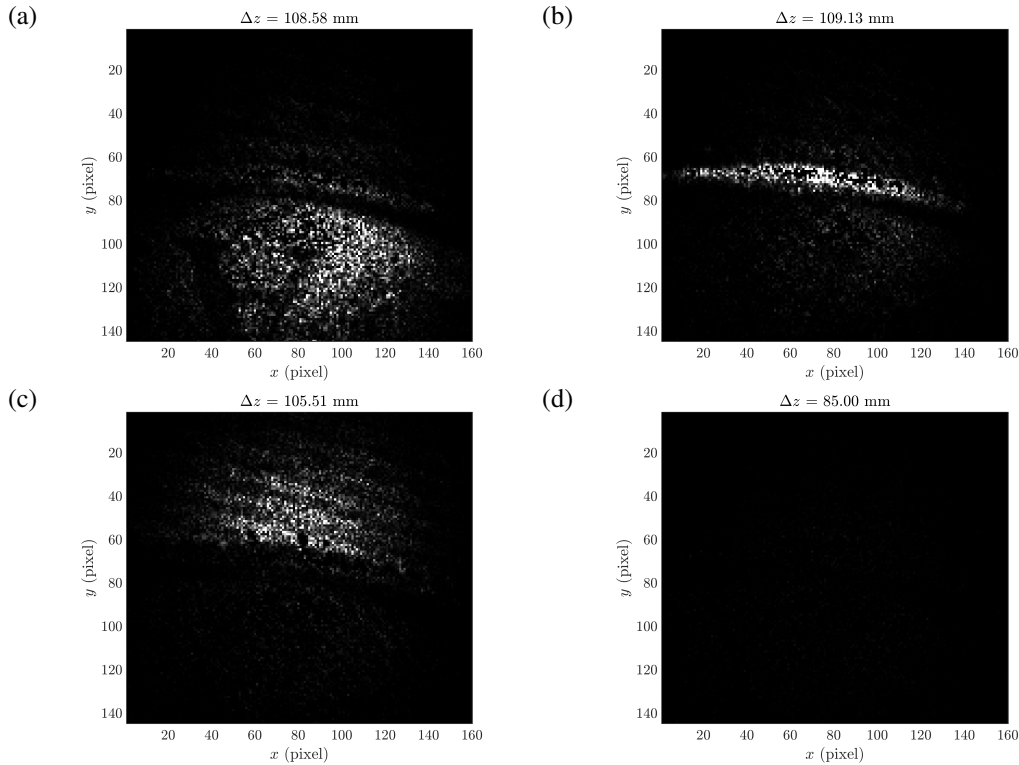


Figure 6.7: Tomographic images (C-scans) of the scene shown in Figure 6.6 at various depth slices. The intensity of the image corresponds to $2I_{\text{mirror}}I_{\text{target}}(z)$ as computed with Equation 6.5. Four depths of interest are shown corresponding to the depth of the coin’s face (where one can read the letter “A”), the bevel of the coin, the piece of paper, and a depth far away from any reflector. Black corresponds to a value of 0 photo electron², while white corresponds to $(3 \times 10^3 \text{ photo electron})^2$.

away from the FMCW peak (49.2 dB), matches the expected shot noise level from the measurement to within 1 dB (predicted to be 48.4 dB). The the shot noise is estimated by taking the variance of the computed TomICam signal between a depth of 73 mm and 82 mm far enough from the reflector as to ignore the phase noise of the laser.

6.8 Experimental results at 1064 nm

We present two experiments utilizing a swept frequency DFB laser at 1064 nm with a chirp bandwidth of 180 GHz. Both experiments utilize the configuration shown in Figure 6.2 but with different beam expanders. While this laser has a smaller chirp bandwidth than the laser at 850 nm, the chirp linearity is greatly improved, yielding a better point spread function.

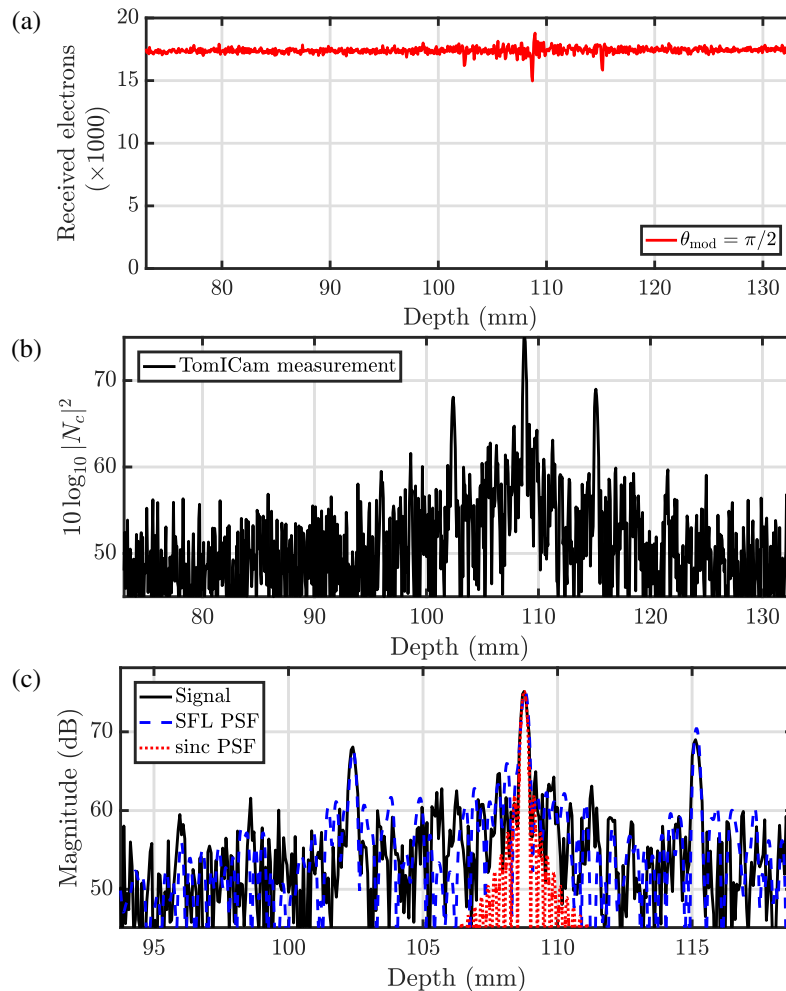


Figure 6.8: Raw measurement and reconstructed A-scan obtained from 980 tomographic slices at pixel $(x, y) = (75, 90)$ in Figure 6.7. The tomographic slices are taken at depths separated by $61 \mu\text{m}$, $1/4$ of the system’s axial resolution. a) The raw measurement where non-interferometric DC term appears in all depth slices. b) The reconstructed A-scan on a logarithmic scale as computed with Equation 6.5. c) TomICam measurement superimposed with the measured point-spread function in the axial dimension of the laser and the expected axial point spread function expected from a perfectly linear sweep of the laser.

Imaging retro-reflective glass beads

In this experiments, three letters, “C”, “I”, and “T” are drawn on glass cover slides utilizing retro-reflective glass beads 30 to $100 \mu\text{m}$ in diameter [109], roughly equal to the lateral resolution of the system ($62 \mu\text{m}$)¹. The three letters are placed near the depth of field ($\delta z = \pm 25 \text{ mm}$), at slight angles to give each letter a depth

¹While efforts were made to remove stray glass beads from the cover slides, unwanted glass beads remained and may appear, at first sight, as noise in the system.

profile as well as to remove the reflection from the glass slide from the image. The reference mirror is formed from the a surface of a glass wedge. A conventional imaged, acquired with coherent illumination, and a sketch of the setup are shown in Figure 6.9

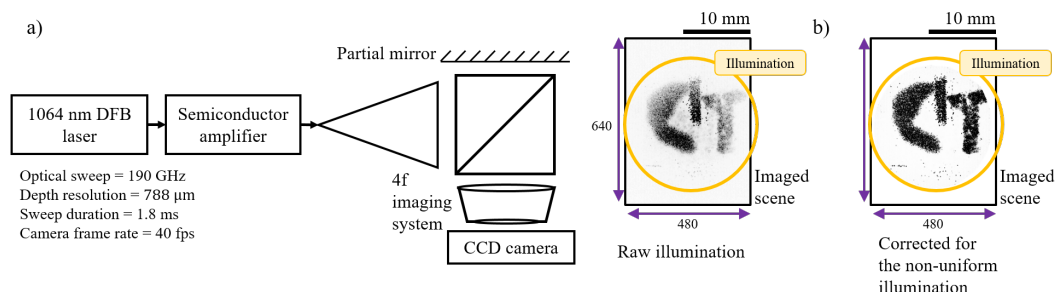


Figure 6.9: a) The setup used to acquired tomographic images of the letters “C”, “I”, and “T” draw with retro-reflective glass beads on different cover-slides, all placed located the depth of field of the imaging optics. While the illumination is not uniform, we removed this artifact from the images by normalizing all results shown in this section by the illumination profile as shown b).

Each camera frame is acquired in 1.8 ms matching the sweep duration of the DFB laser. The nearly Gaussian illumination profile is measured before the acquisition of tomographic slices by measuring the received intensity from the glass wedge when the target scene is blocked. The illumination profile ($I_0(x, y)$) is then used to normalize the images so that they appear to have uniform illumination.

Depth slices are interrogated in succession to acquire volumetric information from the 3D scene. We show the resulting depth slice that contains the letter “C”, $\Delta z = 128.1$ mm away from the reference mirror acquired in four successive camera frames with modulation frequency $\nu_{\text{mod}} = (2z/c)\xi$. Figure 6.10 shows the result of the in-phase component and in-quadrature components. To obtain the full intensity image, the in-phase measurement and the in-quadrature measurement are added coherently to create the final tomographic image Because of the a tilt that has been imposed on the letter “C”, the full letter appears in two (2) different depth resolved tomograms. This is shown in Figure 6.11, where we the acquired tomographic slices at locations $z = 128.5$ mm and $z = 127.7$ mm show the left and right half of the letter.

The letters “I” and “T”, located at depths $z = 180.1$ mm and $z = 209.2$ mm respectively, are shown in Figure 6.11. Finally, 305 tomographic acquisitions, are used to reconstruct a full 3D model shown in Figure 6.12(a). The point cloud is

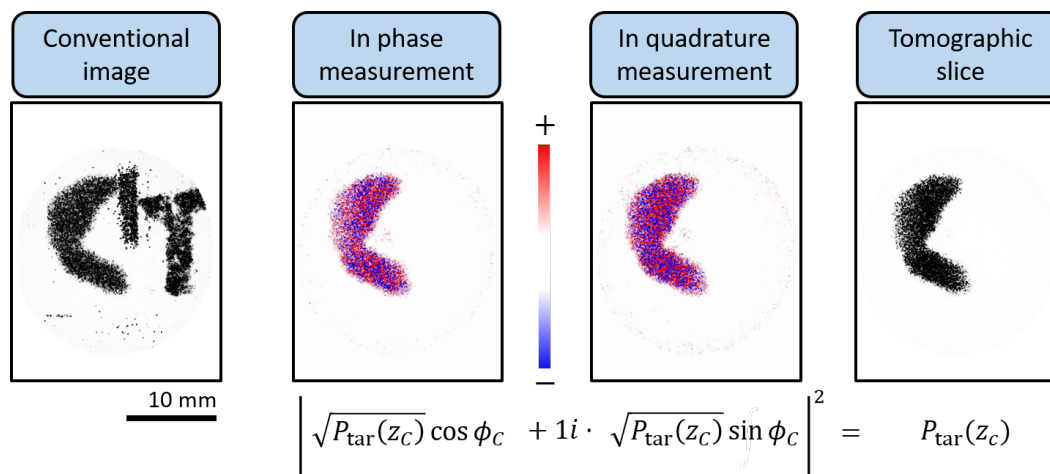


Figure 6.10: The specific depth slice slice containing the letter “C” interrogated in the four successive frames (two frames for the in-phase measurement, two frames for the in-quadrature experiment). Black pixels correspond to 1600 electrons collected from the target.

rendered by only showing the voxels (3D locations) that have received more than 10 signal electrons in the TomICam measurement. An axial scan (typically referred to as an A-scan) can be reconstructed with a sample shown in Figure 6.12(b). The location of a reflector from the reflectors that form the letter “I” and “T” are clearly recognized illustrating the ability of the tomographic imaging camera to naturally quantify multiple reflections.

Imaging weak reflectors with a swept source 1064 nm laser

In this section we demonstrate the ability of the TomICam to image weak diffuse targets by averaging the signal over the multiple sweeps in a single camera frame. We image a piece of paper containing the Caltech seal printed in black. Since the reflectivity of the target is much smaller than that of the retro-reflective beads in the previous experiment, each the exposure of the camera frame is increased to 50 ms, enough to average 25 optical sweeps each having a duration of 1.8 ms, keeping the modulation frequency and phase constant during each camera frame. The 2.2 ms of dead time between chirps is used to ensure that the starting frequency of the laser is the same between sweeps. To decrease the optical power from the reference arm, neutral density filters are placed in front of the optical wedge so that the power matches the received power from the piece of paper. The Caltech seal is tilted away from the camera to give the scene a slight z dependence. Figure 6.13 shows the imaged scene seen with white light illumination. With white light illumination,

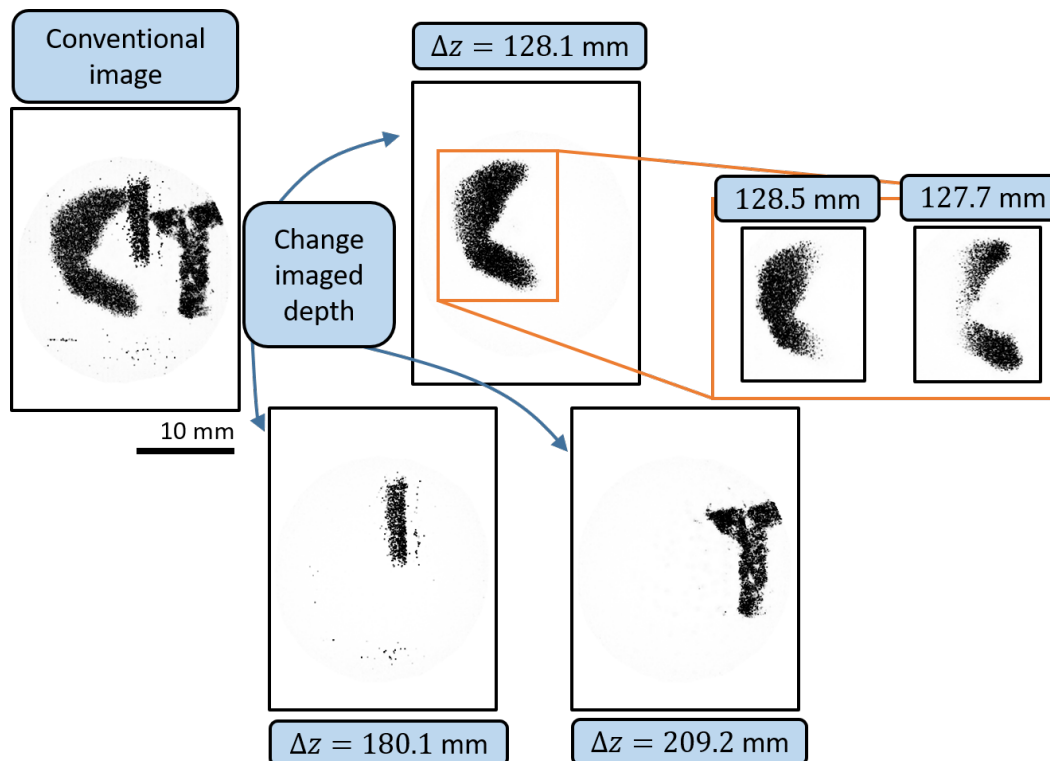


Figure 6.11: The tomographic slices acquired for three different depths z corresponding to the depths of the letters “C”, “I”, and “T”.

the exact orientation of the inclination cannot be known with high precision. The illuminated area has been reduced, to approximately 250×250 pixels in size corresponding to an area of 12×12 mm, in order to collect more power in each pixel. In this experiment, tomograms are acquired at depths in increments of a quarter of the axial resolution ($\Delta z/4 = 196 \mu\text{m}$.) Figure 6.13 shows individual tomograms of the reflectivity of the scene at three depths of interest separated by the axial resolution of the ranging system (Δz). A lateral depth map of the reflector can also be constructed from the measurements by taking the location of maximum reflectivity from all tomograms. Axial scans taken from three pixels separated by the axial resolution of the system are shown to demonstrate that the system is able to fully resolve the location of the reflectors.

6.9 Conclusions

In this chapter we have demonstrated a novel 3D imaging modality that is able to obtain tomographic images with an axial resolution determined by the bandwidth of the optical chirp without requiring beam scanning or moving parts. The imaging modality can make use of an optical intensity modulator, amplitude modulator,

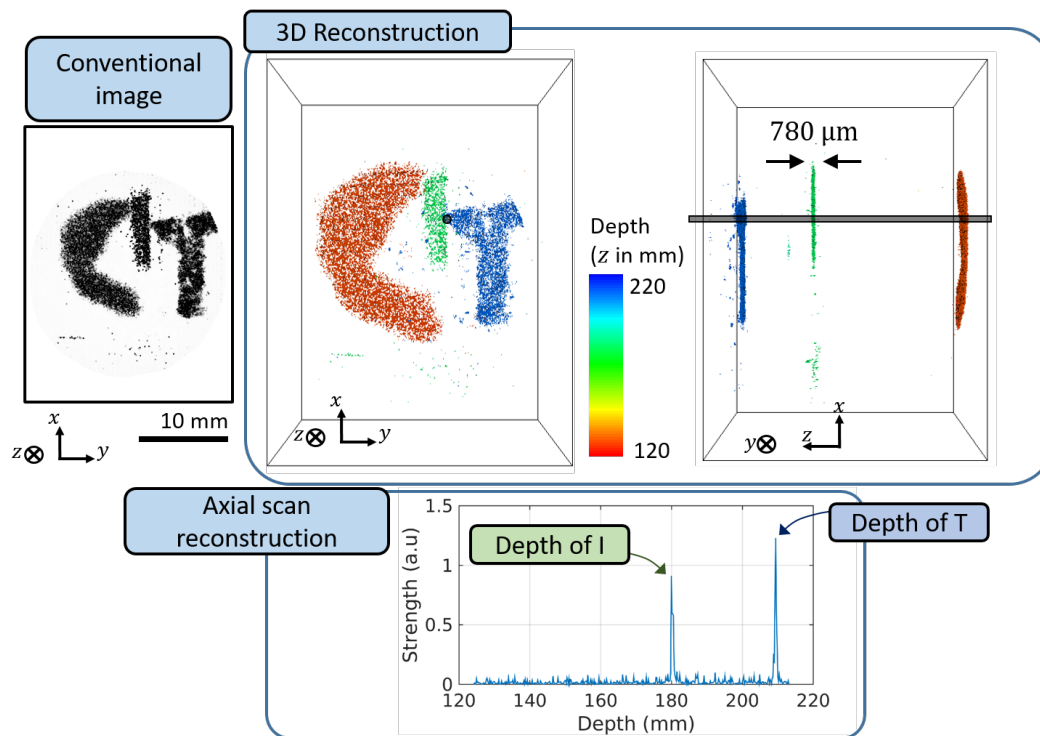


Figure 6.12: 3D reconstruction of the scene imaged with the tomographic imaging camera. (Bottom) An axial scan, showing two well resolved reflectors, corresponding to reflectors from the letter “I” and “T”.

or frequency modulator to obtain tomograms, and selects the imaged depth by electronically changing the modulation frequency of the chosen modulator. Finally, demonstrations of the operating principle of the tomographic imaging camera with a linearized swept frequency laser operating at 1064 nm and 850 nm were shown.

The demonstrations in this chapter have been restricted to scatterers located within the depth of field of the imaging system and have ignored the correlation in the information acquired in adjacent pixels. Each pixel on the camera is interpreted independently. In the next chapter, we will utilize the intensity and phase information acquired in adjacent pixels within a single tomographic slice to digitally refocus the acquired images and greatly extend the depth of field of the tomographic imaging camera.

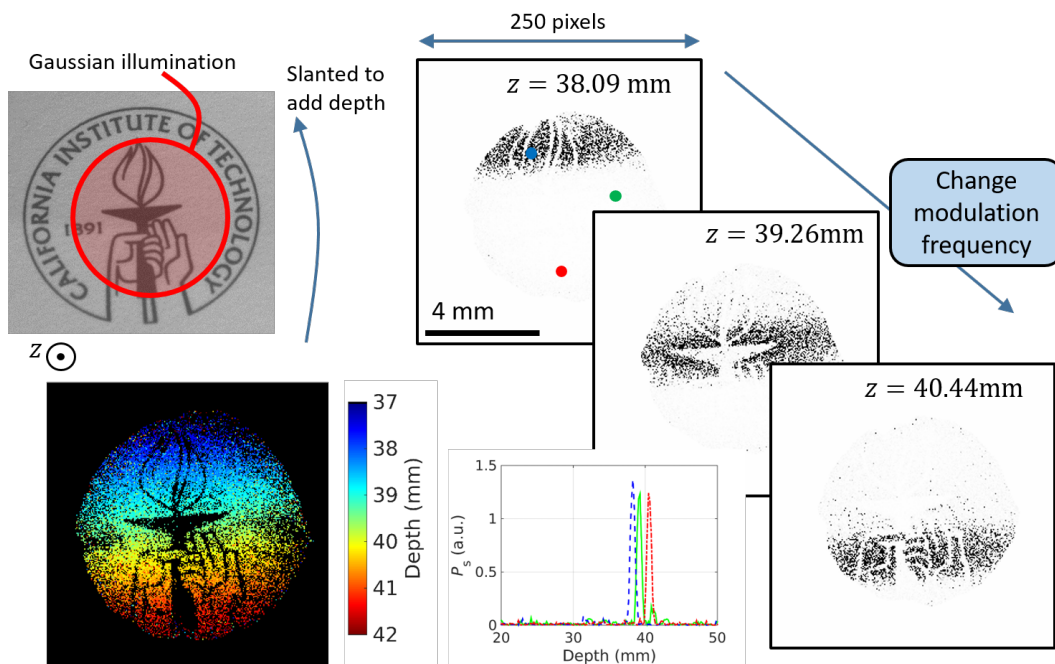


Figure 6.13: The imaged scene (250×250 pixels) containing a single reflector per lateral location consisting of a piece of paper with the Caltech logo printed in black ink. A profile of the piece of paper, shown in color, can be formed by recording the depth slices where the maximum reflection is measured. Axial scans are reconstructed from the en-face tomograms to show the ability of the tomographic imaging camera to resolve locations separated by the axial resolution of the system ($788 \mu\text{m}$).

IMAGING BEYOND THE DEPTH OF FIELD

In the previous chapter, we focused our discussion on the ability of the TomICam to measure the location of reflectors when they are located within the depth of field of the imaging lenses. In this case, a strict tradeoff exists between the lateral resolution of a system and the imaging depth of field. If one decreases the minimum resolvable spot size in the lateral dimension, the depth over which ranging is possible is decreased. It is often desirable to overcome this limitation and image beyond the depth of field of an imaging system [110]. In this chapter, we will exploit the property that the tomographic imaging camera acquires all pixels in the field of view simultaneously to obtain depth resolved high resolution images that are located far beyond the conventional depth of field. To do so, TomICam will use the measured electric field profile (in contrast to the intensity profile) and the precise knowledge of the location of the reflectors to refocus the acquired images in a single mathematical operation.

7.1 Depth of field of a $4f$ imaging system

In contrast to incoherent imaging systems, the TomICam records the complex field reflected from a chosen depth by beating the reflected light with a reference wave. As such, it is necessary to analyze the imaging system by its amplitude transfer function and not the intensity transfer function. We restrict our discussion to the case of a $4f$ system where two lenses are arranged as shown in Figure 6.4 to create an image at the detector array, the digital camera. The advantage of a $4f$ imaging system is that the amplitude transfer function of the electrical field is shift invariant across the entire field of view. We define $U_o(x, y)$ and $U_i(x, y)$ as the electric field at the object and image plane respectively and $\tilde{U}_o(f_x, f_y)$ and $\tilde{U}_i(f_x, f_y)$ as their spatial Fourier transform. For a $4f$ imaging system, they are related by

$$\tilde{U}_i(f_x, f_y) = \tilde{U}_o(M \cdot f_x, M \cdot f_y)P(f_x, f_y), \quad (7.1)$$

where M is the magnification of the system given by the ratio between the focal length of the collecting lens and the focal length of the image forming lens and $P(f_x, f_y)$ is a function of the aperture at the Fourier plane of the imaging system. Typically (and in our experiments), P is a low-pass spatial frequency filter.

In this case the lateral resolution is determined by the aperture P . For a coherent illumination system, the resolution (Δx and Δy) is related to $\Delta x \approx 1/\max(f_x)$ and $\Delta y \approx 1/\max(f_y)$. The effects of the finite resolution of an optical system are readily observable by simulating a Siemens star target [111]. The Siemens star, shown in Figure 7.1, is a radial pattern with alternating black and white stripes. A unique feature of the Siemens star is that the resolution of the imaging system can be readily identified by looking at the smallest circle where the black and white fringes are no longer seen. Figure 7.2 shows how a Siemens star appears on a detector when it is illuminated with coherent light with $P(f_x, f_y) = 1$ for $\sqrt{f_x^2 + f_y^2} < 5 \text{ mm}^{-1}$ and $P(f_x, f_y) = 0$ elsewhere. For this simulated system, fringes no longer become

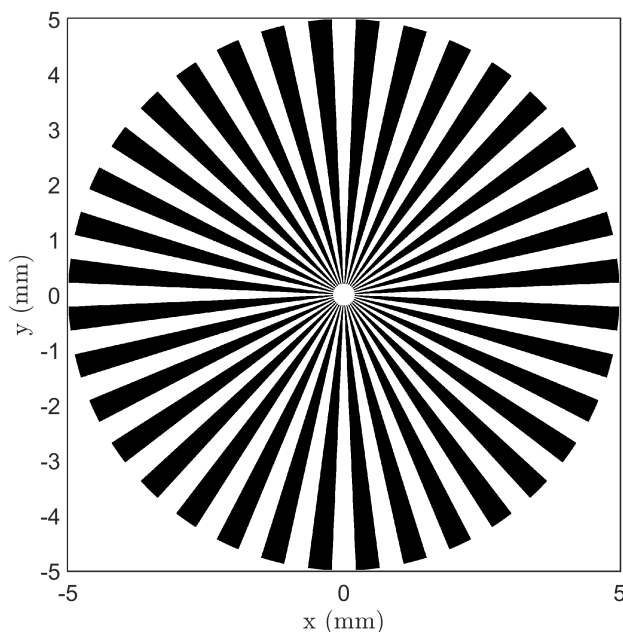


Figure 7.1: A Siemens star target with 36 pairs of spokes. Spokes in black do not reflect light while spokes in white do. This particular Siemens star has an outer radius of 5 mm and an inner radius (all white) of 200 μm .

visible below a radius of 1.1 mm. The information required to resolve the spokes below a this radius is located at higher spatial frequencies than those passed by the spatial filter (realized by placing a pupil in the Fourier plane of the imaging system). Rather than being perfectly black or white, the image within this circle appears gray. In the next sections, we will explore how this same target appears for a coherent illumination system as it is moved out of focus.

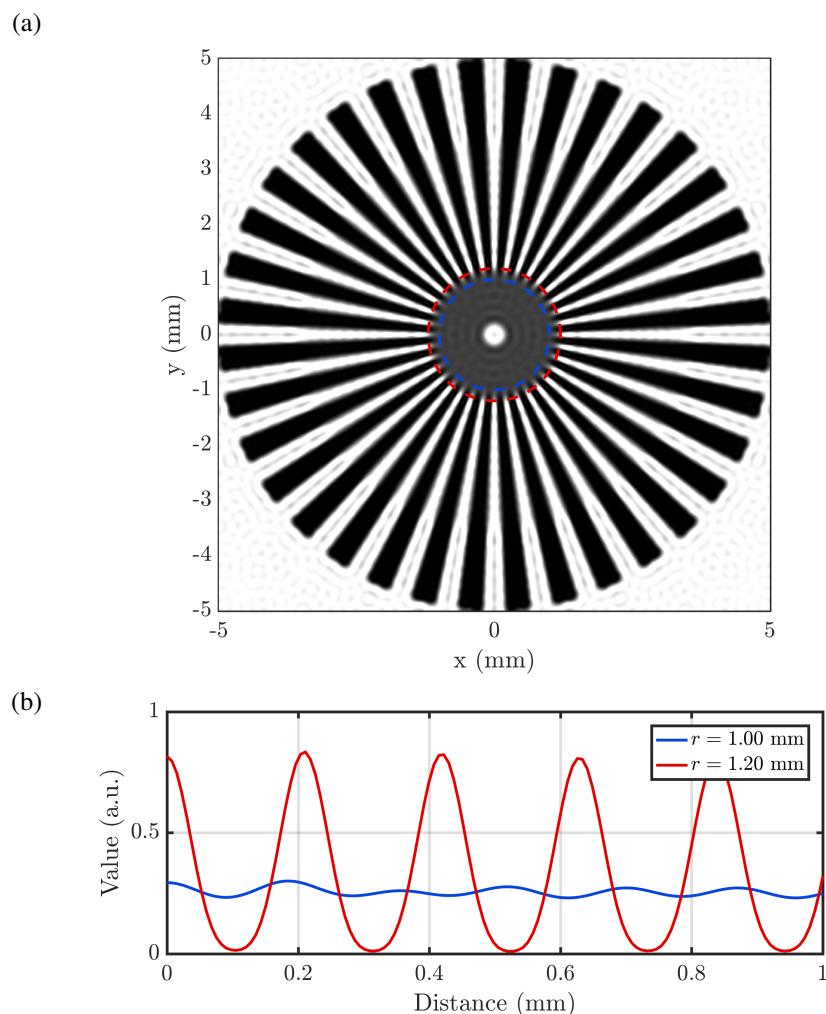


Figure 7.2: The simulated intensity profile at the image plane of a Siemens star when imaged by a coherent imaging system with cutoff frequency of 5 mm^{-1} . The intensity profile is plotted in (b) along the dashed lines shown in (a).

Depth of field for coherent illumination

Here we consider the case where a reflector is located at a distance $z \neq f_o$ away from the object lens. If the offset $z - f_o$ is small, then one can often ignore any effects arising from diffraction and assume that Equation 7.1 still holds. For Gaussian beams, this is typically known as the Rayleigh range, where full width half maximum of the electric field profile increases by a factor of $\sqrt{2}$ [6]. For larger offsets, the beam waist increases and images become hard to discern. For incoherent illumination systems, it is challenging, though not impossible [112], to undo the effects of diffraction that arise from objects located further than the depth of field. For coherent imaging systems it is possible to undo the effects of diffraction, as demonstrated in many digital holographic imaging systems, since the complex

electrical field is precisely known [113], [114] using a linear filter. It can be shown that propagation in free space of the electric field located at a distance $\Delta z = z - f_0$ to the distance $z = f_0$ is given by [115]:

$$\tilde{U}(f_X, f_Y, z = f_0) = \tilde{U}(f_X, f_Y, z = f_0 + \Delta z) \exp\left(i2\pi \frac{\Delta z}{\lambda} \sqrt{1 - (\lambda f_X)^2 - (\lambda f_Y)^2}\right). \quad (7.2)$$

The effect of free space propagation in the spatial (x, y) Fourier domain is a spatial frequency dependent phase shift. Unlike a the low pass filter of the pupil, the information is not lost but rather multiplied by a known function with unity magnitude. To recover the original electric field profile, the appropriate phase mask can be digitally applied to the Fourier transform of the measured complex electric field. Typical digital holograms do not measure the exact depth of the of the reflector (Δz) with respect to the plane of focus. Reconstruction techniques must make assumptions about the content of the image and vary the refocused depth (Δz) until the “best” location is found.

This insight has also been applied to OCT imaging systems to image beyond the depth of field of the focusing optics [114]. Unfortunately, it is challenging to apply the same methodology in raster-scanned OCT systems because potentially large time delays may exist between adjacent points, limiting the phase stability of the image across the field of view [116]. If the phase of the measured signal across the image is not stable, then one cannot successfully refocus the image. In the case of swept source optical coherent tomography, the phase of the measured electric field is directly related to the starting optical frequency of the optical sweep and the precise location of the reference mirror and scatterer to within a fraction of the wavelength of light.

Figure 7.3 shows how a Siemens star appears when it is not located exactly at the focal length of the lens. For small deviations from the plane of focus, the radius where the bright and dark stripes of the Siemens are no longer visible gets slightly larger. For large deviations, the bright and dark stripes interchange periodically maintaining excellent contrast between the stripes. This indicates that the information for the reflector is now located in adjacent pixels instead as opposed to simply being lost. While the Siemens star still maintains its general appearance, more complicated shapes would become much harder to recognize.

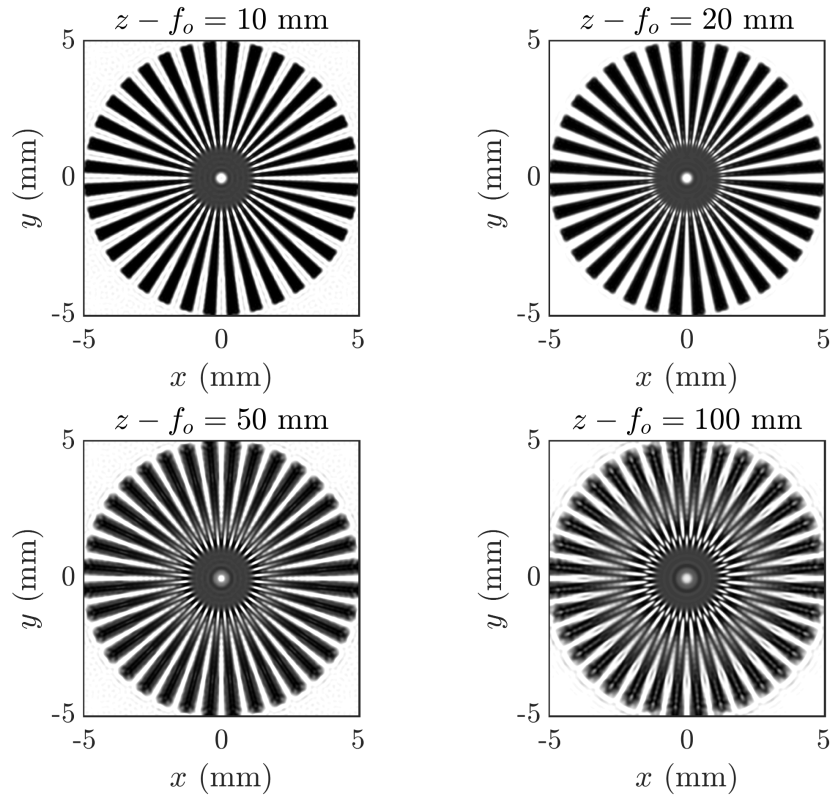


Figure 7.3: Simulated Siemens star as it would appear when imaged through a $4f$ system with cutoff frequency $f < 5 \text{ mm}^{-1}$ at different physical locations from the focal length of the object lens using light with a wavelength of $1 \mu\text{m}$.

7.2 Computationally refocusing images acquired with TomICam

The TomICam takes holographic images of the reflectivity by electronically changing the interrogated depth. Within the depth of field, the TomICam interrogates plane sections with constant distance z with width an axial resolution limited by the axial resolution of the swept laser as discussed in Section 6.2. Away from the depth of field, one needs to undo the effects of free space propagation to obtain meaningful images. Because the TomICam measures the depth of the reflector with certainty and simultaneously isolates the measured electric field from that of other depth locations, it is possible to reconstruct the original electric field in a single mathematical step. To reconstruct the original electric field profile, the appropriate phase mask can be applied computationally to the Fourier transform of the image.

$$U_r(\tilde{z}_{\text{mod}})(f_X, f_Y) = \tilde{U}(f_X, f_Y, \Delta z) \exp\left(-i2\pi \frac{z_{\text{mod}} - z_{\text{mod}0}}{\lambda} \sqrt{1 - (\lambda f_X)^2 - (\lambda f_Y)^2}\right), \quad (7.3)$$

Camera used	Lucam Lu075M
Pixel size at the image plane	48.1 μm
Laser central wavelength	1064 nm
Laser sweep bandwidth	190 GHz
Depth resolution in free space	785 μm
Lateral resolution	62 μm
Approximate depth of field	25 mm
Optical power in fiber	20 mW
Exposure time	2 ms
Frame rate (limited by USB2.0 speeds)	40 frames per second

Table 7.1: Summary of the parameters for the imaging system used in the subsequent experiments.

where z_{mod} refers to the interrogated depth as selected by the modulation frequency of the intensity modulator and $z_{\text{mod}0}$ is the interrogated depth for an image in-focus. The advantage of the TomICam over other forms of depth resolved microscopy is that the system acquires a hologram at a particular depth location in a small number (three to four frames) of successive frames limiting the stability requirement of the system.

7.3 Experimental results with a resolution target

We apply the reconstruction technique described above to the TomICam in Chapter 6.2 and quantify the performance by placing a USAF 1951 resolution target target in field of view of the imaged scene. The target is moved in and out of focus and a volumetric dataset is acquired every time the target is moved. The image obtained when the USAF 1951 resolution target is placed in focus is used to determine the resolution of the imaging system. This image is used to determine the distance relative to the reference mirror from the plane of focus ($z_{\text{mod}0}$).

All images shown reflect the intensity of the light received from a particular depth and normalized in order to remove the effects of the Gaussian illumination.

The properties of the imaging system are summarized in Table 7.1.

At the edge of the depth of field ($\Delta z = \pm 25$ mm), the resolution decreases by approximately a factor of $\sqrt{2}$ as illustrated in Figure 7.5. While the image has decreased in resolution, this is often considered acceptable in the sense that there is still enough information to obtain meaningful images with comparable lateral resolutions to an object located at the focal plane of the lens. When one applies the digital corrections described in the previous sections, the original resolution is

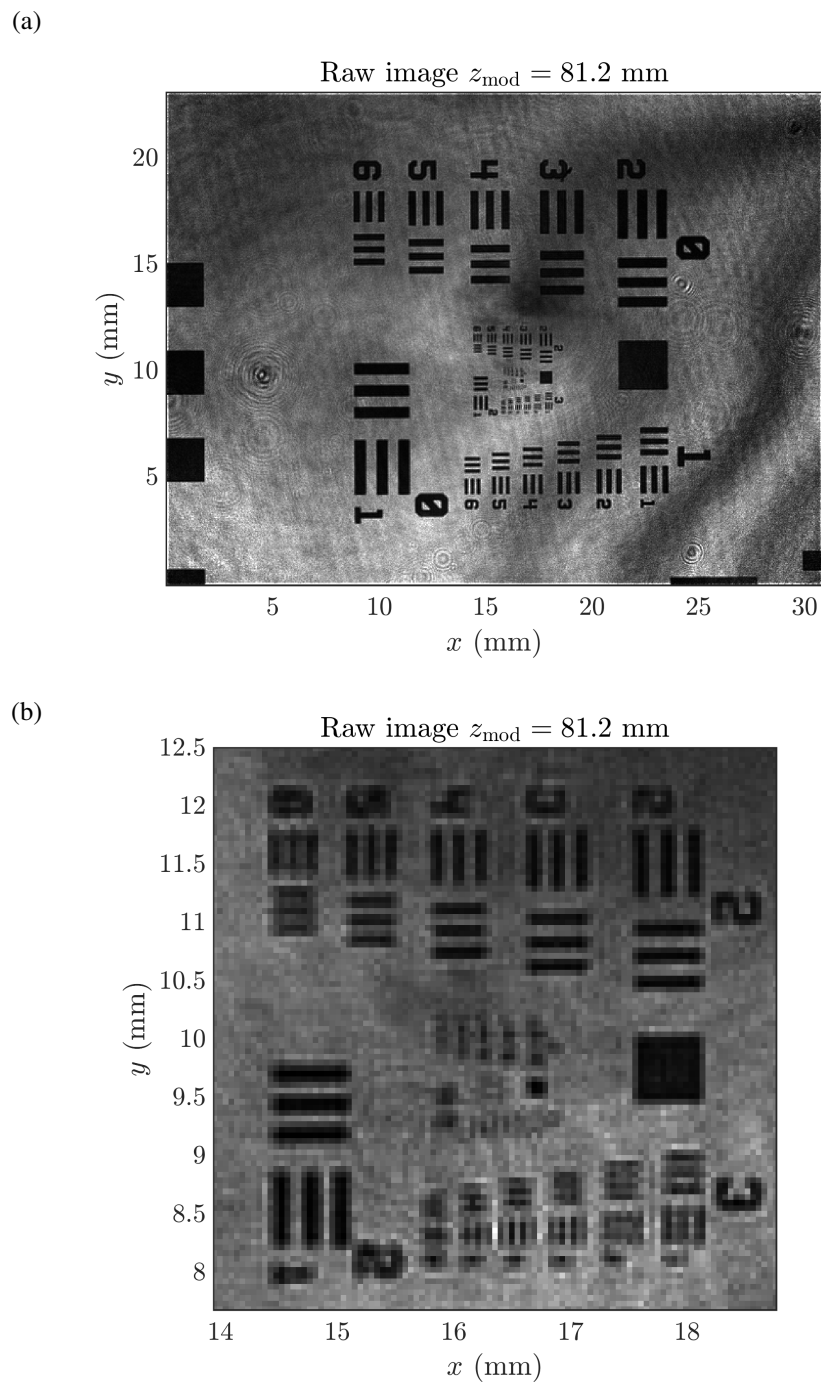


Figure 7.4: The depth slice corresponding to location of the USAF 1951 resolution target. The imaging system is determined to clearly resolve group number 3, element 1 corresponding to a resolution of $62 \mu\text{m}$. a) shows the full frame acquired by the camera (640×480 pixels). b) shows the region of interest near group elements 2 and 3 used to quantify the resolution of the system.

restored, as shown in Figure 7.6, for objects both in front and behind the plane of

the focus.

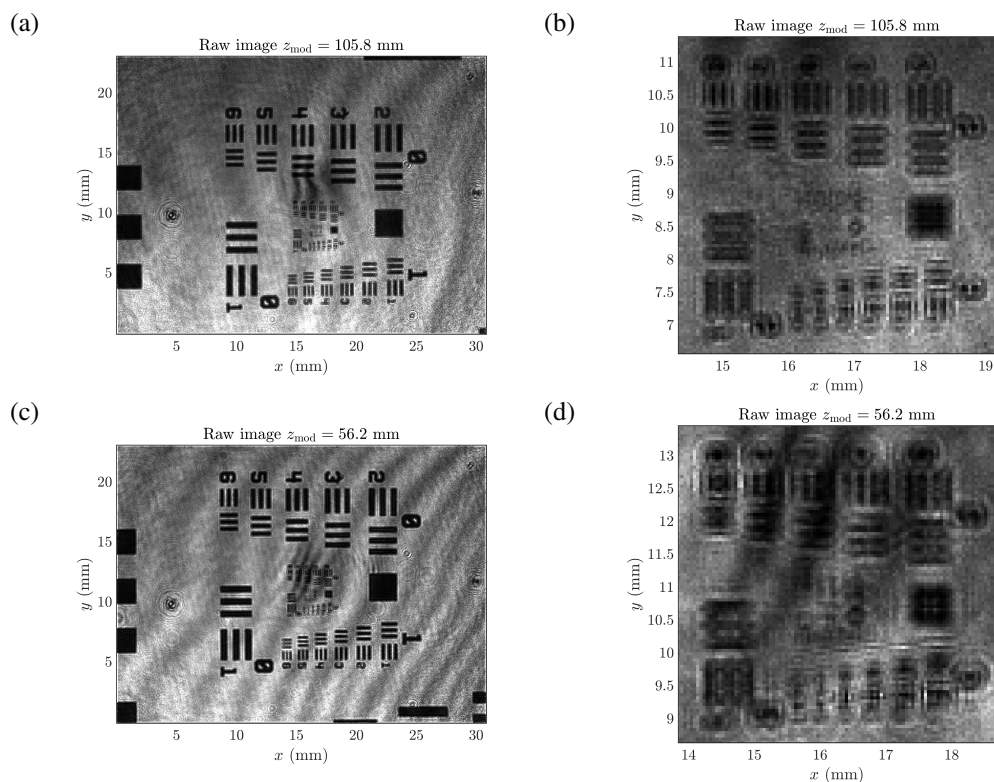


Figure 7.5: The depth slice corresponding where the USAF 1951 resolution is located when it is moved 25 mm toward the lens (a-b) and 25 mm away from the lens (c-d) with respect to the plane of focus.

This correction can be extended far beyond the depth of field. Figures 7.7(a-c) show the results of applying the digital refocusing technique when the target is placed between ± 50 mm and ± 168 mm away from the plane of focus. This demonstration shows that a six fold increase in the depth of field of the is possible by applying a filter to the measured field profile.

To explore the limit of digital we place the resolution, we placed the resolution target 383 mm away from the plane of focus of the imaging system. As shown in Figure 7.8, even more than $15\times$ away from original depth of field, digital reconstruction is able to adequately refocus the image and resolve many of the features of the resolution target.

7.4 Experimental results for retro-reflective polystyrene beads

To show the ability to refocus images in the presence of reflectors located at different depth locations, we show results from images obtained from a scene made of

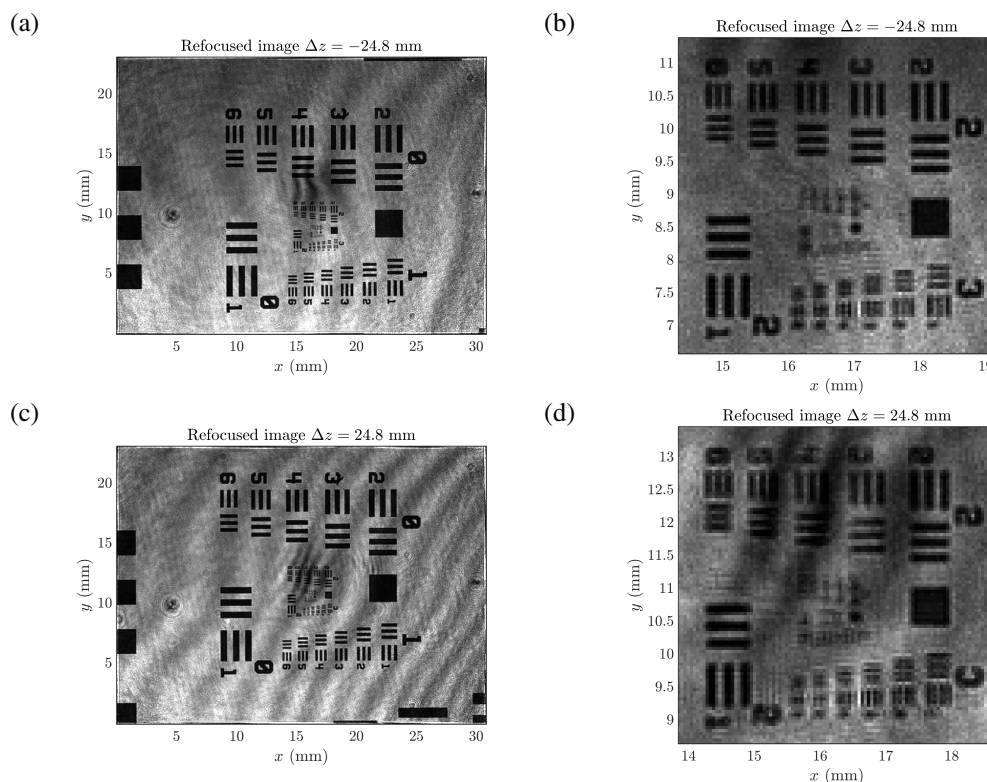


Figure 7.6: The depth slice corresponding to the location of the USAF 1951 resolution target is located when it is moved 25 mm toward the lens (a-b) and 25 mm away from the lens (c-d) with respect to the plane of focus after digital refocusing.

three letters written in retro-reflective polystyrene beads approximately $100\ \mu\text{m}$ in diameter placed on different glass slides. Two letters, *C* and *F* are placed within the depth of field, and the last letter *T* is placed at a location of 185 mm away from the plane of focus, much beyond the original depth of field. Figure 7.9 shows the imaged scene as it would be seen with coherent illumination. As expected, digital refocusing does little to improve the image quality for the two letters placed within the depth of the field of the imaging system, “*C*” and “*F*”. In contrast, the letter *T* is nearly unrecognizable without refocusing because it is located at a position $\approx 6\times$ away from the depth of field. After digital refocusing, a crisp *T* made of individual micro spheres is visible at a depth exactly 265.7 mm from the reference mirror, known to be exactly 184.7 mm away from the plane of focus.

7.5 3D imaging in bulk dielectric volumes

The previous discussion has so far assumed that the scatterers were embedded in free space, where the refractive index is unity. The same refocusing technique is also possible for reflectors embedded in a bulk medium where the refractive index

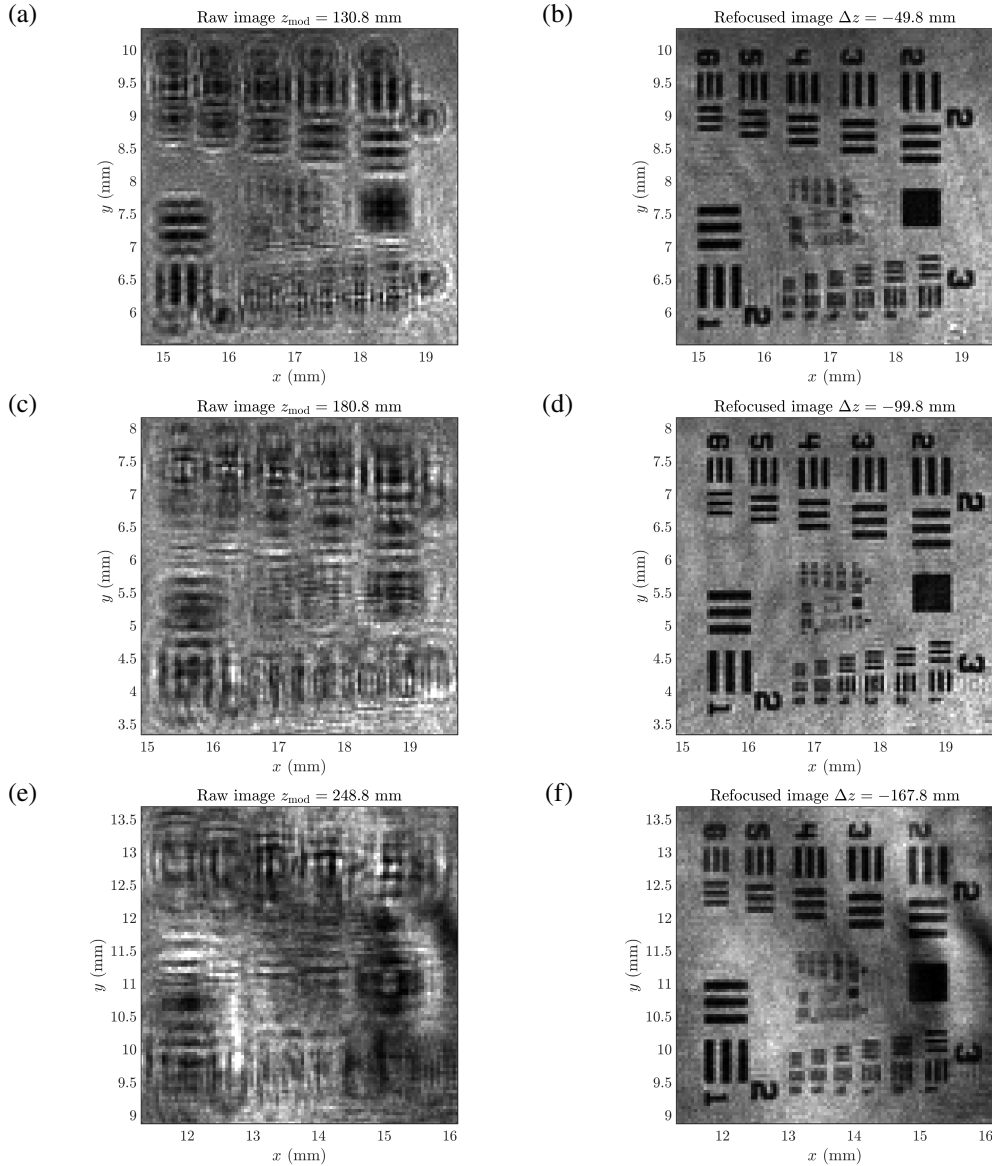


Figure 7.7: The region of interest for the depth slice corresponding to the USAF 1951 resolution target when it is placed 50 mm, 100 mm, and 168 mm away from the plane of focus. Measurements from the TomICam before (a, c, e) and after digital refocusing (b, d, f).

is not unity. This has particular importance for biological applications where the bulk index is closer to that of water, closer to 1.3 for many wavelengths of interest.

In this case, the propagation vector (k vector) is modified to include the refractive index of the bulk medium and becomes $k = 2\pi n_{\text{bulk}}/\lambda_0$, where λ_0 is the central

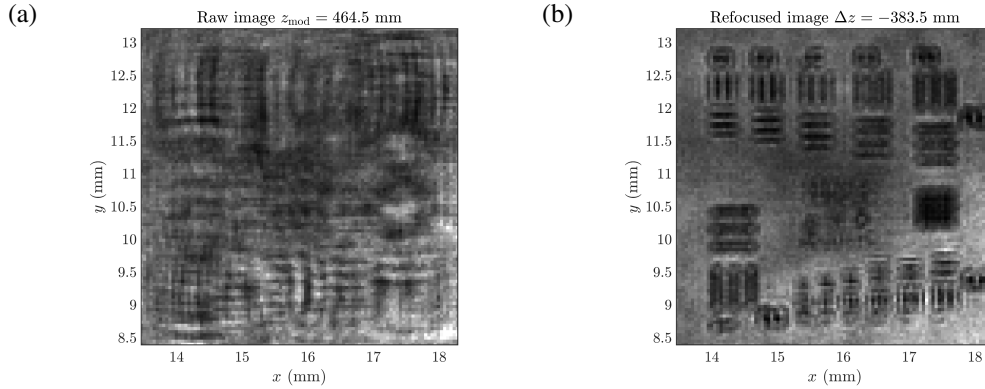


Figure 7.8: The region of interest for the depth slice corresponding to the USAF 1951 resolution target when it is placed 385 mm away from the plane of focus before (a) and after (b) digital refocusing.

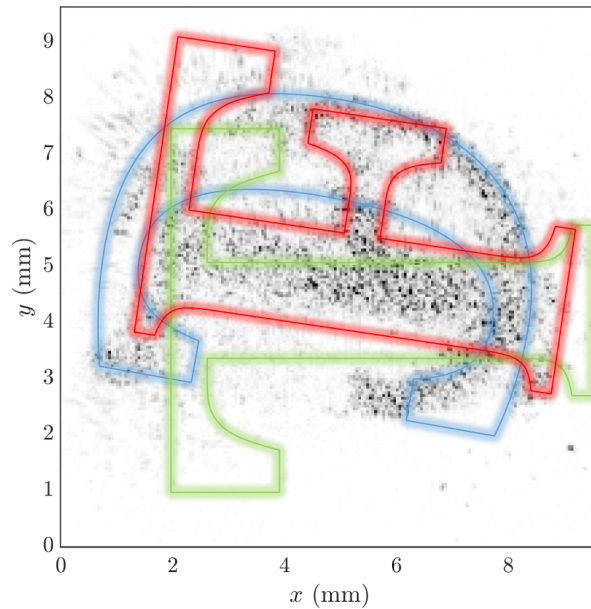


Figure 7.9: The imaged scene containing three letters “C”, “F” and “T”. The letters are located at different depths. Each letter is highlighted in a different color. With conventional illumination it is difficult to read the individual letters or to identify their depth.

wavelength of the laser in vacuum. Equation 7.2 becomes

$$\tilde{U}(f_X, f_Y, z = f_0) = \tilde{U}(f_X, f_Y, z = f_0 + \Delta z) \exp\left(ik_0\Delta zn_{\text{bulk}}\sqrt{1 - (\lambda f_X)^2 - (\lambda f_Y)^2}\right). \quad (7.4)$$

For a reflector Δz away from the plane of focus submerged in a bulk medium with refractive index n_{bulk} , the correction required is needs to be scaled by n_{bulk} .

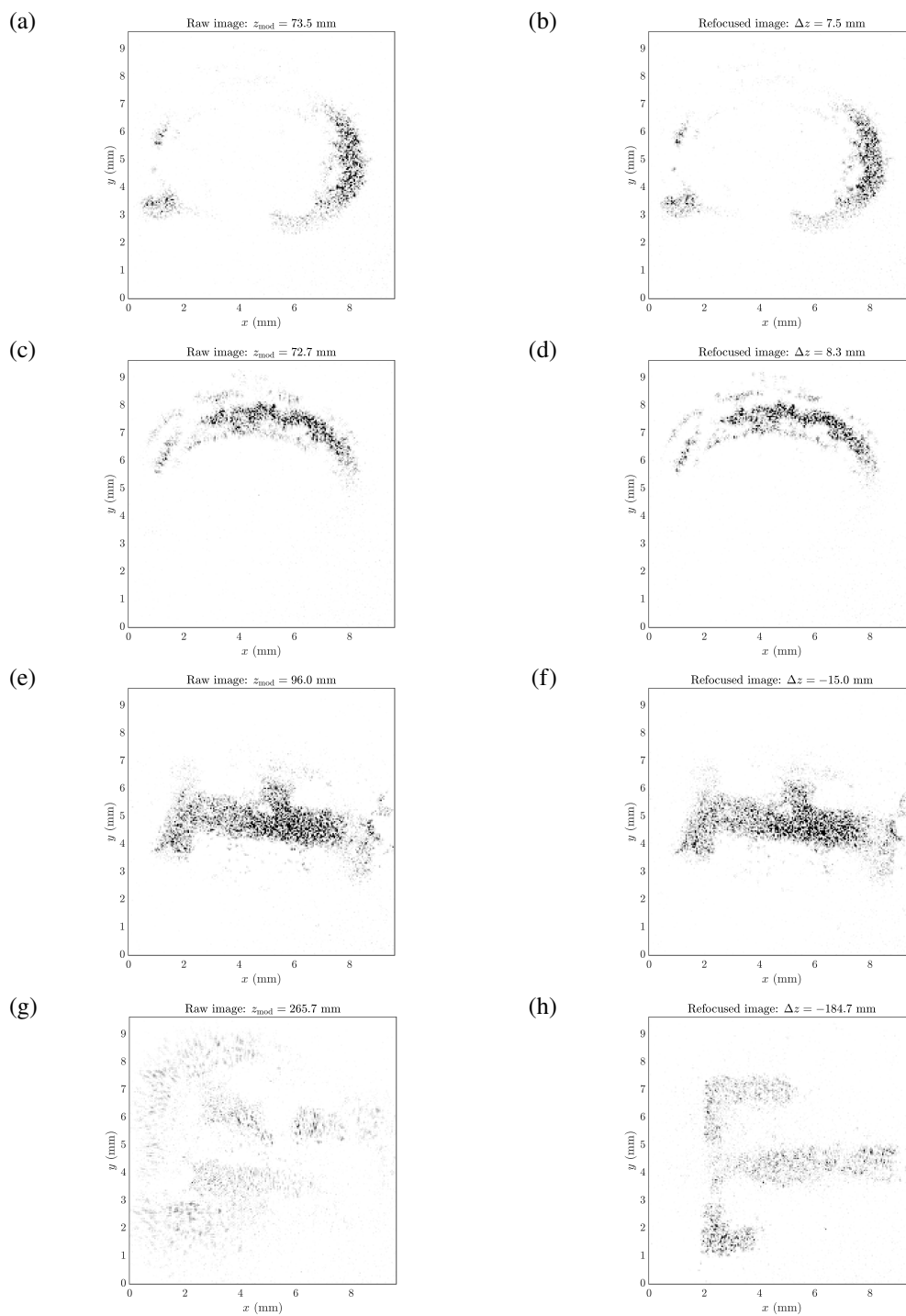


Figure 7.10: The individual tomograms acquired for the letters “C”, “F”, and “T”. (a, c, e, g) show the raw tomograms without digital refocusing for the relevant depths containing the three letters. (b, d, f, h) show the same images after computationally refocusing is applied.

Fortunately, the TomICam does not measure the physical distance but rather the optical path length τ between the reference mirror. Because the optical path length is directly proportional to the refractive index and the physical distance ($\tau \propto n_{\text{bulk}}\Delta z$), the refractive index does not need to be perfectly known to computationally refocus images that originate from reflectors beyond the depth of field. Imperfect knowledge will only manifest itself as an error in the absolute distance (in units of length) and not in the ability of the TomICam to laterally resolve the scatterers.

7.6 Conclusions

We have shown that TomICam is able to combine the knowledge of the measured phase in adjacent pixels with the knowledge of the exact location of the reflectors to extend the depth of field of the image. Back propagation through the use of a linear filter is used to refocus each slice to obtain a diffraction limited image. Using this technique, we are able to extend the depth of field of the tomographic imaging camera by more than a factor of 15 using a single computation step.

BIBLIOGRAPHY

- [1] M. Nakamura, K. Aiki, J. Umeda, and A. Yariv, “CW operation of distributed-feedback GaAs-GaAlAs diode lasers at temperatures up to 300 K,” *Applied Physics Letters*, vol. 27, no. 7, pp. 403–405, 1975. DOI: 10.1063/1.88492. eprint: <http://dx.doi.org/10.1063/1.88492>. [Online]. Available: <http://dx.doi.org/10.1063/1.88492>.
- [2] C. T. Santis, S. T. Steger, Y. Vilenchik, A. Vasilyev, and A. Yariv, “High-coherence semiconductor lasers based on integral high-q resonators in hybrid Si/III-V platforms,” *Proceedings of the National Academy of Sciences*, vol. 111, no. 8, pp. 2879–2884, 2014. DOI: 10.1073/pnas.1400184111. eprint: <http://www.pnas.org/content/111/8/2879.full.pdf>. [Online]. Available: <http://www.pnas.org/content/111/8/2879.abstract>.
- [3] C. T. Santis and A. Yariv, “The next high-coherence semiconductor lasers based on integral high-Q resonators in hybrid si/iii-v platforms,” *Arxiv?*,
- [4] S. T. Steger, “A fundamental approach to phase noise reduction in hybrid Si/III-V lasers,” Dissertation (Ph.D.) California Institute of Technology, 2014. [Online]. Available: <http://resolver.caltech.edu/CaltechTHESIS:05212014-113511509>.
- [5] R. Ramaswami, K. Sivarajan, and G. Sasak, *Optical Networks, A Practical Perspective*, 3rd ed. 30 Corporate Drive, Suite 400, Burlington, MA 01803, USA: Morgan Kaufmann, 2010.
- [6] A. Yariv and P. Yeh, *Photonics - Optical Electronics in Modern Communications*, 6th ed. Oxford, 2007.
- [7] D. Kim, P. Popescu, M. Harfouche, J. Sendowski, M.-E. Dimotsantou, R. C. Flagan, and A. Yariv, “On-chip integrated differential optical microring refractive index sensing platform based on a laminar flow scheme,” *Opt. Lett.*, vol. 40, no. 17, pp. 4106–4109, Sep. 2015. DOI: 10.1364/OL.40.004106. [Online]. Available: <http://ol.osa.org/abstract.cfm?URI=ol-40-17-4106>,
- [8] K. Predehl, G. Grosche, S. M. F. Raupach, S. Droste, O. Terra, J. Alnis, T. Legero, T. W. Hänsch, T. Udem, R. Holzwarth, and H. Schnatz, “A 920-kilometer optical fiber link for frequency metrology at the 19th decimal place,” *Science*, vol. 336, no. 6080, pp. 441–444, 2012, ISSN: 0036-8075. DOI: 10.1126/science.1218442. eprint: <http://science.sciencemag.org/content/336/6080/441.full.pdf>. [Online]. Available: <http://science.sciencemag.org/content/336/6080/441>.

- [9] M. Gabrysch, C. Corsi, F. Pavone, and M. Inguscio, "Simultaneous detection of CO and CO₂ using a semiconductor DFB diode laser at 1.578 μm ," *Applied Physics B*, vol. 65, no. 1, pp. 75–79, Jul. 1997, ISSN: 1432-0649. DOI: 10.1007/s003400050253. [Online]. Available: <https://doi.org/10.1007/s003400050253>.
- [10] S. B. Papp, K. Beha, P. Del'Haye, F. Quinlan, H. Lee, K. J. Vahala, and S. A. Diddams, "Microresonator frequency comb optical clock," *Optica*, vol. 1, no. 1, pp. 10–14, Jul. 2014. DOI: 10.1364/OPTICA.1.000010. [Online]. Available: <http://www.osapublishing.org/optica/abstract.cfm?URI=optica-1-1-10>.
- [11] P. Evans, M. Fisher, R. Malendevich, A. James, G. Goldfarb, T. Vallaitis, M. Kato, P. Samra, S. Corzine, E. Strzelecka, P. Studenkov, R. Salvatore, F. Sedgwick, M. Kuntz, V. Lal, D. Lambert, A. Dentai, D. Pavinski, J. Zhang, J. Cornelius, T. Tsai, B. Behnia, J. Bostak, V. Dominic, A. Nilsson, B. Taylor, J. Rahn, S. Sanders, H. Sun, K.-T. Wu, J. Pleumeekers, R. Muthiah, M. Missey, R. Schneider, J. Stewart, M. Reffle, T. Butrie, R. Nagarajan, M. Ziari, F. Kish, and D. Welch, "1.12 Tb/s superchannel coherent PM-QPSK InP transmitter photonic integrated circuit (PIC)," *Opt. Express*, vol. 19, no. 26, B154–B158, Dec. 2011. DOI: 10.1364/OE.19.00B154. [Online]. Available: <http://www.opticsexpress.org/abstract.cfm?URI=oe-19-26-B154>.
- [12] U. Atsushi, A. Kazuya, I. Masaki, H. Kunihiro, N. Sunao, S. Hiroyuki, O. Isao, K. Takayuki, S. Masaru, Y. Shigeru, Y. Kazuyuki, and D. Peter, "Fast physical random bit generation with chaotic semiconductor lasers," *Nat Photon*, vol. 2, no. 12, pp. 728–732, Dec. 2008, ISSN: 1749-4885. DOI: 10.1038/nphoton.2008.227. [Online]. Available: <http://dx.doi.org/10.1038/nphoton.2008.227>.
- [13] A. Vasilyev, N. Satyan, S. Xu, G. Rakuljic, and A. Yariv, "Multiple source frequency-modulated continuous-wave optical reflectometry: Theory and experiment," *Appl. Opt.*, vol. 49, no. 10, pp. 1932–1937, Apr. 2010. DOI: 10.1364/AO.49.001932. [Online]. Available: <http://ao.osa.org/abstract.cfm?URI=ao-49-10-1932>.
- [14] J. X. Cai, H. Zhang, H. G. Batshon, M. Mazurczyk, O. V. Sinkin, D. G. Foursa, A. N. Pilipetskii, G. Mohs, and N. S. Bergano, "200 Gb/s and Dual Wavelength 400 Gb/s Transmission over Transpacific Distance at 6.0 b/s/Hz Spectral Efficiency," *Journal of Lightwave Technology*, vol. 32, no. 4, pp. 832–839, Feb. 2014, ISSN: 0733-8724. DOI: 10.1109/JLT.2013.2284669.
- [15] J. Proakis and M. Salehi, *Digital Communications*, 5th ed. McGraw-Hill Education, Nov. 2007.

- [16] A. L. Schawlow and C. H. Townes, "Infrared and optical masers," *Phys. Rev.*, vol. 112, pp. 1940–1949, 6 Dec. 1958. DOI: 10.1103/PhysRev.112.1940. [Online]. Available: <https://link.aps.org/doi/10.1103/PhysRev.112.1940>.
- [17] C. Henry, "Theory of the linewidth of semiconductor lasers," *IEEE Journal of Quantum Electronics*, vol. 18, no. 2, pp. 259–264, Feb. 1982, ISSN: 0018-9197. DOI: 10.1109/JQE.1982.1071522.
- [18] Cisco, "Cisco global cloud index: Forecast and methodology, 2015-2000," 2016. [Online]. Available: <https://www.cisco.com/c/dam/en/us/solutions/collateral/service-provider/global-cloud-index-gci/white-paper-c11-738085.pdf>.
- [19] H. Liu, C. F. Lam, and C. Johnson, "Scaling optical interconnects in data-center networks opportunities and challenges for WDM," in *2010 18th IEEE Symposium on High Performance Interconnects*, Aug. 2010, pp. 113–116. DOI: 10.1109/HOTI.2010.15.
- [20] K. i. Sato, H. Hasegawa, T. Niwa, and T. Watanabe, "A large-scale wavelength routing optical switch for data center networks," *IEEE Communications Magazine*, vol. 51, no. 9, pp. 46–52, Sep. 2013, ISSN: 0163-6804. DOI: 10.1109/MCOM.2013.6588649.
- [21] K. Petermann, *Laser Diode Modulation and Noise*. Dordrecht: Springer Netherlands, 1988. DOI: 10.1007/978-94-009-2907-4_1. [Online]. Available: http://dx.doi.org/10.1007/978-94-009-2907-4_1.
- [22] E. M. Strzelecki, D. A. Cohen, and L. A. Coldren, "Investigation of tunable single frequency diode lasers for sensor applications," *Journal of Lightwave Technology*, vol. 6, no. 10, pp. 1610–1618, Oct. 1988, ISSN: 0733-8724. DOI: 10.1109/50.7923.
- [23] A. Fercher, C. Hitzenberger, G. Kamp, and S. El-Zaiat, "Measurement of intraocular distances by backscattering spectral interferometry," *Optics Communications*, vol. 117, no. 1, pp. 43–48, 1995, ISSN: 0030-4018. DOI: [http://dx.doi.org/10.1016/0030-4018\(95\)00119-S](http://dx.doi.org/10.1016/0030-4018(95)00119-S). [Online]. Available: <http://www.sciencedirect.com/science/article/pii/S003040189500119S>.
- [24] M. A. Choma, M. V. Sarunic, C. Yang, and J. A. Izatt, "Sensitivity advantage of swept source and fourier domain optical coherence tomography," *Opt. Express*, vol. 11, no. 18, pp. 2183–2189, Sep. 2003. DOI: 10.1364/OE.11.002183. [Online]. Available: <http://www.opticsexpress.org/abstract.cfm?URI=oe-11-18-2183>.
- [25] M. C. Y. Huang, K. B. Cheng, Y. Zhou, A. P. Pisano, and C. J. Chang-Hasnain, "Monolithic integrated piezoelectric MEMS-tunable VCSEL," *IEEE Journal of Selected Topics in Quantum Electronics*, vol. 13, no. 2,

- pp. 374–380, Mar. 2007, ISSN: 1077-260X. DOI: 10.1109/JSTQE.2007.894056.
- [26] D. D. John, C. B. Burgner, B. Potsaid, M. E. Robertson, B. K. Lee, W. J. Choi, A. E. Cable, J. G. Fujimoto, and V. Jayaraman, “Wideband electrically pumped 1050-nm MEMS-tunable VCSEL for ophthalmic imaging,” *J. Lightwave Technol.*, vol. 33, no. 16, pp. 3461–3468, Aug. 2015. [Online]. Available: <http://jlt.osa.org/abstract.cfm?URI=jlt-33-16-3461>.
- [27] J. O. White, M. Harfouche, J. Edgecumbe, N. Satyan, G. Rakuljic, V. Jayaraman, C. Burgner, and A. Yariv, “1.6 kW Yb fiber amplifier using chirped seed amplification for stimulated Brillouin scattering suppression,” *Appl. Opt.*, vol. 56, no. 3, B116–B122, Jan. 2017. DOI: 10.1364/AO.56.00B116. [Online]. Available: <http://ao.osa.org/abstract.cfm?URI=ao-56-3-B116>,
- [28] I. Grulkowski, J. J. Liu, B. Potsaid, V. Jayaraman, J. Jiang, J. G. Fujimoto, and A. E. Cable, “High-precision, high-accuracy ultralong-range swept-source optical coherence tomography using vertical cavity surface emitting laser light source,” *Opt. Lett.*, vol. 38, no. 5, pp. 673–675, Mar. 2013. DOI: 10.1364/OL.38.000673. [Online]. Available: <http://ol.osa.org/abstract.cfm?URI=ol-38-5-673>.
- [29] G. Liu and Z. Chen, “Capturing the vital vascular fingerprint with optical coherence tomography,” *Appl. Opt.*, vol. 52, no. 22, pp. 5473–5477, Aug. 2013. DOI: 10.1364/AO.52.005473. [Online]. Available: <http://ao.osa.org/abstract.cfm?URI=ao-52-22-5473>.
- [30] S. H. Yun, G. J. Tearney, B. J. Vakoc, M. Shishkov, W. Y. Oh, A. E. Desjardins, M. J. Suter, R. C. Chan, J. A. Evans, I.-K. Jang, N. S. Nishioka, J. F. de Boer, and B. E. Bouma, “Comprehensive volumetric optical microscopy in vivo,” *Nat Med*, vol. 12, pp. 1429–1433, 12 Dec. 2006. [Online]. Available: <http://dx.doi.org/10.1038/nm1450>.
- [31] R. Motaghiannezam and S. Fraser, “In vivo human retinal and choroidal vasculature visualization using differential phase contrast swept source optical coherence tomography at 1060 nm,” pp. 821 304–7, 2012. DOI: 10.1117/12.910991. [Online]. Available: <http://dx.doi.org/10.1117/12.910991>.
- [32] Y. Shimada, A. Sadr, Y. Sumi, and J. Tagami, “Application of Optical Coherence Tomography (OCT) for Diagnosis of Caries, Cracks, and Defects of Restorations,” *Current Oral Health Reports*, vol. 2, no. 2, pp. 73–80, Jun. 2015, ISSN: 2196-3002. DOI: 10.1007/s40496-015-0045-z. [Online]. Available: <http://dx.doi.org/10.1007/s40496-015-0045-z>.

- [33] P. Gong, R. A. McLaughlin, Y. M. Liew, P. R. T. Munro, F. M. Wood, and D. D. Sampson, "Assessment of human burn scars with optical coherence tomography by imaging the attenuation coefficient of tissue after vascular masking," *Journal of Biomedical Optics*, vol. 19, no. 2, pp. 021 111–021 111, 2013. DOI: 10.1117/1.JBO.19.2.021111. [Online]. Available: <http://dx.doi.org/10.1117/1.JBO.19.2.021111>.
- [34] G. Morthier, K. David, P. Vankwikelberge, and R. Baets, "A new DFB-laser diode with reduced spatial hole burning," *IEEE Photonics Technology Letters*, vol. 2, pp. 388–390, Jun. 1990. DOI: 10.1109/68.56595.
- [35] H. J. Wunsche, U. Bandelow, and H. Wenzel, "Calculation of combined lateral and longitudinal spatial hole burning in $\lambda/4$ shifted DFB lasers," *IEEE Journal of Quantum Electronics*, vol. 29, no. 6, pp. 1751–1760, Jun. 1993, ISSN: 0018-9197.
- [36] K. P. Yap, A. Delage, J. Lapointe, B. Lamontagne, J. H. Schmid, P. Waldron, B. A. Syrett, and S. Janz, "Correlation of scattering loss, sidewall roughness and waveguide width in silicon-on-insulator (SOI) ridge waveguides," *Journal of Lightwave Technology*, vol. 27, no. 18, pp. 3999–4008, Sep. 2009, ISSN: 0733-8724. DOI: 10.1109/JLT.2009.2021562.
- [37] Y. Akahane, T. Asano, B.-S. Song, and S. Noda, "Fine-tuned high-Q photonic-crystal nanocavity," *Opt. Express*, vol. 13, no. 4, pp. 1202–1214, Feb. 2005. DOI: 10.1364/OPEX.13.001202. [Online]. Available: <http://www.opticsexpress.org/abstract.cfm?URI=oe-13-4-1202>.
- [38] W. Walukiewicz, J. Lagowski, L. Jastrzebski, P. Rava, M. Lichtensteiger, C. H. Gatos, and H. C. Gatos, "Electron mobility and free-carrier absorption in InP; determination of the compensation ratio," *Journal of Applied Physics*, vol. 51, no. 5, pp. 2659–2668, 1980. DOI: 10.1063/1.327925. eprint: <http://aip.scitation.org/doi/pdf/10.1063/1.327925>. [Online]. Available: <http://aip.scitation.org/doi/abs/10.1063/1.327925>.
- [39] C. T. Santis, "High-coherence hybrid Si/III-V semiconductor lasers," Dissertation (Ph.D.) California Institute of Technology, 2013. [Online]. Available: <http://resolver.caltech.edu/CaltechTHESIS:05312013-151934307>.
- [40] Y. Vilenchik, "Narrow-linewidth Si/III-V lasers: A study of laser dynamics and nonlinear effects," Dissertation (Ph.D.) California Institute of Technology, 2015. [Online]. Available: <http://resolver.caltech.edu/CaltechTHESIS:06042015-232226135>.
- [41] C. Santis and A. Yariv, "High-Q silicon resonators for high-coherence hybrid Si/III-V semiconductor lasers," in *CLEO: 2015*, Optical Society of America, 2015, SW3F.6. DOI: 10.1364/CLEO_SI.2015.SW3F.6. [On-

- line]. Available: http://www.osapublishing.org/abstract.cfm?URI=CLEO_SI-2015-SW3F.6.
- [42] C. Santis, Y. Vilenchik, A. Yariv, N. Satyan, and G. Rakuljic, “Sub-kHz quantum linewidth semiconductor laser on silicon chip,” in *CLEO: 2015 Postdeadline Paper Digest*, Optical Society of America, 2015, JTh5A.7. DOI: 10.1364/CLEO_AT.2015.JTh5A.7. [Online]. Available: http://www.osapublishing.org/abstract.cfm?URI=CLEO_AT-2015-JTh5A.7.
- [43] A. W. Fang, H. Park, O. Cohen, R. Jones, M. J. Paniccia, and J. E. Bowers, “Electrically pumped hybrid AlGaInAs-silicon evanescent laser,” *Opt. Express*, vol. 14, no. 20, pp. 9203–9210, Oct. 2006. DOI: 10.1364/OE.14.009203. [Online]. Available: <http://www.opticsexpress.org/abstract.cfm?URI=oe-14-20-9203>.
- [44] G. Morthier, T. Spuesens, P. Mechet, G. Roelkens, and D. V. Thourhout, “InP microdisk lasers integrated on Si for optical interconnects,” *IEEE Journal of Selected Topics in Quantum Electronics*, vol. 21, no. 6, pp. 359–368, Nov. 2015, ISSN: 1077-260X. DOI: 10.1109/JSTQE.2014.2376697.
- [45] H.-H. Chang, A. W. Fang, M. N. Sysak, H. Park, R. Jones, O. Cohen, O. Raday, M. J. Paniccia, and J. E. Bowers, “1310nm silicon evanescent laser,” *Opt. Express*, vol. 15, no. 18, pp. 11 466–11 471, Sep. 2007. DOI: 10.1364/OE.15.011466. [Online]. Available: <http://www.opticsexpress.org/abstract.cfm?URI=oe-15-18-11466>.
- [46] S. Stankovic, R. Jones, M. N. Sysak, J. M. Heck, G. Roelkens, and D. V. Thourhout, “1310-nm hybrid III-V/Si fabry-perot laser based on adhesive bonding,” *IEEE Photonics Technology Letters*, vol. 23, no. 23, pp. 1781–1783, Dec. 2011, ISSN: 1041-1135. DOI: 10.1109/LPT.2011.2169397.
- [47] C. Ma, W. D. Sacher, Z. Tang, J. C. Mikkelsen, Y. Yang, F. Xu, T. Thiessen, H.-K. Lo, and J. K. S. Poon, “Silicon photonic transmitter for polarization-encoded quantum key distribution,” *Optica*, vol. 3, no. 11, pp. 1274–1278, Nov. 2016. DOI: 10.1364/OPTICA.3.001274. [Online]. Available: <http://www.osapublishing.org/optica/abstract.cfm?URI=optica-3-11-1274>.
- [48] G. Kim, J. W. Park, I. G. Kim, S. Kim, S. Kim, J. M. Lee, G. S. Park, J. Joo, K.-S. Jang, J. H. Oh, S. A. Kim, J. H. Kim, J. Y. Lee, J. M. Park, D.-W. Kim, D.-K. Jeong, M.-S. Hwang, J.-K. Kim, K.-S. Park, H.-K. Chi, H.-C. Kim, D.-W. Kim, and M. H. Cho, “Low-voltage high-performance silicon photonic devices and photonic integrated circuits operating up to 30 Gb/s,” *Opt. Express*, vol. 19, no. 27, pp. 26 936–26 947, Dec. 2011. DOI: 10.1364/OE.19.026936. [Online]. Available: <http://www.opticsexpress.org/abstract.cfm?URI=oe-19-27-26936>.

- [49] J. C. Hulme, J. K. Doylend, and J. E. Bowers, “Widely tunable Vernier ring laser on hybrid silicon,” *Opt. Express*, vol. 21, no. 17, pp. 19 718–19 722, Aug. 2013. DOI: 10.1364/OE.21.019718. [Online]. Available: <http://www.opticsexpress.org/abstract.cfm?URI=oe-21-17-19718>.
- [50] X. Sun and A. Yariv, “Engineering supermode silicon/III-V hybrid waveguides for laser oscillation,” *J. Opt. Soc. Am. B*, vol. 25, no. 6, pp. 923–926, Jun. 2008. DOI: 10.1364/JOSAB.25.000923. [Online]. Available: <http://josab.osa.org/abstract.cfm?URI=josab-25-6-923>.
- [51] K. Vahala and A. Yariv, “Semiclassical theory of noise in semiconductor lasers - part ii,” *IEEE Journal of Quantum Electronics*, vol. 19, no. 6, pp. 1102–1109, Jun. 1983, ISSN: 0018-9197. DOI: 10.1109/JQE.1983.1071984.
- [52] ———, “Semiclassical theory of noise in semiconductor lasers - part i,” *IEEE Journal of Quantum Electronics*, vol. 19, no. 6, pp. 1096–1101, Jun. 1983, ISSN: 0018-9197. DOI: 10.1109/JQE.1983.1071986.
- [53] J. Ahn, M. Fiorentino, R. G. Beausoleil, N. Binkert, A. Davis, D. Fattal, N. P. Jouppi, M. McLaren, C. M. Santori, R. S. Schreiber, S. M. Spillane, D. Vantrease, and Q. Xu, “Devices and architectures for photonic chip-scale integration,” *Applied Physics A*, vol. 95, no. 4, pp. 989–997, Jun. 2009, ISSN: 1432-0630. DOI: 10.1007/s00339-009-5109-2. [Online]. Available: <https://doi.org/10.1007/s00339-009-5109-2>.
- [54] T. Barwicz, Y. Taira, T. W. Lichoulas, N. Boyer, Y. Martin, H. Numata, J. W. Nah, S. Takenobu, A. Janta-Polczynski, E. L. Kimbrell, R. Leidy, M. H. Khater, S. Kamapurkar, S. Engelmann, Y. A. Vlasov, and P. Fortier, “A novel approach to photonic packaging leveraging existing high-throughput microelectronic facilities,” *IEEE Journal of Selected Topics in Quantum Electronics*, vol. 22, no. 6, pp. 455–466, Nov. 2016, ISSN: 1077-260X. DOI: 10.1109/JSTQE.2016.2593637.
- [55] L. A. Coldren, S. W. Corzine, and M. L. Mašanović, “Photonic integrated circuits,” in *Diode Lasers and Photonic Integrated Circuits*. John Wiley and Sons, Inc., 2012, pp. 451–507. DOI: 10.1002/9781118148167.ch8. [Online]. Available: <http://dx.doi.org/10.1002/9781118148167.ch8>.
- [56] O. B. Shchekin and D. G. Deppe, “1.3 μm InAs quantum dot laser with $T_0=161$ K from 0 to 80 $^{\circ}\text{C}$,” *Applied Physics Letters*, vol. 80, no. 18, pp. 3277–3279, 2002. DOI: 10.1063/1.1476708. eprint: <http://dx.doi.org/10.1063/1.1476708>. [Online]. Available: <http://dx.doi.org/10.1063/1.1476708>.
- [57] A. Matsumoto, K. Akahane, T. Umezawa, and N. Yamamoto, “Extremely stable temperature characteristics of 1550-nm band, p-doped, highly stacked quantum-dot laser diodes,” *Japanese Journal of Applied Physics*, vol. 56,

- no. 4S, 04CH07, 2017. [Online]. Available: <http://stacks.iop.org/1347-4065/56/i=4S/a=04CH07>.
- [58] C. Edge, R. M. Ash, C. G. Jones, and M. J. Goodwin, "Flip-chip solder bond mounting of laser diodes," *Electronics Letters*, vol. 27, no. 6, pp. 499–501, Mar. 1991, ISSN: 0013-5194. DOI: 10.1049/el:19910314.
- [59] C. Zhang, D. Liang, G. Kurczveil, J. E. Bowers, and R. G. Beausoleil, "High temperature hybrid silicon micro-ring lasers with thermal shunts," in *2015 Conference on Lasers and Electro-Optics (CLEO)*, May 2015, pp. 1–2. DOI: 10.1364/CLEO_SI.2015.SW3F.5.
- [60] "Indium phosphide (InP), hole mobility," in *Group IV Elements, IV-IV and III-V Compounds. Part b - Electronic, Transport, Optical and Other Properties*, O. Madelung, U. Rössler, and M. Schulz, Eds. Berlin, Heidelberg: Springer Berlin Heidelberg, 2002, pp. 1–6. DOI: 10.1007/10832182_307. [Online]. Available: http://dx.doi.org/10.1007/10832182_307.
- [61] *Applied thin-film products*, 2017. [Online]. Available: <https://www.thinfilm.com/tables.html>.
- [62] S. Adachi, "Lattice thermal resistivity of III–V compound alloys," *Journal of Applied Physics*, vol. 54, no. 4, pp. 1844–1848, 1983. DOI: 10.1063/1.332820. eprint: <http://dx.doi.org/10.1063/1.332820>. [Online]. Available: <http://dx.doi.org/10.1063/1.332820>.
- [63] S. Zhu and G.-Q. Lo, "Vertically stacked multilayer photonics on bulk silicon toward three-dimensional integration," *J. Lightwave Technol.*, vol. 34, no. 2, pp. 386–392, Jan. 2016. [Online]. Available: <http://jlt.osa.org/abstract.cfm?URI=jlt-34-2-386>.
- [64] A. Biberman, K. Preston, G. Hendry, N. Sherwood-Droz, J. Chan, J. S. Levy, M. Lipson, and K. Bergman, "Photonic network-on-chip architectures using multilayer deposited silicon materials for high-performance chip multiprocessors," *J. Emerg. Technol. Comput. Syst.*, vol. 7, no. 2, 7:1–7:25, Jul. 2011, ISSN: 1550-4832. DOI: 10.1145/1970406.1970409. [Online]. Available: <http://doi.acm.org/10.1145/1970406.1970409>.
- [65] N. Sherwood-Droz and M. Lipson, "Multi-layer low-temperature deposited cmos photonics for microelectronics backend integration," in *CLEO: 2011 - Laser Science to Photonic Applications*, May 2011, pp. 1–2. DOI: 10.1364/CLEO_SI.2011.CFB2.
- [66] P. Koonath and B. Jalali, "Multilayer 3-D photonics in silicon," *Opt. Express*, vol. 15, no. 20, pp. 12 686–12 691, Oct. 2007. DOI: 10.1364/OE.15.012686. [Online]. Available: <http://www.opticsexpress.org/abstract.cfm?URI=oe-15-20-12686>.

- [67] J. Kang, Y. Atsumi, M. Oda, T. Amemiya, N. Nishiyama, and S. Arai, "Low-loss amorphous silicon multilayer waveguides vertically stacked on silicon-on-insulator substrate," *Japanese Journal of Applied Physics*, vol. 50, no. 12R, p. 120 208, 2011. [Online]. Available: <http://stacks.iop.org/1347-4065/50/i=12R/a=120208>.
- [68] F. G. D. Corte, M. E. Montefusco, L. Moretti, I. Rendina, and G. Cocorullo, "Temperature dependence analysis of the thermo-optic effect in silicon by single and double oscillator models," *Journal of Applied Physics*, vol. 88, no. 12, pp. 7115–7119, 2000. DOI: 10.1063/1.1328062. eprint: <http://dx.doi.org/10.1063/1.1328062>. [Online]. Available: <http://dx.doi.org/10.1063/1.1328062>.
- [69] I. Corporation, *Gold-tin: The unique eutectic solder alloy*, 2005. [Online]. Available: <http://documents.indium.com/qdynamo/download.php?docid=2103>.
- [70] F. Favre, "Theoretical analysis of external optical feedback on DFB semiconductor lasers," *IEEE Journal of Quantum Electronics*, vol. 23, no. 1, pp. 81–88, Jan. 1987, ISSN: 0018-9197. DOI: 10.1109/JQE.1987.1073195.
- [71] F. Grillot, B. Thedrez, and G.-H. Duan, "Feedback sensitivity and coherence collapse threshold of semiconductor DFB lasers with complex structures," *IEEE Journal of Quantum Electronics*, vol. 40, no. 3, pp. 231–240, Mar. 2004, ISSN: 0018-9197. DOI: 10.1109/JQE.2003.823031.
- [72] F. Grillot, B. Thedrez, O. Gauthier-Lafaye, M. F. Martineau, V. Voiriot, J. L. Lafrayette, J. L. Gentner, and L. Silvestre, "Coherence-collapse threshold of 1.3 um semiconductor dfb lasers," *IEEE Photonics Technology Letters*, vol. 15, no. 1, pp. 9–11, Jan. 2003, ISSN: 1041-1135. DOI: 10.1109/LPT.2002.805771.
- [73] S. Azouigui *et al.*, "Coherence collapse and low-frequency fluctuations in quantum-dash based lasers emitting at 1.57 um," *Opt. Express*, vol. 15, no. 21, pp. 14 155–14 162, Oct. 2007. DOI: 10.1364/OE.15.014155. [Online]. Available: <http://www.opticsexpress.org/abstract.cfm?URI=oe-15-21-14155>.
- [74] L. Bi, J. Hu, P. Jiang, D. H. Kim, G. F. Dionne, L. C. Kimerling, and R. A., "On-chip optical isolation in monolithically integrated non-reciprocal optical resonators," *Nat Photon*, vol. 5, no. 12, pp. 758–762, Dec. 2011, ISSN: 1749-4885. DOI: 10.1038/nphoton.2011.270. [Online]. Available: <http://dx.doi.org/10.1038/nphoton.2011.270>.
- [75] B. J. H. Stadler and T. Mizumoto, "Integrated magneto-optical materials and isolators: A review," *IEEE Photonics Journal*, vol. 6, no. 1, pp. 1–15, Feb. 2014, ISSN: 1943-0655. DOI: 10.1109/JPHOT.2013.2293618.

- [76] M. Sorel, G. Giuliani, A. Scire, R. Miglierina, S. Donati, and P. J. R. Laybourn, "Operating regimes of GaAs-AlGaAs semiconductor ring lasers: Experiment and model," *IEEE Journal of Quantum Electronics*, vol. 39, no. 10, pp. 1187–1195, Oct. 2003, ISSN: 0018-9197. DOI: 10.1109/JQE.2003.817585.
- [77] R. Tkach and A. Chraplyvy, "Regimes of feedback effects in 1.5 um distributed feedback lasers," *Journal of Lightwave Technology*, vol. 4, no. 11, pp. 1655–1661, Nov. 1986, ISSN: 0733-8724. DOI: 10.1109/JLT.1986.1074666.
- [78] R. Schatz, "Longitudinal spatial instability in symmetric semiconductor lasers due to spatial hole burning," *IEEE Journal of Quantum Electronics*, vol. 28, no. 6, pp. 1443–1449, Jun. 1992, ISSN: 0018-9197. DOI: 10.1109/3.135296.
- [79] K. Vahala, L. C. Chiu, S. Margalit, and A. Yariv, "On the linewidth enhancement factor alpha in semiconductor injection lasers," *Applied Physics Letters*, vol. 42, no. 8, pp. 631–633, 1983. DOI: 10.1063/1.94054. eprint: <http://dx.doi.org/10.1063/1.94054>. [Online]. Available: <http://dx.doi.org/10.1063/1.94054>.
- [80] M.-C. Amann, T. Bosch, M. Lescure, R. Myllylä, and M. Rioux, "Laser ranging: A critical review of usual techniques for distance measurement," *Optical Engineering*, vol. 40, no. 1, pp. 10–19, 2001. DOI: 10.1117/1.1330700. [Online]. Available: <http://link.aip.org/link/?JOE/40/10/1>.
- [81] A. Dieckmann, "FMCW-LIDAR with tunable twin-guide laser diode," *Electronics Letters*, vol. 30, no. 4, pp. 308–309, Feb. 1994, ISSN: 0013-5194.
- [82] D. Huang, E. A. Swanson, C. P. Lin, J. S. Schuman, W. G. Stinson, W. Chang, M. R. Hee, T. Flotte, K. Gregory, C. A. Puliafito, and J. G. Fujimoto, "Optical coherence tomography," *Science*, vol. 254, no. 5035, pp. 1178–1181, Nov. 1991, 1957169[pmid], ISSN: 0036-8075. [Online]. Available: <http://www.ncbi.nlm.nih.gov/pmc/articles/PMC4638169/>.
- [83] R. H. Dicke, *Object detection system*, US Patent 2,624,876, Jun. 1953. [Online]. Available: <https://www.google.com/patents/US2624876>.
- [84] J. A. Scheer, J. A. Scheer, and J. L. Kurtz, *Coherent Radar Performance Estimation.*, 1993.
- [85] M. A. Choma, K. Hsu, and J. A. Izatt, "Swept source optical coherence tomography using an all-fiber 1300-nm ring laser source," *Journal of Biomedical Optics*, vol. 10, no. 4, pp. 044 009–044009-6, 2005. DOI: 10.1117/1.1961474. [Online]. Available: <http://dx.doi.org/10.1117/1.1961474>.

- [86] N. Satyan, A. Vasilyev, G. Rakuljic, V. Leyva, and A. Yariv, "Precise control of broadband frequency chirps using optoelectronic feedback," *Opt. Express*, vol. 17, no. 18, pp. 15 991–15 999, Aug. 2009. doi: 10.1364/OE.17.015991. [Online]. Available: <http://www.opticsexpress.org/abstract.cfm?URI=oe-17-18-15991>.
- [87] ANSI, "American national standard for the safe use of lasers," *ANSI Z136.1 (Laser Institute of America, Orlando, FL, 2007)*,
- [88] G. K. Ackermann and J. Eichler, *Holography. A Practical Approach*. Wiley-VCH, 2007.
- [89] E. W. Max Born, *Principles of optics*, 7th. Cambridge University Press, 1999.
- [90] A. V. Oppenheim and R. W. Schaffer, *Discrete-Time Signal Processing*, 3rd. Upper Saddle River, NJ, USA: Prentice Hall Press, 2009.
- [91] B. J. Vakoc, D. Fukumura, R. K. Jain, and B. E. Bouma, "Cancer imaging by optical coherence tomography: Preclinical progress and clinical potential," *Nat Rev Cancer*, vol. 12, no. 5, pp. 363–368, May 2012, ISSN: 1474-175X. doi: 10.1038/nrc3235. [Online]. Available: <http://dx.doi.org/10.1038/nrc3235>.
- [92] B. Behroozpour, P. A. M. Sandborn, N. Quack, T. J. Seok, Y. Matsui, M. C. Wu, and B. E. Boser, "Electronic-photonic integrated circuit for 3d microimaging," *IEEE Journal of Solid-State Circuits*, vol. 52, no. 1, pp. 161–172, Jan. 2017, ISSN: 0018-9200. doi: 10.1109/JSSC.2016.2621755.
- [93] —, "Chip-scale electro-optical 3D FMCW lidar with 8 um ranging precision," in *2016 IEEE International Solid-State Circuits Conference (ISSCC)*, Jan. 2016, pp. 214–216. doi: 10.1109/ISSCC.2016.7417983.
- [94] F. G. D. Corte, G. Cocorullo, M. Iodice, and I. Rendina, "Temperature dependence of the thermo-optic coefficient of InP, GaAs, and SiC from room temperature to 600 K at the wavelength of 1.5 um," *Applied Physics Letters*, vol. 77, no. 11, pp. 1614–1616, 2000. doi: 10.1063/1.1308529. eprint: <http://dx.doi.org/10.1063/1.1308529>. [Online]. Available: <http://dx.doi.org/10.1063/1.1308529>.
- [95] V. Jayaraman, G. D. Cole, M. Robertson, C. Burgner, D. John, A. Uddin, and A. Cable, "Rapidly swept, ultra-widely-tunable 1060 nm MEMS-VCSELs," *Electronics Letters*, vol. 48, no. 21, pp. 1331–1333, Oct. 2012, ISSN: 0013-5194. doi: 10.1049/el.2012.3180.
- [96] V. Jayaraman, G. D. Cole, M. Robertson, A. Uddin, and A. Cable, "High-sweep-rate 1310 nm MEMS-VCSEL with 150 nm continuous tuning range," *Electronics Letters*, vol. 48, no. 14, pp. 867–869, Jul. 2012, ISSN: 0013-5194. doi: 10.1049/el.2012.1552.

- [97] I. Grulkowski, J. J. Liu, B. Potsaid, V. Jayaraman, C. D. Lu, J. Jiang, A. E. Cable, J. S. Duker, and J. G. Fujimoto, "Retinal, anterior segment and full eye imaging using ultrahigh speed swept source OCT with vertical-cavity surface emitting lasers," *Biomed. Opt. Express*, vol. 3, no. 11, pp. 2733–2751, Nov. 2012. DOI: 10.1364/BOE.3.002733. [Online]. Available: <http://www.osapublishing.org/boe/abstract.cfm?URI=boe-3-11-2733>.
- [98] Y. Watanabe, K. Yamada, and M. Sato, "Three-dimensional imaging by ultrahigh-speed axial-lateral parallel time domain optical coherence tomography," *Opt. Express*, vol. 14, no. 12, pp. 5201–5209, Jun. 2006. DOI: 10.1364/OE.14.005201. [Online]. Available: <http://www.opticsexpress.org/abstract.cfm?URI=oe-14-12-5201>.
- [99] E. Beaurepaire, A. C. Boccara, M. Lebec, L. Blanchot, and H. Saint-Jalmes, "Full-field optical coherence microscopy," *Opt. Lett.*, vol. 23, no. 4, pp. 244–246, Feb. 1998. DOI: 10.1364/OL.23.000244. [Online]. Available: <http://ol.osa.org/abstract.cfm?URI=ol-23-4-244>.
- [100] L. Vabre, A. Dubois, and A. C. Boccara, "Thermal-light full-field optical coherence tomography," *Opt. Lett.*, vol. 27, no. 7, pp. 530–532, Apr. 2002. DOI: 10.1364/OL.27.000530. [Online]. Available: <http://ol.osa.org/abstract.cfm?URI=ol-27-7-530>.
- [101] A. Dubois, L. Vabre, A.-C. Boccara, and E. Beaurepaire, "High-resolution full-field optical coherence tomography with a linnik microscope," *Appl. Opt.*, vol. 41, no. 4, pp. 805–812, Feb. 2002. DOI: 10.1364/AO.41.000805. [Online]. Available: <http://ao.osa.org/abstract.cfm?URI=ao-41-4-805>.
- [102] A. Dubois, G. Moneron, K. Grieve, and A. C. Boccara, "Three-dimensional cellular-level imaging using full-field optical coherence tomography," *Physics in Medicine & Biology*, vol. 49, no. 7, p. 1227, 2004. [Online]. Available: <http://stacks.iop.org/0031-9155/49/i=7/a=010>.
- [103] T.-W. Hui and G. K.-H. Pang, "Solder paste inspection using region-based defect detection," *The International Journal of Advanced Manufacturing Technology*, vol. 42, no. 7, p. 725, Aug. 2008, ISSN: 1433-3015. DOI: 10.1007/s00170-008-1639-6. [Online]. Available: <https://doi.org/10.1007/s00170-008-1639-6>.
- [104] B. W. Graf and S. A. Boppart, "Imaging and analysis of three-dimensional cell culture models," in *Live Cell Imaging: Methods and Protocols*, D. B. Papkovsky, Ed. Totowa, NJ: Humana Press, 2010, pp. 211–227, ISBN: 978-1-60761-404-3. DOI: 10.1007/978-1-60761-404-3_13. [Online]. Available: https://doi.org/10.1007/978-1-60761-404-3_13.

- [105] Y. Yasuno, S. Makita, T. Endo, G. Aoki, H. Sumimura, M. Itoh, and T. Yatagai, "One-shot-phase-shifting fourier domain optical coherence tomography by reference wavefront tilting," *Opt. Express*, vol. 12, no. 25, pp. 6184–6191, Dec. 2004. doi: 10.1364/OPEX.12.006184. [Online]. Available: <http://www.opticsexpress.org/abstract.cfm?URI=oe-12-25-6184>.
- [106] S. Bourquin, P. Seitz, and R. P. Salathé, "Optical coherence topography based on a two-dimensional smart detector array," *Opt. Lett.*, vol. 26, no. 8, pp. 512–514, Apr. 2001. doi: 10.1364/OL.26.000512. [Online]. Available: <http://ol.osa.org/abstract.cfm?URI=ol-26-8-512>.
- [107] J. F. de Boer, R. Leitgeb, and M. Wojtkowski, "Twenty-five years of optical coherence tomography: the paradigm shift in sensitivity and speed provided by Fourier domain OCT (Invited)," *Biomed. Opt. Express*, vol. 8, no. 7, pp. 3248–3280, Jul. 2017. doi: 10.1364/BOE.8.003248. [Online]. Available: <http://www.osapublishing.org/boe/abstract.cfm?URI=boe-8-7-3248>.
- [108] M. Wojtkowski, V. J. Srinivasan, T. H. Ko, J. G. Fujimoto, A. Kowalczyk, and J. S. Duker, "Ultrahigh-resolution, high-speed, Fourier domain optical coherence tomography and methods for dispersion compensation," *Opt. Express*, vol. 12, no. 11, pp. 2404–2422, May 2004. doi: 10.1364/OPEX.12.002404. [Online]. Available: <http://www.opticsexpress.org/abstract.cfm?URI=oe-12-11-2404>.
- [109] Cospheric, *Retroreflective aluminum coated solid glass microspheres 4.2g/cc 30-100um - bulk with optional coatings*. [Online]. Available: http://www.cospheric.com/high_index_of_refraction_barium_titante_glass_spheres_bulk.html.
- [110] J. A. Izatt and M. A. Choma, "Theory of optical coherence tomography," in *Optical Coherence Tomography: Technology and Applications*, W. Drexler and J. G. Fujimoto, Eds. Berlin, Heidelberg: Springer Berlin Heidelberg, 2008, pp. 47–72. doi: 10.1007/978-3-540-77550-8_2. [Online]. Available: http://dx.doi.org/10.1007/978-3-540-77550-8_2.
- [111] R. Horstmeyer, R. Heintzmann, G. Popescu, L. Waller, and C. Yang, "Standardizing the resolution claims for coherent microscopy," *Nat Photon*, vol. 10, no. 2, pp. 68–71, Feb. 2016, Commentary, ISSN: 1749-4885. [Online]. Available: <http://dx.doi.org/10.1038/nphoton.2015.279>.
- [112] E. R. Dowski and W. T. Cathey, "Extended depth of field through wavefront coding," *Appl. Opt.*, vol. 34, no. 11, pp. 1859–1866, Apr. 1995. doi: 10.1364/AO.34.001859. [Online]. Available: <http://ao.osa.org/abstract.cfm?URI=ao-34-11-1859>.
- [113] P. Ferraro, S. Grilli, D. Alfieri, S. D. Nicola, A. Finizio, G. Pierattini, B. Javidi, G. Coppola, and V. Striano, "Extended focused image in microscopy by digital holography," *Opt. Express*, vol. 13, no. 18, pp. 6738–6749, Sep.

2005. doi: 10.1364/OPEX.13.006738. [Online]. Available: <http://www.opticsexpress.org/abstract.cfm?URI=oe-13-18-6738>.
- [114] D. Hillmann, C. Lührs, T. Bonin, P. Koch, and G. Hüttmann, "Holoscopy & holographic optical coherence tomography," *Opt. Lett.*, vol. 36, no. 13, pp. 2390–2392, Jul. 2011. doi: 10.1364/OL.36.002390. [Online]. Available: <http://ol.osa.org/abstract.cfm?URI=ol-36-13-2390>.
- [115] J. Goodman, *Introduction to Fourier Optics*, ser. McGraw-Hill physical and quantum electronics series. W. H. Freeman, 2005. [Online]. Available: https://books.google.com/books?id=ow5xs%5C_Rtt9AC.
- [116] V. J. Srinivasan, D. C. Adler, Y. Chen, I. Gorczynska, R. Huber, J. S. Duker, J. S. Schuman, and J. G. Fujimoto, "Ultrahigh-speed optical coherence tomography for three-dimensional and en face imaging of the retina and optic nerve head," *Investigative Ophthalmology & Visual Science*, vol. 49, no. 11, p. 5103, 2008. doi: 10.1167/iovs.08-2127. eprint: /data/journals/iovs/932946/z7g01108005103.pdf. [Online]. Available: <http://dx.doi.org/10.1167/iovs.08-2127>.

Appendix A

SILICON AND III-V WAFERS

Table A.1 summarizes the silicon and InGaAsP wafers used for the fabrication of the quantum noise controlled lasers described in this thesis. The silicon wafer was obtained from Prof. John Bowers at University of California Santa Barbara with a thermal oxide thickness 400 nm. The oxide layer is thinned to the desired thickness for the quantum noise control layer using HF. InGaAsP wafers were sourced from LandMark Optoelectronics Corp. The thickness of the silicon handle is thinned to 150 μm using mechanical lapping.

Name	Material	Height (nm)	Doping (cm^3)	Refractive index
p-contact layer	$\text{In}_{.53}\text{Ga}_{.47}\text{As}$	200	$p > 1 \times 10^{19}$	3.34
p-cladding	InP	1500	$p = 1 \times 10^{18} \rightarrow 1 \times 10^{17}$	3.1
Separate confinement layer	1.15Q InGaAsP	40	none	3.33
Separate confinement layer	1.25Q InGaAsP	40	none	3.3755
Quantum wells $\times 5$	InGaAsP (1550 nm)	7 (per well)	none	3.53
Quantum well barriers $\times 4$	InGaAsP	10 (per barrier)	none	3.3755
Separate confinement layer	1.25Q InGaAsP	40	none	3.3755
Separate confinement layer	1.15Q InGaAsP	40	none	3.33
n-contact	InP	110	$n = 1 \times 10^{18}$	3.1
Super lattice (layer 1)	$\text{In}_{.85}\text{Ga}_{.15}\text{As}_{.327}\text{P}_{.673}$	7.5	$n = 1 \times 10^{18}$	3.25
Super lattice (layer 2)	InP	7.5	$n = 1 \times 10^{18}$	3.21
Super lattice (layer 3)	$\text{In}_{.85}\text{Ga}_{.15}\text{As}_{.327}\text{P}_{.673}$	7.5	$n = 1 \times 10^{18}$	3.25
Super lattice (layer 4)	InP	7.5	$n = 1 \times 10^{18}$	3.21
Bonding layer	InP	10	$n = 1 \times 10^{18}$	3.21
Quantum noise control layer	SiO_2	30 \rightarrow 150	none	1.5
Silicon device layer	Si	500	light p	3.46
Buried oxide layer	SiO_2	1000	none	1.5
Silicon handle	Si	150 μm	none	3.46

Table A.1: Summary of the wafers used to fabricate the high-coherence lasers.